UNIVERSITY OF CALIFORNIA, SAN DIEGO

Detection Technique and Front-end RF Tunable Filter for Cognitive Radio Systems

A dissertation submitted in partial satisfaction of the
requirements for the degree
Doctor of Philosophy

in

Electrical Engineering (Electronic Circuits and Systems)

by

Sanghoon Park

Committee in charge:

Lawrence E. Larson, Chair
Laurence B. Milstein, Co-Chair
James F. Buckwalter
William S. Hodgkiss
William C. Trogler

2010

The dissertation of Sanghoon Park is approved, and it is acceptable in quality and form for publication on microfilm and electronically:

_____

_____

_____

_____
Co-Chair

_____
Chair

University of California, San Diego

2010

DEDICATION

To my parents and sister

For their love and support.

EPIGRAPH

If we knew what it was we were doing, it would not be called research, would it?

Albert Einstein

TABLE OF CONTENTS

LIST OF FIGURES

LIST OF TABLES

ACKNOWLEDGEMENTS

First and foremost, I am most thankful to my research advisers, Professors Lawrence E. Larson and Laurence B. Milstein. They are always kind and considerate. It is great fortune for me to share and discuss lots of things with them. Without their invaluable advice and support they provided me throughout my graduate studies at UCSD, I could not have finished this dissertation. I would like to acknowledge Dr. Vincent W. Leung (Qualcomm). His great knowledge and experience about the RFIC designs was very helpful. I could not have finished our ISCAS paper without his encouragement. I would also like to thank the members of my doctoral committee, Professors William S. Hodgkiss, William C. Trogler, and James F. Buckwalter for their invaluable suggestions and recommendations to this dissertation. I am deeply indebted for their help and support.

I am grateful to all my colleagues in our RFIC group for their beneficial suggestions and discussions: Mr. Namsoo Kim (Qualcomm), Mr. Myoungbo Kwak (Samsung), Dr. Himanshu Khatri (Qualcomm), Dr. Rahul Kodkani (NXP), Dr. Mohammad Farazian (Qualcomm), Dr. Joe Jamp (Atheros), Mr. Yiping Han (Qualcomm), Mr. Marcus Pan, Mr. Sean Kim, Mr. Pavel Kolinko, Mrs. Arpita Moghe, and Mr. Tyson Wooten. I also sincerely thank Dr. Donald Kimball, Dr. Doug Palmer, and Dr. Anders Plymoth for their help and discussions in the lab. Also, I would like to express my sincere thankfulness to all my lovely friends in U.S. and Korea. You guys always make me happy.

I would like to take this opportunity to express my gratitude to my family, my parents Mr. Jungwoo Park and Mrs. Junsook Kim and my younger sister Chunyoung Park. Their infinite love and care during my entire life have been encouraged me to overcome the hardship I experienced.

Finally, I would like to acknowledge the support of the UCSD Center for Wireless Communications, as well as the UC Discovery Grant Program, for my research works at UCSD.

The text of Chapter Two, Three, and Four in this dissertation, in part or in full, is a reprint of the material as it appears in our published papers or as it has been submitted for the following publications:

1. Sanghoon Park, Lawrence E. Larson, and Laurence B. Milstein, “Spectrum broad-

ening of phase noise interaction with applications to cognitive radio coexistence," submitted to *IEEE Communications Letters*, 2009.

2. Sanghoon Park, Lawrence E. Larson, and Laurence B. Milstein, "An RF receiver detection technique for UWB/WiMAX coexistence with applications to cognitive radio," submitted to *IEEE Transactions on Circuits and Systems*, 2009.

3. Sanghoon Park, Wingching V. Leung, and Lawrence E. Larson, "An improved wide-dynamic range tunable RF interference suppression notch filter," to appear in *Proc. IEEE International Symposium on Circuits and Systems*, May 2010.

4. Sanghoon Park, Lawrence E. Larson, and Laurence B. Milstein, "Phase noise effects on signal detection for UWB/WiMAX coexistence," in *Proc. International Conference on Military Communication*, 2008, pp. 1-7.

5. Sanghoon Park, Lawrence E. Larson, and Laurence B. Milstein, "Hidden mobile terminal device discovery in a UWB environment," in *Proc. IEEE International Conference on Ultra-Wideband*, 2006, pp. 417-421.

The dissertation author was the primary author listed in these publications directed and supervised the research which forms the basis for these chapters.

VITA

2001	Bachelor of Engineering in Electrical Engineering, Korea University, Seoul, Republic of Korea
2002-2003	Graduate Student Researcher in Electrical and Computer Engineering, Texas A&M University, College Station, TX
2004	Master of Science in Electrical and Computer Engineering, Texas A&M University, College Station, TX
2005-2009	Graduate Student Researcher in Electrical and Computer Engineering, University of California - San Diego, La Jolla, CA
2010	Doctor of Philosophy in Electrical and Computer Engineering, University of California - San Diego, La Jolla, CA

PUBLICATIONS

Sanghoon Park, Lawrence E. Larson, and Laurence B. Milstein, "Spectrum broadening of phase noise interaction with applications to cognitive radio coexistence," submitted to *IEEE Communications Letters*, 2009.

Sanghoon Park, Lawrence E. Larson, and Laurence B. Milstein, "An RF receiver detection technique for UWB/WiMAX coexistence with applications to cognitive radio," submitted to *IEEE Transactions on Circuits and Systems*, 2009.

Sanghoon Park, Wingching V. Leung, and Lawrence E. Larson, "An improved wide-dynamic range tunable RF interference suppression notch filter," to appear in *Proc. IEEE International Symposium on Circuits and Systems*, May 2010.

Sanghoon Park, Lawrence E. Larson, and Laurence B. Milstein, "Phase noise effects on signal detection for UWB/WiMAX coexistence," in *Proc. International Conference on Military Communication*, 2008, pp. 1-7.

Sanghoon Park, Lawrence E. Larson, and Laurence B. Milstein, "Hidden mobile terminal device discovery in a UWB environment," in *Proc. IEEE International Conference on Ultra-Wideband*, 2006, pp. 417-421.

ABSTRACT OF THE DISSERTATION

Detection Technique and Front-end RF Tunable Filter for Cognitive Radio Systems

by

Sanghoon Park

Doctor of Philosophy in Electrical Engineering (Electronic Circuits and Systems)

University of California San Diego, 2010

Lawrence E. Larson, Chair

Laurence B. Milstein, Co-Chair

Cognitive radio (CR) can effectively increase the spectral efficiency. However, there is an inevitable interference problem between the primary licensed users and the unlicensed CR devices. A detection technique utilizing the local oscillator (LO) leakage signal coming from a nearby mobile terminal is proposed and evaluated for short-range wireless communication systems, such as an ultra-wide band (UWB) system. Due to the low-level LO leakage, the detection sensitivity is a great concern. Local oscillator phase noise of the detector can degrade the detection sensitivity. Spectrum broadening of the LO phase noise interaction with an adjacent channel signal through a multiplier is analyzed and the degradation in detection performance is evaluated.

Spectrum broadening is applied to the cognitive radio (CR) device operation in UHF bands. A strong TV signal transmitted by a nearby TV station can interact with LO phase noise of a CR receiver, and induce serious in-band interference which possible degrades the receiver performance. In order to suppress strong TV signals, a wide dynamic range low-power CMOS-based RF tunable filter with image cancellation is presented using a balanced passive complex mixer and frequency dependent loads. The tunable RF notch filter with 17 dB attenuation and 1.6 dB insertion loss is achieved using parallel LC tank loads. A tunable RF bandpass filter is implemented with capacitive termination, and achieves 18 dB maximum attenuation and 1.8 dB insertion loss.

Chapter 1

Introduction

1.1 Cognitive Radio System

In modern wireless communication, most of the practical frequency bands are already occupied [10]. Table 1.1 contains a brief list of popular wireless systems in the North America. More frequency bands, nevertheless, are required to handle more users simultaneously as well as provide faster data service. In addition, since the propagation properties are getting worse as the operating frequency increases [11–13], the favorable spectral bands for commercial wireless services are currently limited to 6 GHz, as shown in Table 1.1, and may be extended to roughly 10 GHz in the near future. Therefore, the limited spectrum resource should be carefully managed.

In order to increase the spectrum efficiency, spectrum sharing is an attractive approach. As a result, interference problems between wireless systems occupying the same frequency band is of great concern, and so an efficient method to minimize this problem is required. Cognitive radio (CR) was proposed to manage the frequency allocation problems due to spectrum crowding by multiple wireless devices [14, 15]. As an extended concept of the software-defined radio (SDR) [16–18], a CR device can adaptively change its receiving and transmitting parameters to communicate using unoccupied frequency bands on a non-interfering basis with the primary users [14, 15, 19]. A CR device should support stand-alone as well as collaborative operations. Eventually, a group of CR devices constitutes a large-scale CR network [15, 20–22].

Table 1.1: Frequency band allocations for popular wireless systems in North American standard

Wireless System	**Frequency Bands**
AM Radio	0.5 $\sim$ 1.6 MHz
Walkie–Talkie	49 MHz, 450 $\sim$ 470 MHz
FM Radio	88 $\sim$ 108 MHz
Cordless Home Phone	43 $\sim$ 50 MHz, 902 $\sim$ 928 MHz 1.92 $\sim$ 1.93 GHz, 5.725 $\sim$ 5.825 GHz
Digital TV	54 $\sim$ 698 MHz
Wireless Microphone	174 $\sim$ 216 MHz, 470 $\sim$ 698 MHz
GPS[1]	1.217 $\sim$ 1.237 GHz, 1.565 $\sim$ 1.585 GHz
GSM[2]	824 $\sim$ 849 MHz, 1.85 $\sim$ 1.91 GHz
AMPS[3]	824 $\sim$ 849 MHz, 869 $\sim$ 894 MHz
ZigBee	902 $\sim$ 928 MHz, 2.4 $\sim$ 2.484 GHz
Pager	929 $\sim$ 932 GHz
PCS[4]	1.85 $\sim$ 1.99 GHz
Satellite Radio	2.31 $\sim$ 2.36 GHz
Wi-Fi	2.4 $\sim$ 2.484 GHz, 5.15 $\sim$ 5.35 GHz 5.725 $\sim$ 5.825 GHz
Bluetooth Headset	2.4 $\sim$ 2.484 GHz
WiMAX[5]	2.3 $\sim$ 2.4 GHz, 2.496 $\sim$ 2.69 GHz 3.3 $\sim$ 3.8 GHz
UWB[6]	3.1 $\sim$ 10.6 GHz
Ground to Satellite	3.7 $\sim$ 4.2 GHz, 5.925 $\sim$ 6.425 GHz
Satellite TV	12.2 $\sim$ 12.7 GHz

[1]Global positioning system. [2]Global system for mobile communications. [3]Advanced mobile phone service. [4]Personal communications system. [5]Worldwide interoperability for microwave access. [6]Ultra-wide band.

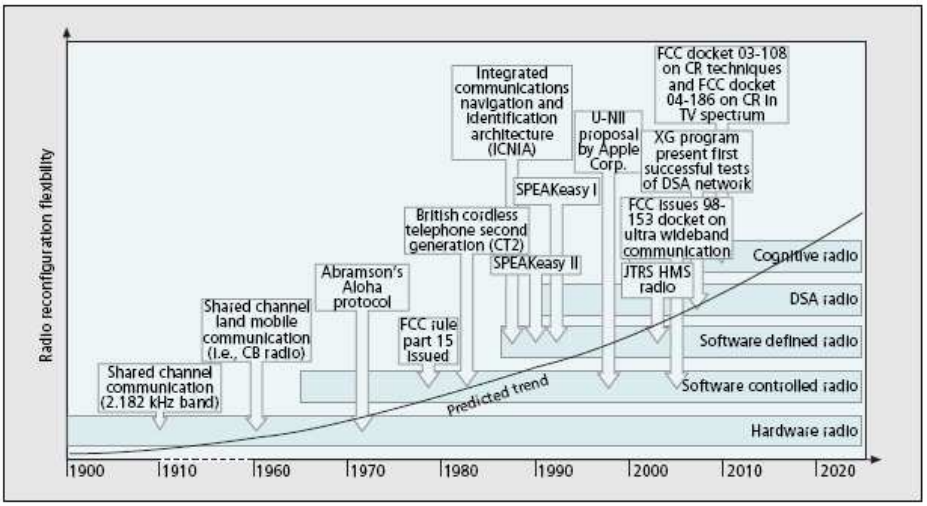

Figure 1.1: History of cognitive radio related systems [1].

The term, *Cognitive Radio*, was first mentioned by Mitola in 1999 [14]. However, the concept of sharing frequency spectrum dates back to maritime communication in early 20th century [1]. Through the Aloha protocol in 1970 that enabled radio channel sharing [1, 23], the unlicensed frequency spectrum in 0.9, 2.4, 5.7 GHz bands became first available by the Federal Communications Commission (FCC) in 1985 [24]. Based on the huge success of Wi-Fi products in the 2.4 GHz industrial, scientific, and medical (ISM) band, the FCC in 2002 allowed an unlicensed device operation, known as an ultra-wide band (UWB) system, in the licensed bands [2]. Even though CR-based operation is not mandatory for a UWB device, research has been actively ongoing about the interference problem due to a UWB device and CR-based UWB operation [25–30]. Recently, the FCC introduced the CR-based device operation as a secondary user in the TV bands in 2008 [31]. The development of CR-related systems are consolidated in Fig. 1.1.

Cognitive radios should be built with end-to-end operations from spectrum sensing to real-time communication by dynamically organizing RF spectrum detection and estimation processes, channel-state identification and prediction processes, power control technique, dynamic channel allocation, adaptive modulation, and cognitive management [15, 19, 32, 33]. As an initial phase of standardizing CR system, most current

research work is focusing on adaptive spectrum access, which includes spectrum sensing, avoidance, and allocation techniques. In particular, a robust detection technique for sensing unoccupied frequency spectrum is an important prerequisite for all other processes. There are three popular detection techniques, based on knowledge of the signal that a CR wants to detect.

1. Correlation detection [34–38]: Correlation detection, also known as matched filtering detection, is the optimal detection technique when a deterministic signal is buried in an additive Gaussian white noise (AWGN) environment. In order to maximize the signal-to-noise ratio (SNR), the correlation detection adaptively controls its multiplication weight, so that greater weight is applied when the input SNR is higher. Correlation detection is widely used in most of the modern modulation techniques. In order to detect a signal in a colored noise background, a pre-whitening filter is desirable before the correlation detection. If the signal is not known, correlation detection becomes seriously degraded .

2. Energy detection [38–42]: The energy detector, also known as a radiometer, is one of the most popular detectors due to its simplicity. It typically consists of a front-end bandpass filter, square-law device, and finite time integrator. Therefore, the energy of all the received signals is accumulated for a given observation time. When an unknown signal is buried in noise environment, the energy detector can effectively differentiate the signal-plus-noise input from the noise only input. However, the signal resolution of the energy detector is very limited, and so it is only useful to determine the presence of the signal. The energy detector has a critical detection problem when the estimate of the ambient noise is not accurate. Then, the signal below a reference point cannot be detected by the energy detector, even with infinite observation time. This reference point is called the minimum required SNR, or SNR wall.

3. Feature detection [26, 43–46]: Two types of the feature detection are common. One exploits a known feature of a signal. One example is pilot signal detection. If the primary system employs the pilot signals for synchronization, a CR device can also utilize the pilot signals to determine the presence of the primary user in a cer-

tain frequency band. Due to the use of coherent detection, pilot detection is beneficial for the lower SNR conditions, compared with energy detection. However, pilot detection requires some prerequisite signal information. The other technique is discriminating the features of a signal from the background noise. Since the modulated signals are cyclostationary rather than stationary, cyclostationary detection can determine the presence of a signal using the inherent cyclostationary properties for different types of modulations. The cyclosationarity of the received signals can be revealed by investigating correlation properties between the frequency components. Cyclostationary detection suffers from increased complexity, interference from multiple signals, cyclosationary noise generated by the system itself (such as a mixer), and analysis difficulty for its detection performance.

This dissertation can be divided into two broad topics. The first part of this dissertation describes the detection problems for the cognitive radio operation of a UWB device, in order to protect the primary worldwide interoperability for microwave access (WiMAX) users. The salient features of the UWB and WiMAX systems are described in Sections 1.2 and Section 1.3, respectively. The second part of this dissertation describes an interference suppression tunable RF filter to support for the IEEE 802.22 cognitive radio system in the TV bands. The general description for the IEEE 802.22 cognitive radio system is given in Section 1.4. Section 1.5 presents an overview of this dissertation.

1.2 Ultra-wide Band System

In 2002, the FCC authorized the unlicensed use of the frequency band from 3.1 to 10.6 GHz for UWB systems [2]. The UWB signal can be defined as follows [2]:

1. Fractional bandwidth, defined by $\frac{f_U - f_L}{(f_U + f_L)/2}$, where f_U and f_L denote the upper and lower frequencies of the 10 dB emission point, respectively, is equal or greater than 0.2.

2. Regardless of its fractional bandwidth, its absolute bandwidth, $f_U - f_L$, is greater than 500 MHz.

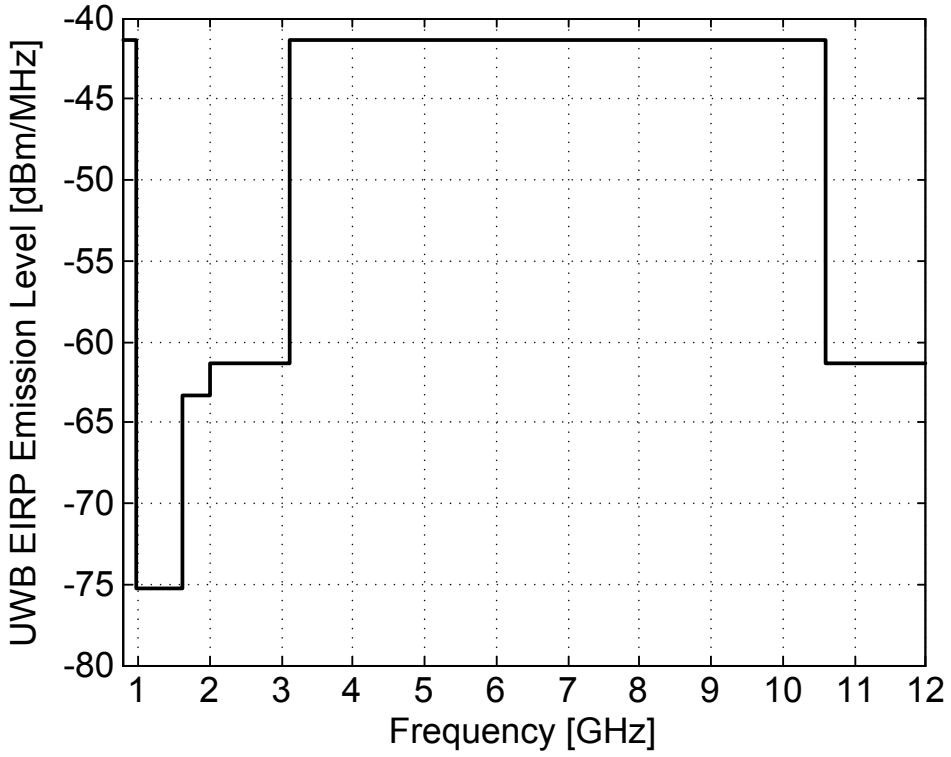

Figure 1.2: Spectral mask for hand-held UWB Systems [2, 3]. Emission level is measured in 1 MHz bandwidth.

This large signal bandwidth among currently existing wireless systems is the unique characteristic of the UWB systems.

Since a UWB signal occupies such a large spectral band, it is inevitable that it will overlap other wireless system bands. In order to protect the primary users from harmful interference problems due to the unlicensed operation of UWB devices, the emission power of the UWB signal is stringently restricted by the FCC [2], and the effective isotropic radiation power (EIRP) of a UWB signal should be less than -41.25 dBm/MHz between 3.1 and 10.6 GHz. The FCC-allowed spectral mask for hand-held UWB Systems is shown in Fig. 1.2. Due to its low power and fast data rate capabilities, the most suitable applications are found in the high speed wireless personal area networks (WPANs), such as remote controllers, radio-frequency identifications (RFIDs), sensor networks, wireless home/office networking, etc.

Two different standards for the UWB systems have been simultaneously developed by IEEE 802.15 working group [47]: single-band impulse radio system and multi-band orthogonal frequency division multiplexing (OFDM) system.

1.2.1 Single Band Impulse Radio System

Single band impulse radio systems exploit a signal whose spectral band is equal to the entire UWB spectral width of 7.5 GHz when transmitting or receiving the data. Using short-time impulse signal, the single band impulse radio can accommodate multiple users in separate time frames. The major properties of the single-band impulse radio system can be summarized as follows:

- Simplified receiver and transmitter architecture due to the absence of the mixing stage
- Low power and low cost implementation
- Controllable signal-to-noise ratio at the receiver side by transmitting and receiving multiple impulses to represent single data bit
- High accuracy in ranging and position location due to its narrow pulse width of a few nanoseconds
- Robust to the narrow band jammers due to its wide signal bandwidth
- Highly required timing precision and signal synchronization

1.2.2 Multi-band OFDM System

The multi-band OFDM system was proposed to enhance its flexibility to support worldwide operation with high frequency efficiency [3]. In the multi-band OFDM systems, the allocated UWB frequency band from 3.1 to 10.6 GHz is divided into five non-overlapped frequency bands called groups, as shown in Fig. 1.3. Each group has three non-overlapped channels, and a channel consists of 128 orthogonal subcarriers

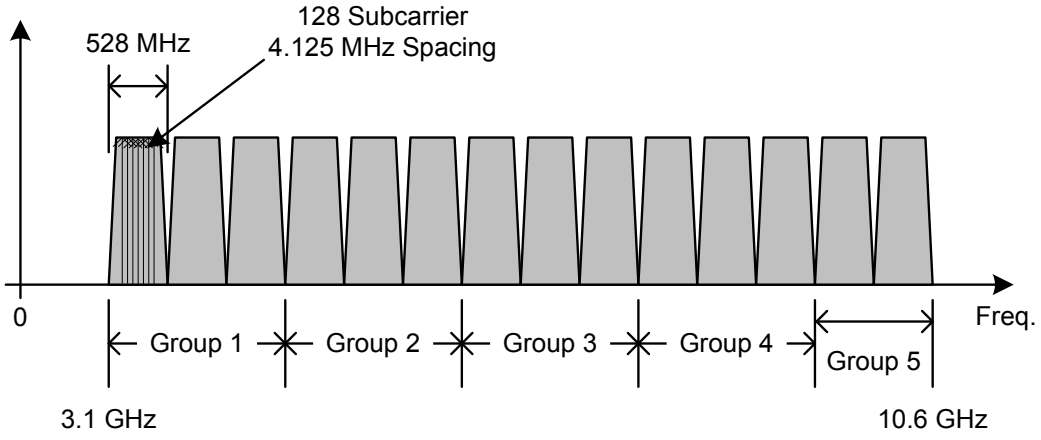

Figure 1.3: Frequency allocation for the Multi-band OFDM System.

with a subcarrier spacing of 4.125 MHz. The major properties of multi-band OFDM systems can be summarized as follows:

- Flexible frequency planning by selectively tuning on and off subcarriers
- Eased hardware implementation due to the relatively narrow channel bandwidth of 512 MHz
- Accommodating multiple multi-band OFDM UWB devices using frequency hopping
- High instantaneous SNR with low average power level using frequency hopping
- Fast settling time requirement to support frequency hopping
- Susceptible to the frequency variation of the subcarriers
- High peak to average power ratio of the OFDM signal

1.3 Worldwide Interoperability for Microwave Access System

Worldwide interoperability for microwave access (WiMAX), based on the IEEE 802.16 air interface standard [4, 5], is one of the wireless systems that are expected to

share the frequency spectrum with UWB devices. The IEEE 802.16 working group was formed to develop an air interface standard for broadband wireless metropolitan area networks (WMANs) [48]. The initial objective of the IEEE 802.16 working group was the development of a point-to-multi-point (PMP) wireless network access using a line-of-sight (LOS) channel between 10 and 66 GHz with an average bandwidth performance of 70 Mbps and a cell coverage of 50 km. Thus, it was basically developed to provide a wireless connection between buildings using exterior antennas and a baseband radio station by replacing a cable modem network and digital subscriber lines (DSL) in an urban area [4].

In December, 2005, the IEEE ratified the 802.16e amendment [5]. This amendment included new features and attributes such as scalable OFDM, multiple inputs and multiple outputs (MIMO), and power management scenarios using *idle* and *sleep* modes, in order to support seamless mobile connectivity of the WiMAX system, which is called mobile WiMAX [9]. Thus, the coverage of the WiMAX system was extended to personal hand-held mobile devices. For better propagation properties of the wireless channel, mobile WiMAX systems focus on several frequency bands, ranging from 2 to 11 GHz, and Table 1.2 shows the initial mobile WiMAX certification profiles in the 2.3, 2.5, 3.3, and 3.5 GHz bands [8, 9]. Some important features of the mobile WiMAX system are as follows [4, 5, 8, 9, 48]:

- Scalable OFDM: The mobile WiMAX system can easily scale its channel bandwidth by flexibly selecting available subcarriers.

- Subchannelization: The available subcarriers can be divided into several groups to enhance range performance and to increase the battery efficiency for the mobile WiMAX devices.

- Advanced antenna technique: The WiMAX system supports multiple-inputs and multiple-outputs, including space-time coding, spatial multiplexing, phased array beam-forming, etc.

- Power-saving management: In order to extend the battery life of the hand-held mobile WiMAX devices, the mobile WiMAX system has three different classes

Table 1.2: Mobile WiMAX initial certification profiles [8]

Frequency Band	Channel Bandwidth	Duplexing
2.3 $\sim$ 2.4 GHz	5 MHz	TDD[1]
	10 MHz	TDD
	8.75 MHz	TDD
2.305 $\sim$ 2.320 GHz	3.5 MHz	TDD
	5 MHz	TDD
2.345 $\sim$ 2.360 GHz	5 MHz	TDD
	10 MHz	TDD
2.496 $\sim$ 2.690 GHz	5 MHz	TDD
	10 MHz	TDD
3.3 $\sim$ 3.4 GHz	5 MHz	TDD
	7 MHz	TDD
	10 MHz	TDD
3.4 $\sim$ 3.8 GHz	5 MHz	TDD
3.4 $\sim$ 3.6 GHz	7 MHz	TDD
3.6 $\sim$ 3.8 GHz	10 MHz	TDD

[1]Time-division duplexing.

of power-saving schemes.

- Various duplexing types: All the initial certification profiles in Table 1.2 support time-division duplexing (TDD) only, but frequency-division duplexing (FDD) as well as half-duplex FDD is also supported for the fixed WiMAX applications.

- Advanced security: The WiMAX system uses the advanced encryption standard (AES) and the extensible authentication protocol (EAP) to support secured private data services.

- Quality-of-service (QoS): Based on the connection-oriented protocol, the WiMAX system supports constant/variable bit rates, and real/non-real time traffic for various data types.

Among lots of salient features of the WiMAX system, the most important ones are scalable OFDM and subchannelization techniques. We will discuss the details of scalable OFDM and subchannelization now.

1.3.1 Scalable Orthogonal Frequency Division Multiplexing Signal with Subchannelization

An OFDM symbol consists of modulated subcarriers, which are mutually orthogonal within one symbol period. The complex baseband OFDM symbol, denoted by $\tilde{s}(t)$, can be represented by

$$\tilde{s}(t) = \frac{1}{\sqrt{N}} \sum_{k=0}^{N-1} A_k \text{exp}\left(j2\pi \left[\frac{k-(N-1)/2}{T_S} \right] t \right) \tag{1.1}$$

where A_k is the complex data of the *k*th subcarrier and N and T_S denote the total number of subcarriers and the OFDM symbol period [49, 50]. With the help of a long symbol duration of the subcarrier, the OFDM signal becomes less susceptible to the inter-symbol interference (ISI) problem in a multi-path fading channel. Thus, the OFDM technique helps the WiMAX system to robustly operate in the non-line-of-sight (NLOS) wireless conditions of an urban area.

An OFDM symbol is made up of a bunch of subcarriers. There are three different types of subcarriers [4, 5, 8, 9]:

1. Data subcarriers: For data transmission
2. Pilot subcarriers: For various estimation purposes
3. Null subcarriers: No signal transmission for guard bands and DC subcarrier

Figure 1.4 (a) shows an OFDM symbol with three different types of subcarriers. Moreover, the available subcarriers can be divided into several groups, called subchannelization, as shown in Fig. 1.4 (b).

The mobile WiMAX system is based on scalable OFDM, which supports variable bandwidth by adjusting the fast Fourier transform (FFT) size. Note that the subcarrier frequency spacing is fixed at 10.94 kHz in mobile WiMAX scalable OFDM. The scalable OFDM parameters are listed in Table 1.3.

Since the OFDM signal is based on the orthogonality of the subcarriers, any frequency instability due to the phase noise and Doppler shift can possibly degrade receiver

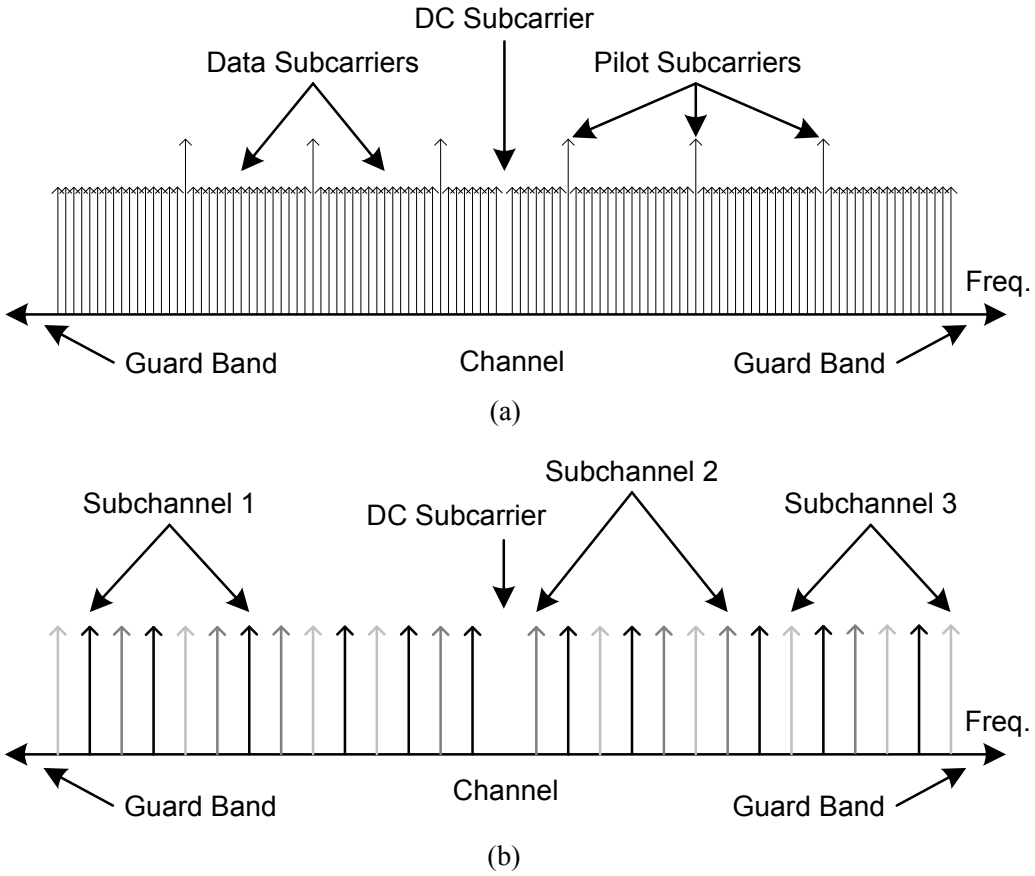

Figure 1.4: (a) OFDM symbol subcarrier description [4, 5], (b) OFDM symbol subchannelization (three subchannelizations example) [4, 5].

Table 1.3: Parameters used in mobile WiMAX scalable OFDM [8, 9]

Parameters	**Channel Bandwidth**			
Channel bandwidth (MHz)	1.25	5	10	20
FFT size	128	512	1024	2048
Number of data subcarriers[1]	72	360	720	1440
Number of pilot subcarriers[1]	12	60	120	240
Number of guardband subcarriers[1]	44	92	184	368
Sample rate (MHz)	1.4	5.6	11.2	22.4
Subcarrier frequency spacing (kHz)	10.94			
Useful symbol time (μs)	91.4			
Guard time (μs)	11.4			
OFDM symbol duration (μs)	102.9			
Number of OFDM symbol in 5 ms frame	48			

[1]The mobile WiMAX subcarrier distribution for downlink partial usage of subcarriers.

performance. Another drawback of the OFDM signal is its high peak-to-average power ratio (PAPR), causing power management problems [51–55].

1.4 IEEE 802.22 System

In May 2004, a notice of proposed rulemaking (NPRM) was issued by the FCC [56]. It proposed to utilize unoccupied TV bands by license-exempt wireless devices to increase spectral efficiency as well as to promote broadband wireless service. Many portions of the frequency bands primarily assigned to the TV broadcasting services were underutilized [57, 58]. Also, explosive growth of Wi-Fi market using unlicensed ISM band at 2 GHz and national information infrastructure (UNII) bands at 5 GHz motivated the FCC to consider more frequency bands for unlicensed usage [13,59]. However, there was serious debate on the potential interference problems caused by unlicensed devices. Incumbent TV broadcasters generally opposed the FCC notice allowing interfering mobile devices to operate in the same frequency bands.

The FCC released its order allowing unlicensed wireless devices to operate in unoccupied TV channels between 2 and 51 except channels 3, 4, and 37 in Nov. 2008 [31]. In particular, approximately 200 MHz of bandwidth from 500 to 700 MHz, spanning

the TV channels between 21 and 51 (except channel 37), is now available for personal portable devices [31]. The available frequency bands may be extended to $41 \sim 910$ MHz, and cover variable channel bandwidths from 6 to 8 MHz, in order to meet international regulations [13]. However, the very strict sense of non-interfering operation for unlicensed devices has been adopted to protect the primary users such as TV broadcasting services and wireless microphones [31].

The IEEE 802.22 working group was formed in October 2004, and has been developing a world-wide CR-based air interface standard for wireless regional area networks (WRANs) using the TV bands [13, 60]. Using longer propagation and better penetration wave properties in the very high frequency (VHF) and ultra high frequency (UHF) bands, the IEEE 802.22 working group is pursuing wide wireless coverage range of up to 100 km, so that the most suitable application of the IEEE 802.22 system is broadband wireless service in less-populated or less-developed areas, with comparable performance to the existing cabled network services [11, 13, 58, 61–63].

The ongoing standard in the IEEE 802.22 working group has lots of similar aspects and techniques with the WiMAX system in Section 1.3. The major difference of the IEEE 802.22 system from the WiMAX system is the stringent interference control protocols represented by the incorporated CR techniques such as dynamic spectrum sensing, detection and avoidance (DAA), dynamic frequency selection (DFS), spectrum management schemes, etc [13, 64]. A CR device operating in the TV bands should not interfere with the primary signals such as digital/analog TV and wireless microphone signals. Table 1.4 lists the key detection parameters accepted in the IEEE 802.22 standard, which are based on the DFS model for 5 GHz bands by the FCC [13, 63, 65].

An IEEE 802.22 CR device must coexist with commercial TV systems. The presence of a strong adjacent TV signal is one of the challenging characteristics of the IEEE 802.22 system. A signal transmitted by a nearby TV station can be so strong that a level of -8 dBm is suggested in terms of the receiver blocking level [66]. However, the minimum detectable CR signal level can be as weak as -102 dBm [66]. Thus, the required dynamic range, more than 90 dB, of the receiver puts a heavy burden on the receiver design to process a weak desired signal simultaneously with a strong TV signal. Therefore, an interference suppression filtering technique is highly desired to suppress

Table 1.4: Detection parameters for the IEEE 802.22 system

Parameters	**Value for Wireless Microphones**	**Value for TV Broadcasting**
Channel detection time	≤ 2 second	≤ 2 second
Detection Threshold	-107 dBm over 200 kHz	-116 dBm over 6 MHz
Probability missed detection	≤ 0.1	≤ 0.1
Probability false alarm	≤ 0.1	≤ 0.1
Channel setup/closing time	0.1 second	0.1 second
Channel moving time	2 second	2 second

the adjacent strong TV signals. There are four popular RF filter types.

1. Surface acoustic wave filters [67–72]: A surface acoustic wave (SAW) device is an electromechanical device which uses the piezoelectric effect of non conductive crystal or ceramic materials. SAW devices generally consist of a pair of inter-digital transducers (IDTs) deposited on a piezoelectric substrate. The input IDT converts the electrical signals to mechanical acoustic waves, and the paired IDT receives the propagated acoustic waves and converts them to the corresponding electrical signals. The frequency selectivity of the SAW devices occurs through the energy conversions between the electrical input/output signals and intermediate state mechanical acoustic waves, which are related to the shape and geometry of the IDTs as well as the piezoelectric materials. This frequency selectivity is easily comparable to more than a hundred-pole LC-type network. Therefore, SAW devices are widely used in high performance filter networks in the tens or hundreds MHz frequency range. The harmonic mode operation is exploited in the GHz–range SAW filter applications. Besides its excellent frequency selectivity, SAW devices can be mass produced in compact volume with high reliability.

2. Microelectromechanical system filters [73–80]: Microelectromechanical systems (MEMS) is the technology of integrating mechanical and electrical elements using micro-scale fabrication processes. The major applications can be found in various sensor networks, biological microfluidics, fiber optical components, and wireless RF electronics. In signal processing, a MEMS device shows excellent properties with low loss, high linearity, and the high power handling. The MEMS

filters, built with MEMS resonators, MEMS switches, and capacitive networks, can achieve a wide tuning range with a high quality factor, low insertion loss and high linearity in 0.1 to 10 GHz applications. However, there are some disadvantages of the MEMS filter. Special packaging, separate fabrication processes, and low reliability are generally critical issues in MEMS applications.

3. Distributed element filters [81–86]: A distributed element filter is a type of filter which uses geometric structures instead of the lumped elements such as resistors, capacitors, and inductors to build the desired frequency responses. As the operating frequency goes up, the size of lumped elements is too big, and becomes comparable to the operating wavelength. Therefore, lumped-element implementation is not realistic. In distributed element filters, all the required impedances are acquired by the distributed elements such as a transmission line, and their connections are described by the distributed network theory. Since distributed element filters have multiple passbands, unless carefully controlled, the spurious passbands can introduce interference. Distributed element filters can be categorized into three different types, transmission line filters, waveguide filters, and dielectric resonator filters, and each filter type has lots of different implementations for different frequency responses. In general, distributed element filters show low insertion loss and high power handling ability, but they are often bulky and difficult to integrate with other circuit components.

4. Active filters [87–94]: An active filter means an analog-type filter distinguished by the active components such as an operational amplifier (OPAMP) or an operational transconductance amplifier (OTA). From the desired filter response, the required transfer function can be derived using the well-known functions such as Butterworth, Chebyshev, Elliptic, and Bessel polynomials. Then, the transfer function is embodied by the combination of first and second order structures. There are lots of different types of the first and second order implementations, such as Ackerberg-Mossberg, Sallen-Key, Tow-Thomas, Delyiannis-Friend, etc. With the help of active components, an active filter can get any arbitrary transfer function with an inductor-less network, as well as signal gain. In addition, the resistors can be replaced by a switched-capacitor pair [95–97]. Therefore, the active

filter network is favorable to integrated circuit (IC) implementations. Moreover, it is easily tunable by controlling active components. However, the active filter networks suffer from limited dynamic range, high power consumption, high sensitivity to components and temperature variation. Also, the gain drop of the active components limits high-frequency operation.

1.5 Dissertation Overview

This dissertation mainly focuses on the detection and local oscillator phase noise problems in cognitive radio systems. Due to the large bandwidth of a UWB signal, a CR-based UWB device needs to avoid interference problems with primary users, such as the WiMAX system in the 3 GHz bands. The detection technique using a radiated LO leakage can be useful for a short range communication system, such as the UWB system. Local oscillator phase noise of the detector interacts with an adjacent channel signal, and possibly degrades the detection sensitivity. Accurate analysis can show the underlying mechanism and be useful to estimate the performance degradation due to the resulting in-band interference. The phase noise problem is applied to the CR device operation in the TV bands, where a strong TV signal can desensitize CR devices. A tunable RF filter for interference suppression is presented using a balanced passive complex mixer and a frequency dependent load.

Chapter 2 proposes a mobile terminal detection technique by measuring the low-level leakage signal from a nearby mobile terminal local oscillator. The probabilities of false alarm and missed detection are derived to quantify the detection performance. The technique provides higher sensitivity than a radiometer, and is more robust to estimation error if the power spectral density of the ambient noise is unknown. Systematic limitations on the detection performance are investigated.

Chapter 3 investigates the effects of local oscillator phase noise of a CR-based UWB device on detecting a nearby WiMAX mobile terminal. Spectrum broadening due to the LO phase noise interaction through a multiplier is analyzed, and applied to the situation where the detector receives a significant adjacent channel signal. Accurate expressions for the resulting in-band interference are presented for the adjacent channel

WiMAX signal. The effects of the in-band interference on the detection performance are evaluated with the probabilities of false alarm and missed detection.

Chapter 4 presents a tunable RF notch as well as bandpass filters for interference suppression applications, using a balanced passive complex mixer and a frequency dependent load. The circuit has very wide dynamic range and zero dc-power consumption, and is designed for cognitive radio applications in the IEEE 802.22 system where a strong TV signal can degrade the receiver performance by interacting with local oscillator phase noise.

Chapter 5 concludes the dissertation.

Chapter 2

Mobile Terminal Detection Technique for UWB/WiMAX Coexistence

2.1 Introduction

In 2002, the FCC authorized the unlicensed use of the frequency band from 3.1 to 10.6 GHz for ultra wide-band (UWB) systems [2]. UWB technology can be characterized by its short range of 10 m, low effective isotropic radiation power (EIRP) of -41.25 dBm/MHz, and wide signal bandwidth, as explained in Section 1.2. Since a UWB signal occupies a large bandwidth, its spectrum will likely overlay those of other users, and so an active detection method is necessary to minimize potential interference problems. Even though the spectral mask for the UWB system in Fig. 1.2 was proposed by the FCC to prevent the primary users, the detected UWB signal by a nearby mobile terminal (MT) can be strong enough to create serious interference problems. For instance, the UWB signal power of about -80 dBm over 5 MHz bandwidth at 3 GHz bands is possible if a nearby MT is located 1 m away from the UWB device. This detected UWB signal is about $10 \sim 20$ dB higher than the typical minimum detectable signal (MDS) levels in modern wireless systems.

Worldwide interoperability for microwave access (WiMAX), based on the IEEE 802.16 standard [4], is one of the wireless systems that are expected to share the frequency spectrum with UWB devices, as explained in Section 1.3. In 2005, the IEEE

ratified the 802.16e amendment [5]. This amendment included additional features and attributes to support mobility. The most likely frequencies for mobile WiMAX system are the licensed spectrum bands at 2.3, 2.5, 3.3, and 3.5 GHz [9]. Therefore, the mobile WiMAX system in the 3 GHz frequency band is quite susceptible to potential interference from UWB devices.

This chapter describes an MT detection method utilizing the local oscillator (LO) leakage from a nearby WiMAX MT to avoid the situation where both a WiMAX MT and a UWB device are accessing the same frequency at the same time. An existing application of LO leakage detection is found in [98, 99]. In [98], the LO leakage of a TV receiver is used to detect unlicensed TV viewers. In [99], detecting the LO leakage is used to enable spectrum sharing between a TV and a CR, where the sensor continuously scans the spectrum a TV receiver is tuned to, and then transmits that information to the CR system. In this chapter, we consider direct detection of the LO leakage between mobile terminals. Section 2.2 describes the detection environment, and employs a detection technique using the discrete Fourier transform (DFT). In Section 2.3, we compare the DFT-based detection technique with a radiometer. Section 2.4 investigates several systematic limitations and available remedies to alleviate the performance degradation. The conclusions of this chapter are presented in Section 2.5.

2.2 Mobile Terminal Detection Using Discrete Fourier Transform

In this section, we first outline the detection environment between UWB and WiMAX systems, and then propose a DFT-based detection technique. The performance is described by the probabilities of false alarm (P_{FA}) and missed detection (P_{MD}). The unified equations for the desired P_{FA} and P_{MD} are presented.

2.2.1 Detection Environment

Once a WiMAX channel is set up, there are two synchronized wireless connections — uplink and downlink — between a WiMAX access point (AP) and a WiMAX

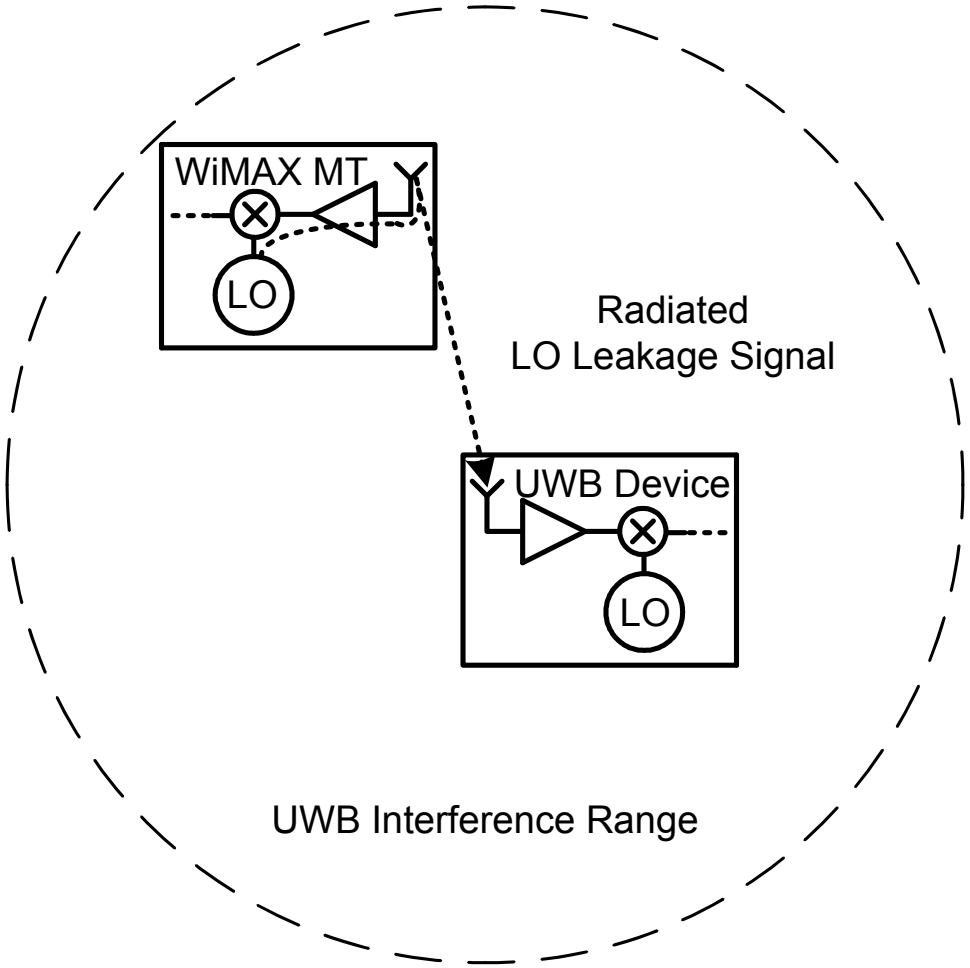

Figure 2.1: Typical coexistence situation where a WiMAX MT is inside the UWB interference range

Table 2.1: Measured LO Leakage Signal Power at the Antenna Port

Wi-Fi Device #1	-72 dBm
Wi-Fi Device #2	-81 dBm
Wi-Fi Device #3	-85 dBm
Wi-Fi Device #4	-90 dBm

MT. Both connections are useful for a UWB device to detect the presence of a WiMAX MT. However, there will be a potential interference problem with an unsynchronized WiMAX MT which does not have a stable wireless connection with a WiMAX AP. The transmitted UWB signal can be harmful for an unsynchronized WiMAX MT in the sense of preventing it from receiving a signal from a WiMAX AP. Therefore, a UWB device *also* needs a method to detect a nearby unsynchronized WiMAX MT, which is within its interference range. The unsynchronized condition can occur when an MT awakens from the *unavailable interval* in either *sleep* or *idle* mode, or when an MT enters or registers with the network [5, 9].

As shown in Fig. 2.1, the proposed detection technique utilizes the LO leakage from a nearby unsynchronized WiMAX MT. An unsynchronized WiMAX MT continuously scans the possible downlink channels until it establishes a stable synchronized wireless connection with a WiMAX AP [4, 5]. A small portion of the WiMAX MT receiver LO signal leaks to the antenna and radiates when it is scanning. A UWB detector can use this LO leakage to determine the presence of a nearby MT receiver. The received LO leakage is generally very weak, and so the sensitivity of the UWB detector is a great concern. Typically, an LO leakage power of -90 to -70 dBm at the WiMAX MT receiver antenna port is expected by considering the reverse isolation of the receiver front-end RF sections [100, 101], and a path loss of 60 to 80 dB for 10 m distance is expected in an indoor environment [12, 102]. The LO leakage powers were measured at the antenna ports for some typical, off-the-shelf, Wi-Fi devices, and found to lie between -90 and -72 dBm, as shown in Table 2.1.

In order to avoid DC offset, flicker noise, and even-order distortion problems, a low-IF architecture for a WiMAX receiver was proposed [103, 104]. However, the WiMAX OFDM signal does not transmit any data using the DC subcarrier, as shown in Fig. 1.4, and also the excellent performance in integration and power saving makes

direct conversion architecture more attractive [105–111]. Moreover, the multi-band and multi-standard receiver highly favors a direct conversion architecture to combine separate receiver path [108–111]. Therefore, a direct conversion type receiver will be predominant for future hand-held devices. The proposed detection technique will be most effective when the WiMAX receiver employs a direct conversion type receiver. Since the frequency of the WiMAX receiver LO is centered at the corresponding WiMAX downlink channel, a UWB detector can directly map the spectrum information of the captured LO leakage to the channel the WiMAX MT listens to. In case the WiMAX MT device utilizes a heterodyne receiver, then the intermediate frequency (IF) must be known *a priori* to estimate the frequency of the LO leakage signal.

As a simplified detector architecture, Fig. 2.2 shows a heterodyne receiver, which removes the frequency ambiguity between the received WiMAX MT LO leakage and the UWB detector's own LO leakage. The signal in the IF band is downconverted to baseband via quadrature mixing in Fig. 2.2.

2.2.2 Magnitude Response of the Discrete Fourier Transformation

The received signal at the UWB antenna, $r(t)$, can be described by one of the following two hypotheses:

$$H_0 : \ r(t) = n_W(t) \tag{2.1a}$$

or

$$H_1 : \ r(t) = s_L(t) + n_W(t) \tag{2.1b}$$

where $s_L(t)$ and $n_W(t)$ denote the received LO leakage from a nearby unsynchronized WiMAX MT and an AWGN, respectively. The detector downconverts $r(t)$ to baseband, and performs a DFT, as shown in Fig. 2.2. The gain of the receiver path from the antenna to baseband in unity, and the narrowband intermediate frequency filter (IFF) defines the bandwidth of the detector. We use an ideal rectangular filter responses for simplicity of analysis. However, we will compare the resulting system performance with the performance when the lowpass equivalent of the IFF is implemented by a 10th order Chebyshev lowpass filter with 100 kHz bandwidth and 0.5 dB passband ripple [87, 88].

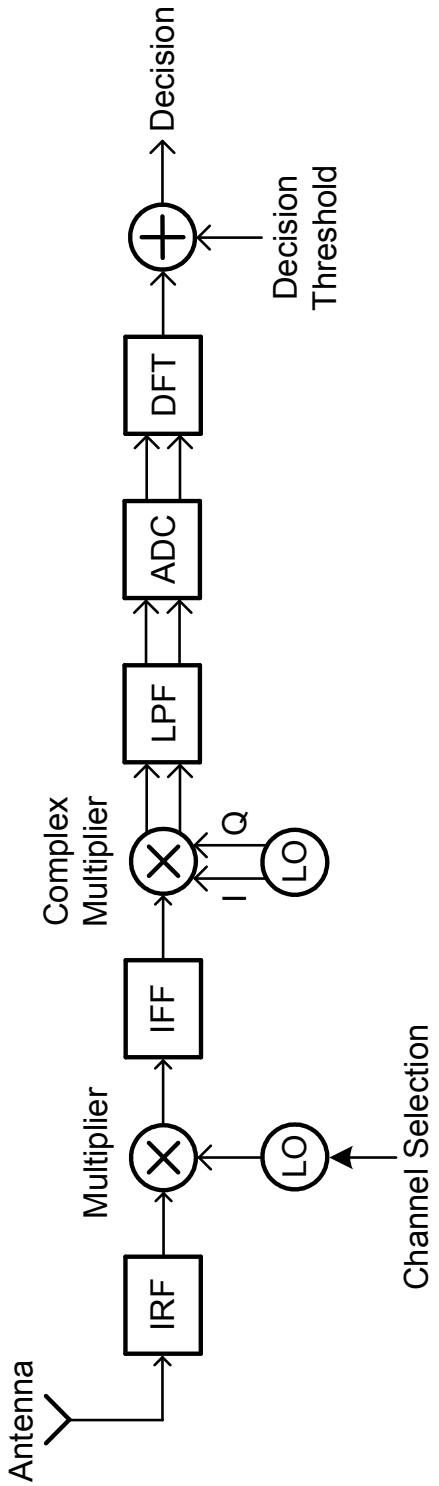

Figure 2.2: Proposed detector architecture. The blocks IRF, IFF, LPF, and ADC denote the image rejection filter, intermediate frequency filter, lowpass filter, and analog-to-digital converter, respectively.

The received LO leakage at a CR-based UWB MT, denoted by $s_L(t)$, is an unmodulated frequency tone, and can be written as

$$s_L(t) = A_L \cos(\omega_L t + \theta_L) \tag{2.2}$$

where A_L, ω_L, and θ_L denote the amplitude, frequency, and arbitrary random phase of the received LO leakage, respectively. After downconverting and sampling, the baseband discrete sequence of the received LO leakage, denoted by $s_D[m]$, is described by

$$s_D[m] = A_L \exp(j[2\pi f_D m + \theta_D), \quad m \in [0,\ M-1] \tag{2.3}$$

where M denotes the number of samples. The discrete-time frequency, f_D, is the ratio of the frequency of the baseband LO leakage to the sampling frequency. The uniformly distributed random phase, θ_D, accounts for an arbitrary phase mismatch between the received LO leakage and the UWB detector's LO signals.

The baseband discrete sequence of the received noise signal, denoted by $n_D[m]$, can be described by

$$n_D[m] = n_1[m] + jn_2[m], \quad m \in [0,\ M-1] \tag{2.4}$$

where $n_1[m]$ and $n_2[m]$ are independent zero-mean Gaussian discrete random processes with variance of σ_n^2. If $n_1[m]$ and $n_2[m]$ result from Nyquist-rate sampling of their continuous-time counterparts, the M samples of both $n_1[m]$ and $n_2[m]$ are independent [112].

Let $S[k]$ and $N[k]$ be the M-point DFT responses to $s_D[m]$ and $n_D[m]$, respectively. With this model, under hypothesis H_0, the probability density function (PDF) for the magnitude response of $N[k]$ is given by

$$f_{|N[k]|}(x) = \frac{x}{M\sigma_n^2} \exp\left(-\frac{x^2}{2M\sigma_n^2}\right). \tag{2.5}$$

Under hypothesis H_1, if we initially assume that the product of Mf_D is an integer, the signal energy of $s_D[m]$ is accumulated at one frequency bin, say the k^{th}. Then, the PDF for the magnitude response of $S[k] + N[k]$ is given by

$$f_{|S[k]+N[k]|}(x) = \frac{x}{M\sigma_n^2} \exp\left(-\frac{x^2 + (A_L M)^2}{2M\sigma_n^2}\right) I_0\left(\frac{A_L x}{\sigma_n^2}\right) \tag{2.6}$$

where I_y is the modified Bessel function of the first kind and order y [113].

2.2.3 Detector Performance

A false alarm occurs when only noise is present at the input, but at least one of the DFT outputs exceeds a pre-determined decision threshold. In a particular frequency bin, whose density is given by (2.5), the probability P_C that its magnitude response does not exceed the threshold is given by

$$P_C = 1 - \exp\left(-\frac{D_{TH}^2}{2M\sigma_n^2}\right) \tag{2.7}$$

where D_{TH} denotes the pre-determined decision threshold. Then, P_{FA} for M frequency bins is given by

$$\begin{aligned} P_{FA} &= 1 - (P_C)^M \\ &= 1 - \left[1 - \exp\left(-\frac{R_{TH}}{M}\right)\right]^M \end{aligned} \tag{2.8}$$

where R_{TH} is the power ratio between D_{TH} and the baseband noise (i.e., $R_{TH} = D_{TH}^2/2\sigma_n^2$). Figure 2.3 shows the P_{FA} variation with R_{TH} for different values of M. The P_{FA} simulation results using the 10th order Chebyshev lowpass filter are compared with the analytical result in (2.8), and good agreement can be observed in Fig. 2.3.

On the other hand, a missed detection occurs when there is an LO leakage at the input, but all of the DFT magnitude responses are below the pre-determined decision threshold. For the frequency bin corresponding to f_D, whose density is given by (2.6), the error probability $P_{E(f_D)}$ that its magnitude response does not exceed the threshold is given by

$$P_{E(f_D)} = 1 - Q\left(\sqrt{2M\lambda}, \sqrt{\frac{2R_{TH}}{M}}\right) \tag{2.9}$$

where Q indicates the Marcum Q-function [113], and λ is the input signal-to-noise ratio (SNR), given by

$$\lambda = \frac{A_L^2}{2\sigma_n^2}. \tag{2.10}$$

For the other $M - 1$ frequency bins, the error probability, denoted by P_E, is the same as

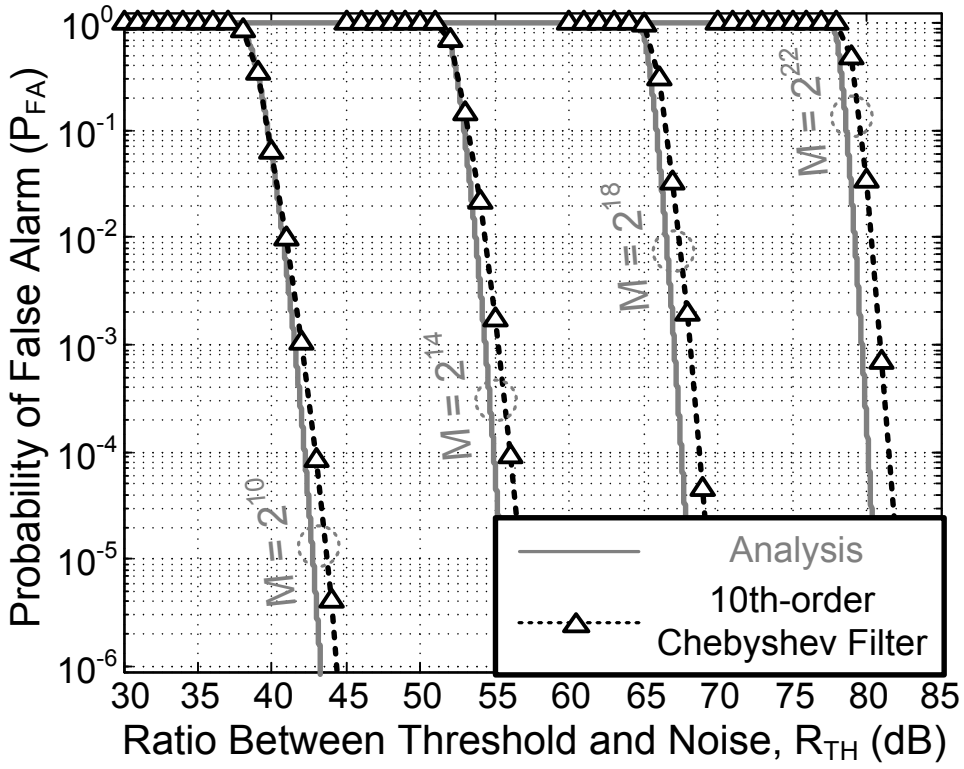

Figure 2.3: Probability of false alarm. The quantity M denotes the number of samples.

(2.7). Combining (2.7) and (2.9), the P_{MD} for M frequency bins is given by

$$\begin{aligned} P_{MD} &= (P_E)^{M-1} \times P_{E(f_D)} \\ &= \left[1 - \exp\left(-\frac{R_{TH}}{M}\right)\right]^{M-1} \left[1 - Q\left(\sqrt{2M\lambda}, \sqrt{\frac{2R_{TH}}{M}}\right)\right]. \end{aligned} \tag{2.11}$$

Figure 2.4 shows the P_{MD} variation with input SNR for different combinations of M and R_{TH}. The P_{MD} simulation results using the 10th order chebyshev lowpass filter are compared with the analytical result in (2.11), and again good agreement can be observed in Fig. 2.4.

From (2.8), the required decision threshold for a desired P_{FA} is given by

$$D_{TH(req)} = \sqrt{-2M\sigma_n^2 \ln\left[1 - (1 - P_{FA(des)})^{\frac{1}{M}}\right]}. \tag{2.12}$$

Using (2.12) in (2.11), P_{MD} can be related to the desired P_{FA} by

$$P_{MD} = \left[1 - P_{FA(des)}\right]^{\frac{M-1}{M}} \left[1 - Q\left(\sqrt{2M\lambda}, \sqrt{-2\ln\left[1 - (1 - P_{FA(des)})^{\frac{1}{M}}\right]}\right)\right]. \tag{2.13}$$

For a large M and a small desired P_{FA}, (2.13) can be approximated as

$$P_{MD} \approx 1 - Q\left(\sqrt{2M\lambda}, \sqrt{-2\ln\left[1 - (1 - P_{FA(des)})^{\frac{1}{M}}\right]}\right). \tag{2.14}$$

As expected, P_{MD} is dominated by the input SNR. As shown in Fig. 2.5, the proposed detection technique requires samples from 2^{10} to 2^{23} to simultaneously satisfy the desired P_{FA} and P_{MD} of 10^{-2} to 10^{-6} for a detection range of 10 m, 5 dB noise figure of the receiver, and 200 kHz IFF bandwidth. The free space path loss of a 3.5 GHz LO leakage is used to generate the received leakage signal power in Fig. 2.5.

2.3 Comparison with Radiometer Detection

In this section, we compare a radiometer with the detector presented in Section 2.2.

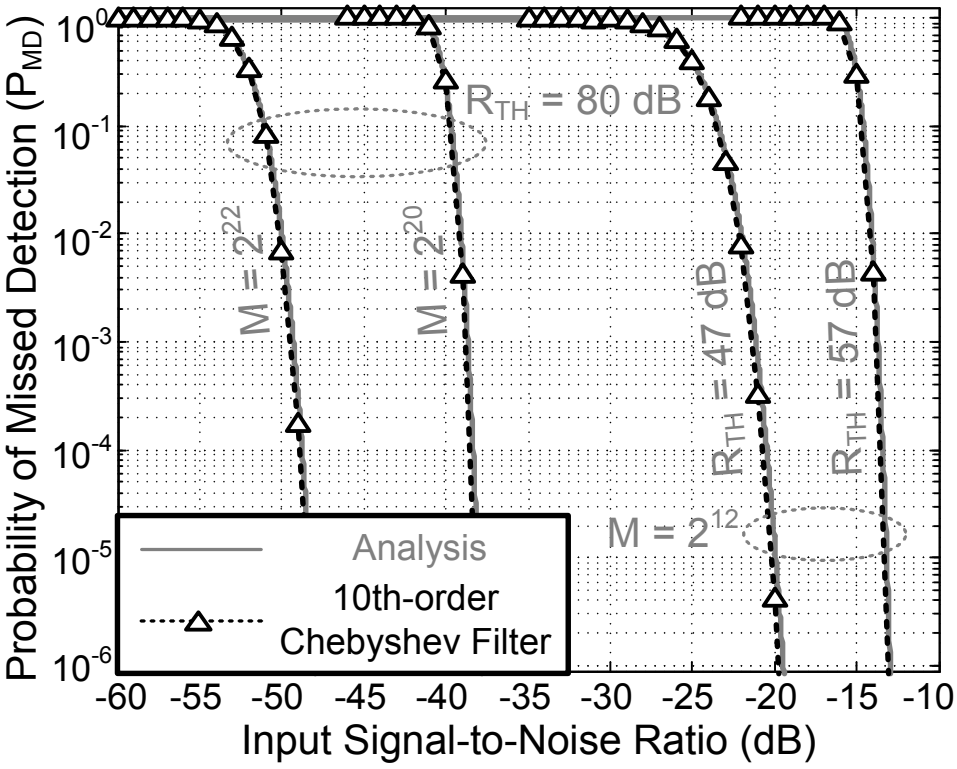

Figure 2.4: Probability of missed detection. The quantities M and R_{TH} denote the number of samples and the power ratio between the pre-determined decision threshold and baseband noise, respectively.

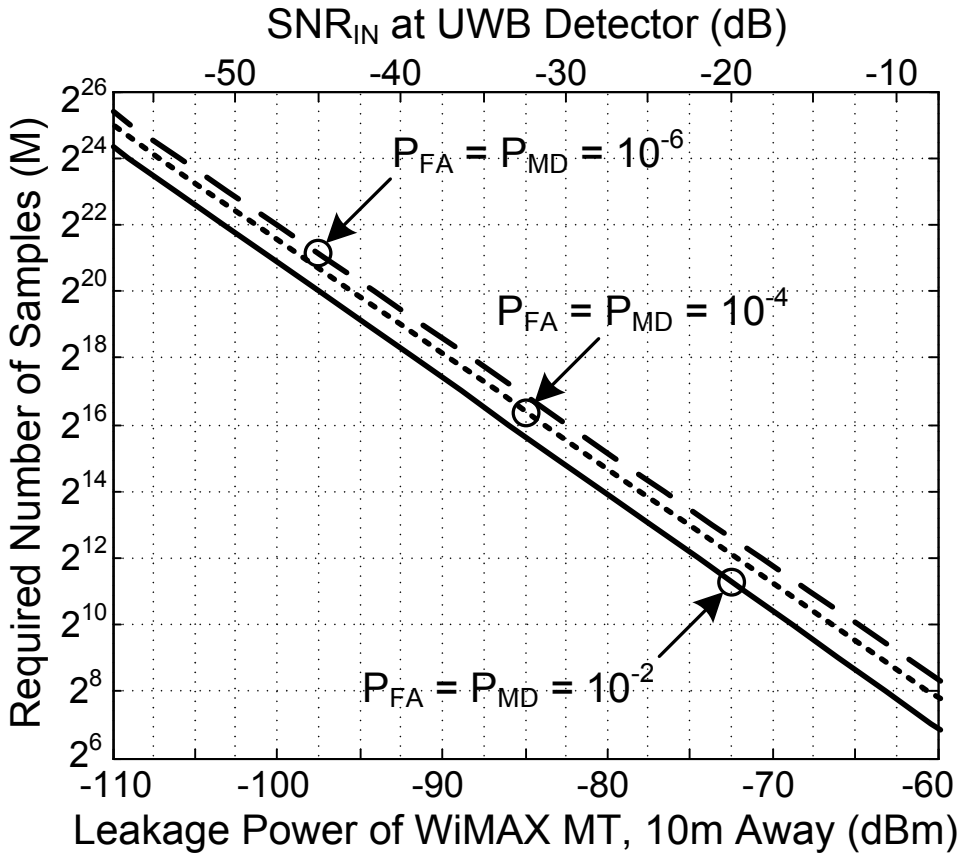

Figure 2.5: Required number of samples for the detection of the leakage signal from a WiMAX at 10 m distance, assuming the free space path loss of a 3.5 GHz LO leakage signal, 5 dB noise figure of the receiver, and 200 kHz bandwidth of the intermediate frequency filter.

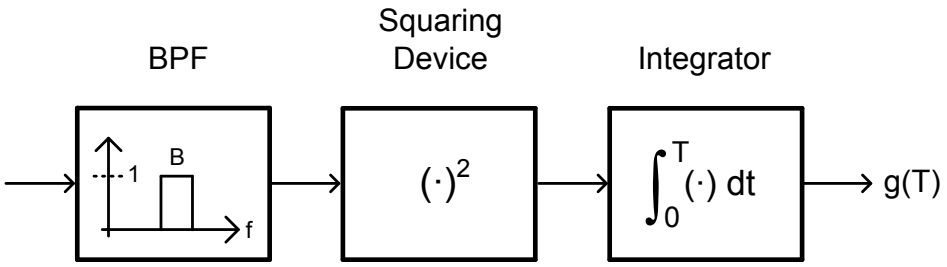

Figure 2.6: Radiometer block diagram. The quantity B denotes the bandwidth of the bandpass filter

2.3.1 Detector Sensitivity

The performance of a radiometer is well established [6, 39, 40]. As shown in Fig. 2.6, a typical radiometer consists of a bandpass filter (BPF) followed by a square-law device and a finite time integrator. We assume that the BPF has an ideal rectangular frequency response with a magnitude of unity and a bandwidth of B Hz.

Under hypothesis H_0, the output of the integrator, $g_0(T)$, over the interval $(0,\ T)$ is approximated as being Gaussian [39]. That is

$$g_0(T) \sim \mathcal{N}\left(\eta_0 M,\ \eta_0^2 M\right) \tag{2.15}$$

where η_0 denotes the single-sided PSD of the AWGN. The number of samples, M, is equivalent to the integer part of the product of TB, based on the Nyquist rate sampling theorem. Thus, for a given threshold level of D_{TH}, P_{FA} is given by [39]

$$P_{FA} = \phi\left(-\frac{D_{TH} - \eta_0 M}{\sqrt{\eta_0^2 M}}\right) \tag{2.16}$$

where $\phi(x)$ indicates the cumulative distribution function for a normalized Gaussian random variable [113].

Under hypothesis H_1, the received LO leakage, given by (2.2), passes through the BPF without any attenuation. Then, the output of the integrator, $g_1(T)$, is given by [39]

$$g_1(T) \sim \mathcal{N}\left(\eta_0(1+\lambda)M,\ \eta_0^2(1+2\lambda)M\right), \tag{2.17}$$

and P_{MD} is given by [39]

$$P_{MD} = \phi\left(\frac{D_{TH} - \eta_0(1+\lambda)M}{\sqrt{\eta_0^2(1+2\lambda)M}}\right). \tag{2.18}$$

Combining (2.16) and (2.18), for the desired P_{FA}, we have

$$P_{MD} = \phi\left(-\frac{\phi^{-1}\left(P_{FA(des)}\right) + \lambda\sqrt{M}}{\sqrt{1+2\lambda}}\right). \tag{2.19}$$

Comparing (2.13) with (2.19), Fig. 2.7 shows the required M for the DFT-based detector and the radiometer to simultaneously satisfy the desired P_{FA} and P_{MD} for the same system bandwidth of 200 kHz. The superior sensitivity of the DFT-based detector for low SNR input aids the detection of the weak LO leakage. Another useful method to assess the detection sensitivity is the receiver operating characteristic (ROC) curve, which displays the probability of detection (P_D) versus P_{FA}. Figure 2.8 compares the ROC curves of the radiometer and the DFT-based detector.

2.3.2 Detector Sensitivity to Noise Uncertainty

The detection performance of the radiometer, given by (2.16) and (2.18), can be limited if the PSD of the ambient noise, η_0, is unknown [6, 40, 42]. In order to quantify the effect of the estimation error, we take the approach of [40], and assume that the estimate $\widehat{\eta_0}$ can be upper and lower bounded by

$$(1-\epsilon_1)\eta_0 \leq \widehat{\eta_0} \leq (1+\epsilon_2)\eta_0 \tag{2.20}$$

where the boundary uncertainties ϵ_1 and ϵ_2 are given by [40]

$$0 \leq \epsilon_1 < 1 \tag{2.21}$$

$$0 \leq \epsilon_2 \tag{2.22}$$

Given this uncertainty range, the worst case P_{MD} for the desired P_{FA} is given by [40]

$$P_{MD(worst)} = \phi\left(\frac{\sqrt{M}(U-1-\lambda) - U\phi^{-1}\left(P_{FA(des)}\right)}{\sqrt{1+2\lambda}}\right). \tag{2.23}$$

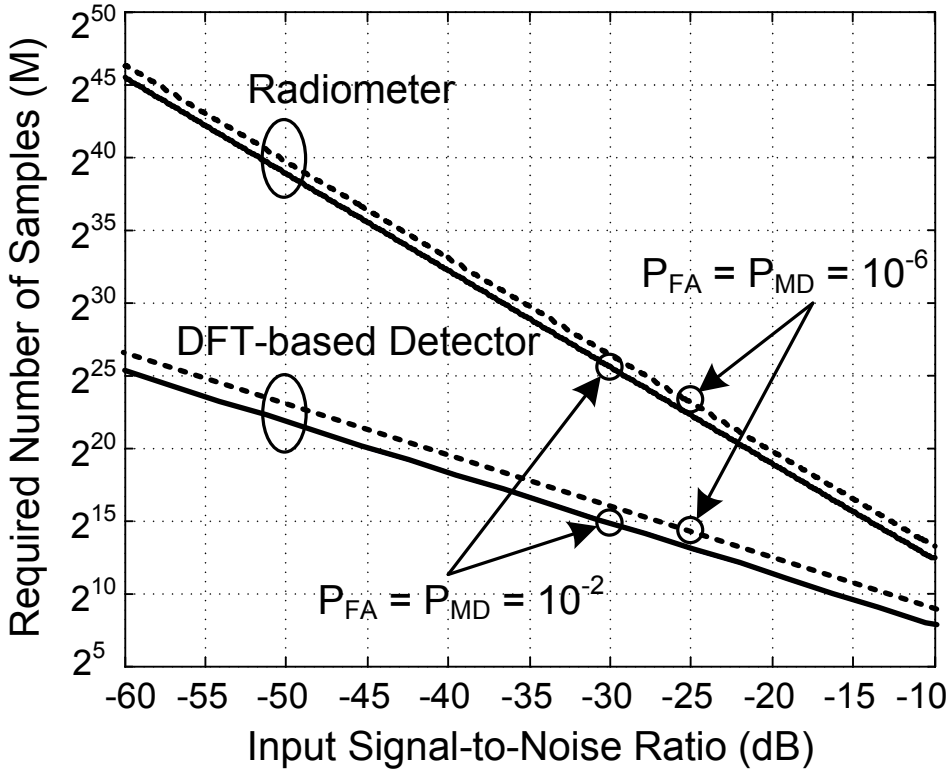

Figure 2.7: Required number of samples for the radiometer and DFT-based detector.

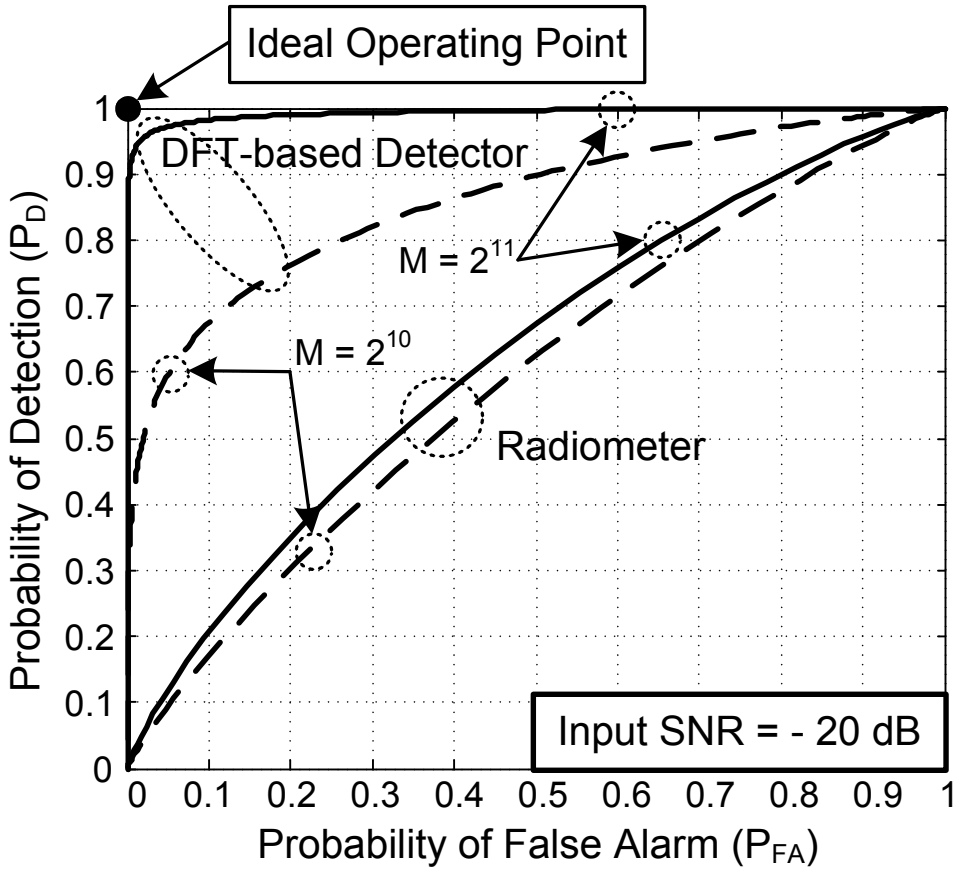

Figure 2.8: Receiver operating characteristic curves for the radiometer and DFT-based detector. The quantity M denotes the number of samples

In (2.23), U denotes the ratio of the peak-to-peak noise uncertainty [40], defined by

$$U = \frac{1+\epsilon_2}{1-\epsilon_1} \geq 1. \tag{2.24}$$

If $\lambda \leq U-1$, there is a boundary in the $P_{MD(worst)}$ response. This boundary, denoted by $P_{MD(worst)\_min}$, indicates the minimum achievable $P_{MD(worst)}$ in (2.23), which cannot be overcome by increasing M. The $P_{MD(worst)\_min}$ can be found when $\lambda = U-1$, and is given by

$$P_{MD(worst)\_min} = \phi\left(-\frac{U\phi^{-1}\left(P_{FA(des)}\right)}{\sqrt{1+2(U-1)}}\right). \tag{2.25}$$

Since (2.25) is limited by U and $P_{FA(des)}$, a radiometer cannot simultaneously satisfy both the desired P_{FA} and P_{MD}, even with an infinite number of samples, if the desired P_{MD} is smaller than (2.25).

If $\lambda > U-1$, any $P_{MD(worst)}$ can be achieved for a given λ by adjusting M in (2.23). Therefore, in order to simultaneously satisfy both the desired P_{FA} and P_{MD}, there is the minimum required λ, denoted by SNR_{min} [40], defined by

$$SNR_{min} = U-1. \tag{2.26}$$

Figure 2.9 shows the serious degradation of the radiometer detection sensitivity due to the noise uncertainty. Even with just little noise uncertainty ratio of 0.001 dB, the detection ability is bounded by SNR_{min} of -37 dB in Fig. 2.9. If the received LO leakage does not satisfy this minimum required SNR, the radiometer may fail to make a correct decision of the presence of a nearby MT.

Now consider the DFT-based detector. Using the same boundary conditions as (2.20), the biased decision threshold for the desired P_{FA} in the DFT-based detector, derived from (2.12), is

$$D_{TH(req)} = \sqrt{-\frac{2\widehat{\eta_0}MB_{IF}}{1-\epsilon_1}\ln\left[1-\left(1-P_{FA(des)}\right)^{\frac{1}{M}}\right]}. \tag{2.27}$$

Note that the variance of the noise samples, σ_n^2, is replaced by $\eta_0 B_{IF}$, where B_{IF} denotes the IFF bandwidth. Using (2.27) in (2.13), the $P_{MD(worst)\_min}$ for the DFT-based detector

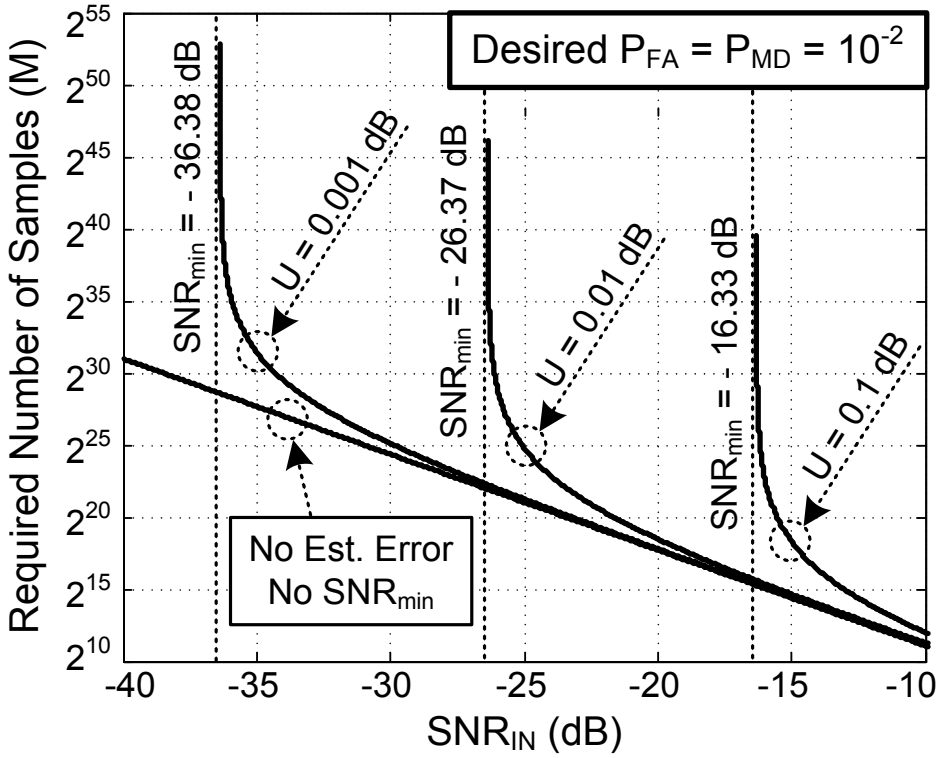

Figure 2.9: Effect of the noise uncertainty on the Radiometer [6]. The quantity U denotes the ratio of the peak-to-peak noise uncertainty.

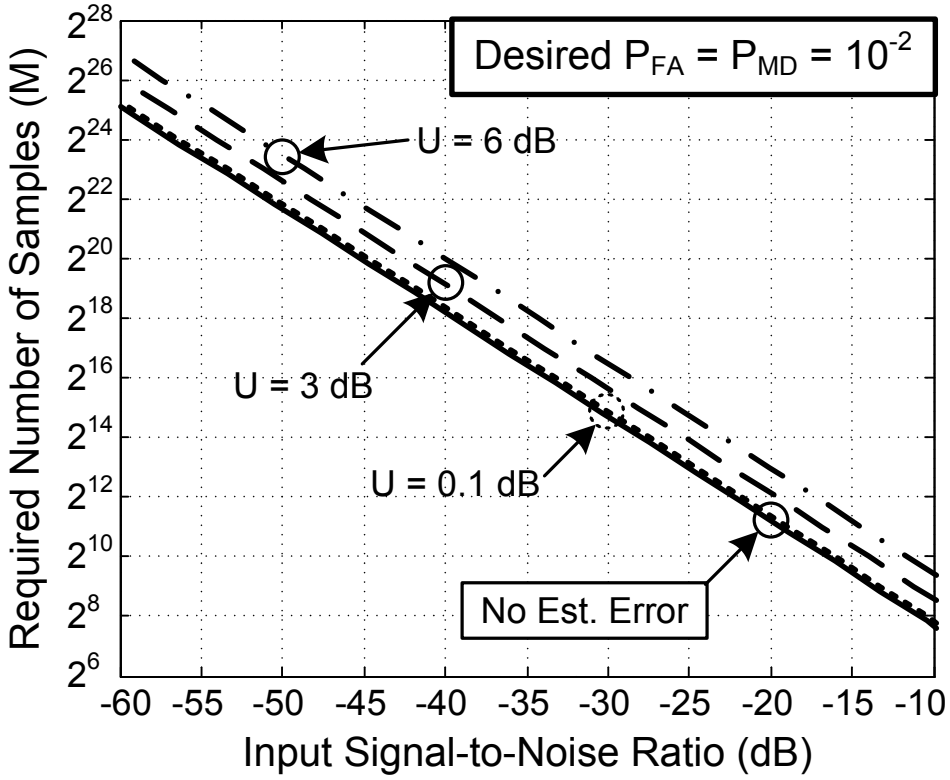

Figure 2.10: Effect of the noise uncertainty on the DFT-based detector. The quantity U denotes the ratio of the peak-to-peak noise uncertainty.

is given by

$$P_{MD(worst)} = \left[1 - \left(1 - (1 - P_{FA(des)})^{\frac{1}{M}}\right]^{U}\right)^{M-1} \times \left[1 - Q\left(\sqrt{2M\lambda}, \sqrt{-2U\ln\left[1 - (1 - P_{FA(des)})^{\frac{1}{M}}\right]}\right)\right]. \quad (2.28)$$

For a large M and a small desired P_{FA}, (2.28) can be approximated as

$$P_{MD(worst)\_min} \approx 1 - Q\left(\sqrt{2M\lambda}, \sqrt{-2U\ln\left[1 - (1 - P_{FA(des)})^{\frac{1}{M}}\right]}\right). \quad (2.29)$$

Figure 2.10 illustrates the required number of samples for the DFT-based detector with different values of U. Contrary to the radiometer, the estimation error does not result in any detection limitation for an arbitrary λ, even though the DFT-based detector requires more samples to overcome the biased decision threshold in (2.29).

The fundamental difference between the radiometer and the DFT-based detector can be explained by the dependence on M of the noise and the signal-plus-noise responses. From (2.15) and (2.17), the expected output of the radiometer integrator increases linearly with M. However, for the DFT-based detector, there is a difference in behavior of the magnitude responses of the DFT frequency bins for noise and signal-plus-noise inputs.

From (2.5), the expected DFT magnitude response to noise input is proportional to $\sqrt{M}$ and given by

$$E\left[|N[k]|\right] = \sqrt{\frac{\pi}{2} M \sigma_n^2}. \tag{2.30}$$

For the signal-plus-noise input, only one DFT frequency bin carries information about the received LO leakage, assuming the product of Mf_D is an integer. From (2.6), the expected magnitude response of that frequency bin is given by

$$\begin{aligned} E\left[|S[k]+N[k]|\right] =& \sqrt{\frac{\pi}{2} M \sigma_n^2} \left[\left(1 + \frac{A_L^2 M}{2\sigma_n^2} \right) I_0 \left(\frac{A_L^2 M}{4\sigma_n^2} \right) \right] \exp\left(-\frac{A_L^2 M}{4\sigma_n^2} \right) \\ &+ \sqrt{\frac{\pi}{2} M \sigma_n^2} \left[\frac{A_L^2 M}{2\sigma_n^2} I_1 \left(\frac{A_L^2 M}{4\sigma_n^2} \right) \right] \exp\left(-\frac{A_L^2 M}{4\sigma_n^2} \right). \end{aligned} \tag{2.31}$$

In (2.31), the modified Bessel function can be approximated for either large SNR or large M. For a large x, the modified Bessel function can be approximated as [114]

$$I_y(x) \approx \frac{\exp(x)}{\sqrt{2\pi x}}. \tag{2.32}$$

Using (2.32) in (2.31), the expected magnitude response is approximately given by

$$E\left[|S[k]+N[k]|\right] \approx A_L M. \tag{2.33}$$

The expected DFT magnitude response for the frequency bin corresponding to f_D increases approximately linearly with M, but the biased decision threshold is proportional to $\sqrt{M}$ as shown in (2.27). Therefore, the estimation error of the ambient noise PSD can be overcome by increasing M.

2.4 Limitations on the Detection Performance

There are several systematic limitations on the detection performance. In this section, those limitations are introduced, and available remedies are investigated.

2.4.1 Frequency Drift of the LO and Minimum Frame Duration of the Mobile WiMAX System

When the decision threshold is pre-determined for the desired P_{FA}, P_{MD} becomes a function of the input SNR, λ, and the number of samples, M. Therefore, in (2.14), both λ and M should be large enough to detect the weak power of a received LO leakage. The frequency mismatch of the LO signals between the WiMAX MT receiver and the UWB detector places a limit on the minimum detector bandwidth. The bandwidth of the UWB detector should be wide enough to cover this frequency mismatch, but simultaneously as narrow as possible to minimize the noise bandwidth. The frequency instability of the LO signal is a dominant source of the frequency mismatch problem. A typical LO has a frequency accuracy of roughly $\pm$10 ppm [115, 116], which corresponds to a frequency uncertainty of 70 kHz for a 3.5 GHz LO. Since the frequency uncertainties for the LO signals of the WiMAX MT receiver and the UWB detector are independent, the bandwidth of the detector should be greater than at least 140 kHz. In addition, any changes in parameters, such as temperature or Doppler frequency shift, during the observation time can result in additional frequency uncertainties. However, those are usually negligible when compared with the frequency instability of LO signals when we consider the required detector bandwidth.

Once the system bandwidth is determined, the UWB detector should use enough samples to satisfy the desired P_{MD} with the low input SNR. From (2.14), it is seen that the required number of samples should vary inversely with the input SNR for a given P_{MD}. However, there is a limitation to the available number of samples because the operation of an unsynchronized MT depends on the pre-determined frame pattern in WiMAX system. The minimum value of the pre-determined frame duration is that of two MAC frames, and the maximum is undefined [4, 5]. The IEEE 802.16 standard provides frame durations from 2 ms to 20 ms [4, 5]. For Mobile WiMAX system, the frame duration of 5 ms is common [9], which corresponds to an M of 10^3 with a sampling frequency of 200 kHz. Since the pre-determined frame duration cannot be arbitrarily long for a UWB device, the limited observation time can become a system bottleneck. Also, the arbitrary on and off signal pattern of the radiated LO leakage can make the detection more difficult because only a fraction of the samples include the received LO leakage.

The smaller number of effective samples can result in insufficient energy of the LO leakage accumulated in the DFT frequency bin, and so the UWB detector requires a longer observation time than what is expected in Fig. 2.5. Therefore, the co-existence problem requires cooperation between the WiMAX and UWB systems to ensure that either the frame duration is sufficiently long, or the power of the LO leakage is sufficiently strong for a UWB detector to accurately detect the presence of an unsynchronized WiMAX MT.

The variations of the Doppler frequency shift and temperature during the observation time can result in the frequency variation in the DFT responses. These short-time frequency variations are usually negligible in determining the require detector bandwidth. However, they can degrade the detection performance, especially when the required number of samples is large. When the velocity of the WiMAX MT is varying, the variation of the Doppler frequency shift makes the energy of the received LO leakage spread over more than one frequency bin in the DFT response [117]. The degradation of the detection performance depends on the acceleration rate of the WiMAX MT. If the maximum acceptable acceleration rate, denoted by $R_{ACC(max)}$, is defined as the acceleration rate which results in the variation of the Doppler frequency shift equal to one frequency step in the DFT response, then $R_{ACC(max)}$ is given by

$$R_{ACC(max)} = \frac{f_S^2 c}{M^2 f_R} \tag{2.34}$$

where f_S, f_R, and c denote the sampling frequency, the frequency of the radiated LO leakage, and the speed of light, respectively. The temperature variation can be examined similarly. If the maximum acceptable temperature coefficient, denoted by $C_{T(max)}$, is defined as the temperature coefficient which results in the frequency variation of the LO leakage for the given temperature variation equal to one frequency step in the DFT response, then $C_{T(max)}$ is given by

$$C_{T(max)} = \frac{f_S^2}{M^2 f_R R_T} \tag{2.35}$$

where R_T denotes the temperature variation rate. Figure 2.11 shows the variation of $R_{acc(max)}$ and $C_{T(max)}$ with M for f_S of 200 kHz, f_R of 3.5 GHz, and R_T of 2 °C/minute.

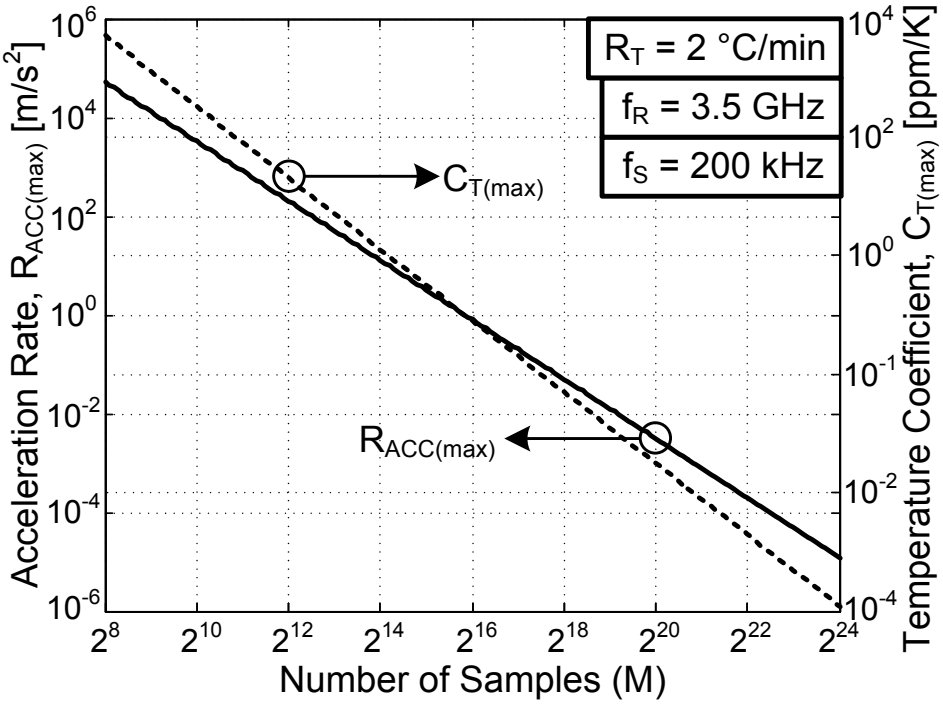

Figure 2.11: Maximum acceptable acceleration rate and temperature coefficient of the WiMAX MT. The quantities R_T, f_R, and f_S denote the temperature variation rate, the frequency of the radiated LO leakage, and the sampling frequency, respectively.

As the number of samples increases, the detection performance becomes more susceptible to the Doppler frequency shift and temperature variation.

2.4.2 Finite DFT Resolution

The probability of missed detection given by (2.11) is valid only when the product Mf_D is an integer. For a non-integer value of Mf_D the M-point DFT responses to $s_D[m]$ in (2.3) are given by

$$S[k] = A_L \frac{\sin(\pi(Mf_D - k))}{\sin(\pi(Mf_D - k)/M)} \exp\left(j\pi(Mf_D - k)\left(1 - 1/M\right) + j\theta_D\right) \tag{2.36}$$

where $k \in [0,\ M-1]$. The signal energy spreads over all M frequency bins when the product Mf_D is not an integer [118]. Then, the PDF for the magnitude response of $S[k] + N[k]$, under hypothesis H_1, is given by

$$f_{|S[k]+N[k]|}(x) = \frac{x}{M\sigma_n^2} \exp\left(-\frac{x^2 + |S[k]|^2}{2M\sigma_n^2}\right) I_0\left(\frac{|S[k]|x}{M\sigma_n^2}\right). \tag{2.37}$$

Therefore, the general expression of P_{MD} for M frequency bins is given by

$$P_{MD} = \prod_{k=0}^{M-1} P_E[k] \tag{2.38}$$

where

$$P_E[k] = 1 - Q\left(\sqrt{\frac{|S[k]|^2}{M\sigma_n^2}}, \sqrt{\frac{2R_{TH}}{M}}\right). \tag{2.39}$$

Unlike the P_{MD} of (2.11), the P_{MD} of (2.38) is a function of Mf_D, as shown in Fig. 2.12. The worst P_{MD} degradation is observed when the fractional part of Mf_D is 0.5, and it is equivalent to an input SNR degradation of approximately 2.5 dB for a P_{MD} of 10^{-3}. This dependence of P_{MD} on the product of Mf_D is inherently due to the finite number of samples in the DFT. This finite number of samples limits the frequency resolution of the DFT responses, and so the signal energy leaks into all M frequency bins.

The P_{MD} degradation due to the finite frequency resolution can be improved by augmenting the given M samples with an all-zero sequence, known as zero-padding

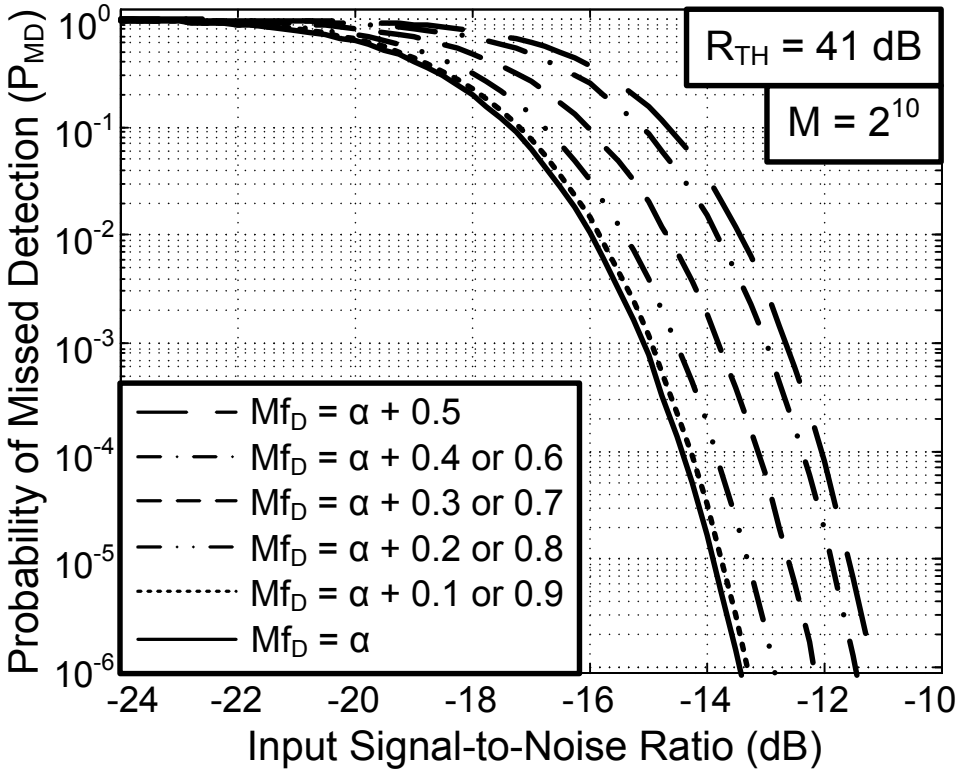

Figure 2.12: Variation of probability of missed detection for non-integer values of the product of Mf_D. The quantities α, M, f_D, and R_{TH} denote an arbitrary integer, the number of samples, the discrete-time frequency, and the power ratio between the pre-determined decision threshold and baseband noise, respectively.

[118]. Suppose that a sequence of M zeros is appended to $s_D[m]$ in (2.3). Then, the $2M$-point DFT responses to the zero-padded sequence are given by

$$S_{ZP}[k] = A_L \frac{\sin(\pi(2Mf_D - k/2))}{\sin(\pi(2Mf_D - k/2)/M)} \exp\left(j\pi(2Mf_D - k/2)\left(1 - 1/M\right) + j\theta_D\right) \tag{2.40}$$

where $k \in [0,\ 2M-1]$. Figure 2.13 shows the peak magnitude variations in the DFT responses with and without the padded zero sequence of length M. Since the frequency resolution of the DFT response is doubled, the peak magnitude variation is reduced. In comparing Fig. 2.12 with Fig. 2.13, it can be seen that the degradation of P_{MD} is dominated by the peak magnitude response of the $S[k]$. Since the degradation of the peak magnitude response is mitigated by the appended zero sequence, as shown in Fig. 2.13, the P_{MD} degradation can be mitigated by the appended zero sequence. The worst P_{MD} degradation for the zero-padded sequence is expected when the fractional part of Mf_D is either 0.25 or 0.75. In Fig. 2.14, the P_{MD} simulation results using the 10th order Chebyshev lowpass filter with and without the appended zero sequence of length M are compared with the analytical result in (2.38). It is observed in Fig. 2.14 that the P_{MD} degradation due to a non-integer value of Mf_D is alleviated by the appended zero sequence.

When there is no LO leakage at the input, the $2M$-point DFT responses to the zero-padded noise sequence are given by

$$\begin{aligned} N_{ZP}[k] &= \sum_{m=0}^{M-1} n_D[m] \exp\left(-j\frac{\pi k}{M}m\right),\ k \in [0,\ 2M-1] \\ &= N_{ZP1}[k] + jN_{ZP2}[k] \end{aligned} \tag{2.41}$$

where $N_{ZP1}[k]$ and $N_{ZP2}[k]$ denote the real and imaginary part of $N_{ZP}[k]$, respectively. The autocorrelation of either $N_{ZP1}[k]$ or $N_{ZP2}[k]$ and the crosscorrelation between $N_{ZP1}[k]$ and $N_{ZP2}[k]$ can be shown to equal

$$R_{N_{ZP1}}[\tau] = R_{N_{ZP2}}[\tau] = \sigma_n^2 \sum_{m=1}^{M-1} \cos\left(\frac{\pi}{M}m\tau\right) \tag{2.42}$$

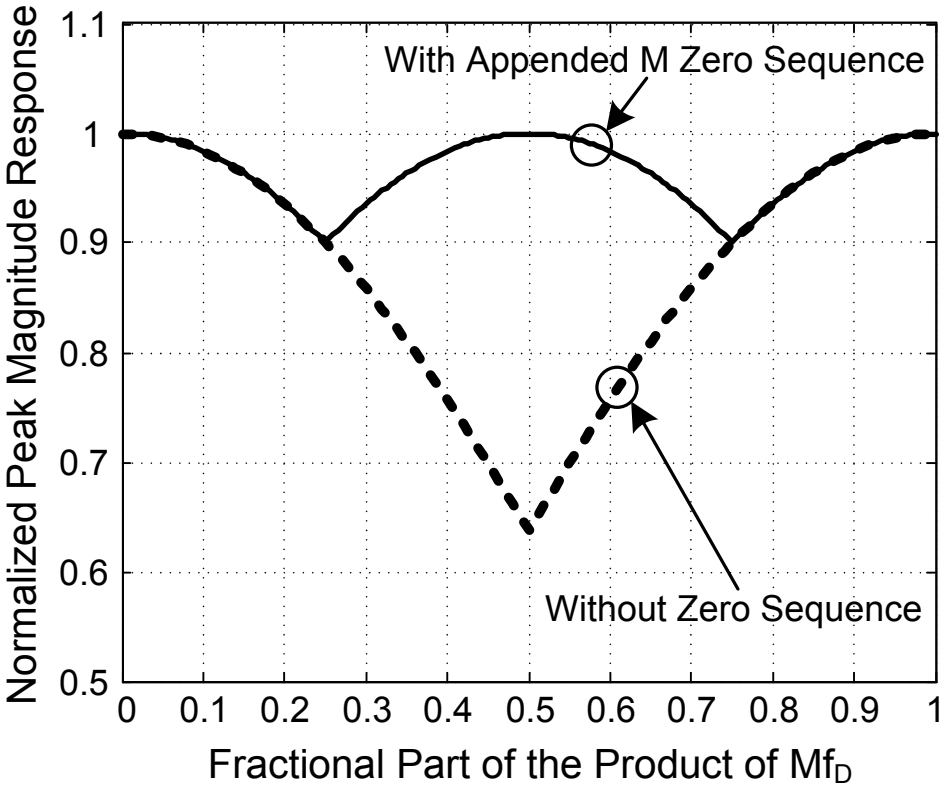

Figure 2.13: Peak magnitude variation with and without the padded zero sequence of length M. The quantities M and f_D represent the number of samples and the discrete-time frequency, respectively.

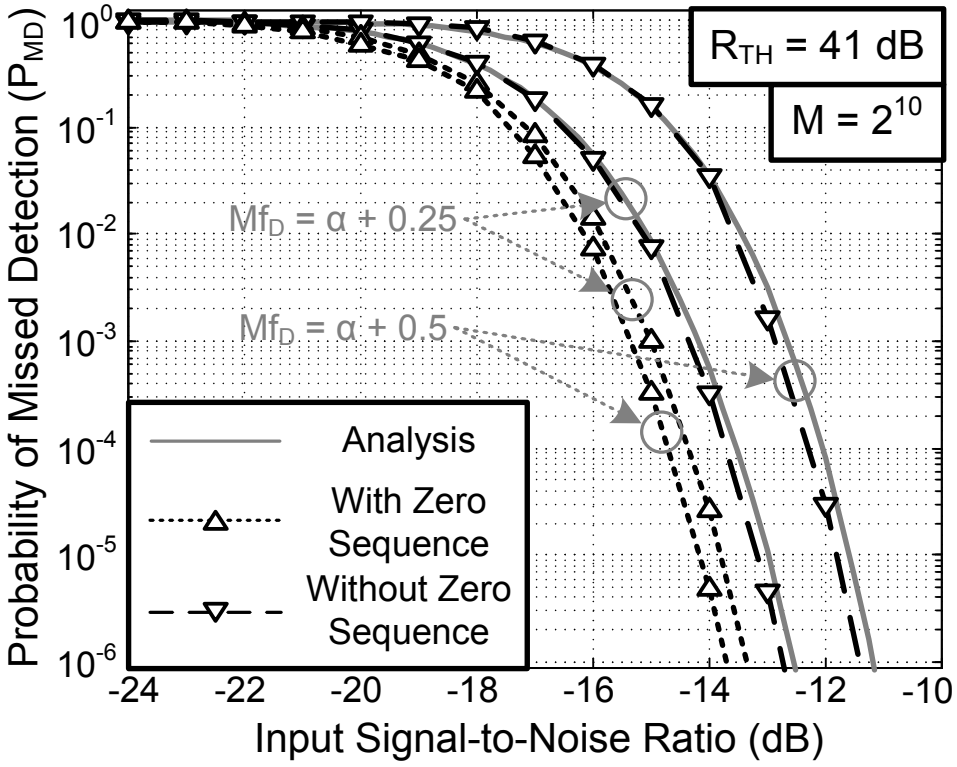

Figure 2.14: Probability of missed detection with and without the padded zero sequence of length M. The quantities α, M, f_D, and R_{TH} denote an arbitrary integer, the number of samples, the discrete-time frequency, and the power ratio between the pre-determined decision threshold and baseband noise, respectively.

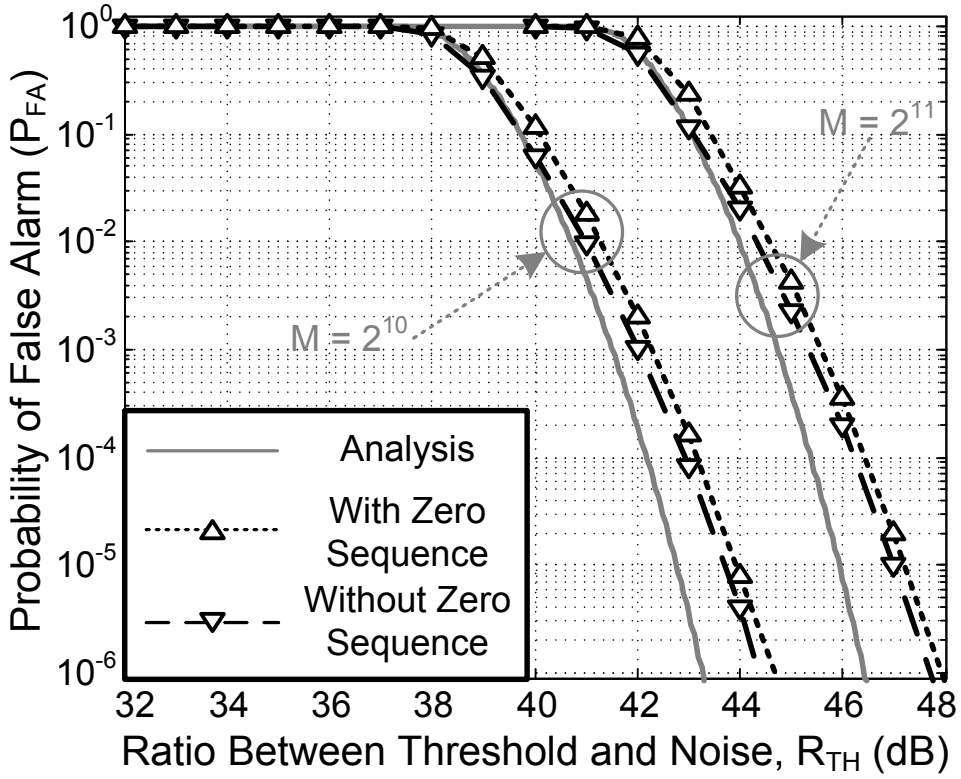

Figure 2.15: Probability of false alarm with and without the appended zero sequence of length M. The quantity M denotes the number of samples

and

$$R_{N_{ZP1}N_{ZP2}}[\tau] = -\sigma_n^2 \sum_{m=1}^{M-1} \sin\left(\frac{\pi}{M} m\tau\right) \tag{2.43}$$

where $\tau \in [0,\ 2M-1]$, respectively. Thus, there are M uncorrelated and M correlated DFT responses among total $2M$-point DFT responses of $N_{ZP}[k]$. In Fig. 2.15, using the 10th order Chebyshev lowpass filter, the P_{FA} simulation results with and without the appended zero sequence of length M are compared. A slight degradation in the P_{FA} simulation results is observed when the zero sequence of length M is appended, and this appears to be due to the additional M frequency bins in (2.41). Therefore, the zero-padding method is effective for reducing the variation in the P_{MD} response, depending on the product of Mf_D at the expense of the slight degradation in P_{FA} response when there is no LO leakage at the input.

2.5 Conclusion

A detection technique has been proposed to identify the presence of nearby unsynchronized WiMAX MT devices within a UWB interference range. The essence of the technique is for the UWB device to sense the incoming LO leakage of an unsynchronized MT that is within the UWB interference range, thus enabling the UWB device to avoid the spectrum of the unsynchronized MT. Both P_{FA} and P_{MD} of the proposed DFT-based UWB detector are derived, and it is shown that there is a tradeoff between P_{FA} and P_{MD} when adjusting the number of samples and the decision threshold. The DFT-based detector is compared with a radiometer, and demonstrated superior performance for the detection of a low-level LO leakage. Cooperation between the WiMAX and UWB systems is recommended to ensure that a UWB device can accurately detect the presence of an unsynchronized WiMAX MT. Lastly, while the detection technique is proposed in the context of UWB, it is also applicable to cognitive radio system, especially for short range data transmission applications.

This chapter has been published and submitted for review in part for the following publications:

1. Sanghoon Park, Lawrence E. Larson, and Laurence B. Milstein, "An RF receiver detection technique for UWB/WiMAX coexistence with applications to cognitive radio," submitted to *IEEE Transactions on Circuits and Systems*, 2009.

2. Sanghoon Park, Lawrence E. Larson, and Laurence B. Milstein, "Hidden mobile terminal device discovery in a UWB environment," in *Proc. IEEE International Conference on Ultra-Wideband*, 2006, pp. 417-421.

Chapter 3

Phase Noise Effects on Signal Detection for UWB/WiMAX Coexistence

3.1 Introduction

The Mobile WiMAX system in the 3 GHz frequency bands is susceptible to potential interference from a UWB device [9]. In order to enhance the coexistence between UWB and WiMAX system, a detection technique utilizing a LO leakage signal coming from a nearby WiMAX MT was presented and analyzed in Chapter 2. However, the power level of the radiated leakage signal is very small. Typically, a leakage signal power level of -90 to -70 dBm is expected at the WiMAX MT receiver antenna port [100, 101], and a path loss of 60 to 80 dB for 10 m distance is expected in an indoor environment [12, 102]. Therefore, the detection sensitivity of the UWB detector is of major concern due to the very weak power of the received LO leakage.

The phase noise of the UWB detector LO can degrade the detection sensitivity when a strong adjacent channel WiMAX signal is present. This phenomenon is known as *reciprocal mixing* [119–123]. In this chapter, we present accurate closed-form expressions for the resulting in-band interference. Section 3.2 analyzes the spectrum broadening due to the receiver LO phase noise for an AWGN environment. The effects of the in-band interference due to the spectrum broadening are estimated for an adjacent channel WiMAX signal in Section 3.3. The conclusions are presented in Section 3.4.

3.2 Spectrum Broadening Due to Local Oscillator Phase Noise Interaction Through a Multiplier

3.2.1 Characteristics of Local Oscillator Phase Noise

For precise frequency as well as phase controls of a LO, a phase-locked loop (PLL) is widely used [115, 116, 120, 124–126]. A PLL is a feedback system which provides a voltage-controlled oscillator (VCO) a correction signal by the amount of the phase deviation it measures. This controlled VCO output signal serves as a LO and is applied to a multiplier.

Figure 3.1 shows the linear time-invariant (LTI) phase-domain model of a PLL under phase-locked condition. Since phase noise of the reference signal is usually very small in a typical operating condition [115, 116, 126], it is assumed that the phase noise of the LO is dominated by that of the VCO. Then, the transfer function for the LO phase noise, denoted by $\phi_{LO}(s)$, is given by

$$\phi_{LO}(s) = \frac{sM_F}{sM_F + K_D K_V F(s)} \phi_{VCO}(s) \tag{3.1}$$

where $\phi_{VCO}(s)$ denotes the phase domain representation for the VCO phase noise. The quantities K_D, K_V, and M_F denote the gain of the phase detector, the frequency gain of the VCO, and the division ratio of the frequency divider, respectively. In case a large division ratio is required to generate a RF carrier ω_{LO} from the low frequency of the reference signal, the effect of the frequency divider on the LO phase noise can be significant. However, an elaborate noise shaping and compensation technique can effectively suppress the noise contribution of the frequency divider [127–130].

From perturbation analysis and stochastic characterization techniques, the phase noise of the VCO can be modeled as the output of an ideal integrator, given by

$$\phi_{VCO}(s) = \frac{n_{VCO}(s)}{s} \tag{3.2}$$

where $n_{VCO}(s)$ denotes the phase domain representation for the VCO noise source, $n_{VCO}(t)$ [131–133]. If $n_{VCO}(t)$ is a zero-mean white Gaussian random process, then $\phi_{VCO}(t)$ is known as a Wiener process [134–136]. The statistical characteristics of the LO phase noise can be different, depending on the loop filters.

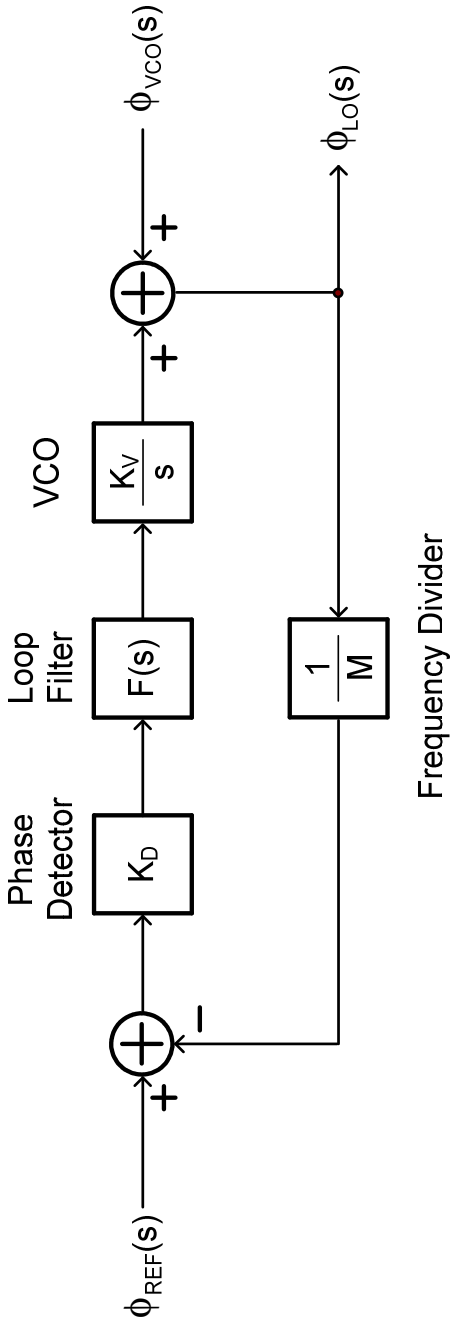

Figure 3.1: The phase domain LTI model of the PLL. The quantity $\phi_{REF}(s)$, $\phi_{VCO}(s)$, and $\phi_{LO}(s)$ represent the phase noise of the reference, VCO, and LO signal in the phase domain, respectively.

First-order Phase-locked Loop

As the simplest PLL, a first-order PLL cab be configured without the loop filter (i.e., $F(s) = 1$) [133,137]. Then, from (3.1), the transfer function of the LO phase noise is given by

$$\phi_{LO}(s) = \frac{s}{s + W_{PLL}} \phi_{VCO}(s) \tag{3.3}$$

where W_{PLL} denotes the PLL bandwidth, and is given by

$$W_{PLL} = \frac{K_D K_V}{M_F}. \tag{3.4}$$

The power spectral density (PSD) of the LO phase noise, from (3.2) and (3.3), using the first-order PLL is given by

$$\begin{aligned} S_{\phi_{LO}}(\omega) &= \left| \frac{1}{s + W_{PLL}} \right|^2_{s=j\omega} S_{\phi_{VCO}}(\omega) \\ &= \frac{1}{\omega^2 + W_{PLL}^2} \left(\frac{\eta_{VCO}}{2} \right) \end{aligned} \tag{3.5}$$

where η_{VCO} denotes the single-sided PSD of $n_{VCO}(t)$. Because of the simple structure of the first-order PLL, it has a critical problem due to the lack of a loop filter. Any spurious signals generated by the phase detector directly modulates the VCO, degrading the LO spectral purity seriously.

Second-order Phase-locked Loop

Probably the most popular PLL architecture is the second-order PLL, which can be obtained with the loop filter transfer function of

$$F(s) = \frac{s + \omega_Z}{s} \tag{3.6}$$

where ω_Z denotes the zero of the loop filter, that should be carefully selected to ensure the enough phase margin of the loop stability [119,120,124,133,137]. Then, from (3.1) and (3.6), the transfer function of the LO phase noise for the second-order PLL is given by

$$\phi_{LO}(s) = \frac{s^2}{s^2 + 2\zeta_{PLL} W_{PLL} s + W_{PLL}^2} \phi_{VCO}(s) \tag{3.7}$$

where the PLL bandwidth W_{PLL} and the PLL damping ratio ζ_{PLL} are given by

$$W_{PLL} = \sqrt{\frac{K_D K_V \omega_Z}{M_F}} \tag{3.8}$$

$$\zeta_{PLL} = \frac{1}{2}\sqrt{\frac{K_D K_V}{M_F \omega_Z}}. \tag{3.9}$$

The PSD of the LO phase noise for the second-order PLL, obtained by combining (3.2) and (3.7), is given by

$$\begin{aligned} S_{\phi_{LO}}(\omega) &= \left| \frac{s^2}{s^2 + 2\zeta_{PLL} W_{PLL} s + W_{PLL}^2} \right|_{s=j\omega}^2 S_{\phi_{VCO}}(\omega) \\ &= \frac{\omega^2}{\omega^4 + \omega^2 \left(4\zeta_{PLL}^2 - 2\right) W_{PLL}^2 + W_{PLL}^4} \left(\frac{\eta_{VCO}}{2}\right). \end{aligned} \tag{3.10}$$

In the feedback system, a damping ratio of less than the critical damping condition of unity results in the ringing problem in its transient response, and that of greater than unity makes the system suffer from a slow settling response. With the PLL damping ratio ζ_{PLL} of unity, $S_{\phi_{LO}}(\omega)$ can be approximated as

$$S_{\phi_{LO}}(\omega) \approx \frac{\omega^2}{\left(\omega^2 + W_{PLL}^2\right)^2} \left(\frac{\eta_{VCO}}{2}\right). \tag{3.11}$$

The PSD of the LO phase noise in (3.11) is now applied to the spectrum broadening of the LO phase noise interaction.

3.2.2 Spectrum Broadening

As a simplified detector architecture, Fig. 3.2 shows a heterodyne receiver, which removes the frequency overlap between the received WiMAX MT LO leakage and detector's own LO leakage. We assume that the total gain of the receive path from the antenna to baseband is unity, all the filters have ideal rectangular frequency responses, and the narrowband intermediate frequency filter sets the bandwidth of the detector.

The phase noise of a typical LO signal, $\phi_{LO}(t)$, generally satisfies $|\phi_{LO}(t)| \ll 1$ (i.e., the standard deviation of $\phi_{LO}(t)$ is much less than one radian). Then, the noisy LO signal can be approximated as

$$\begin{aligned} LO(t) &= 2\cos(\omega_{LO} t + \phi_{LO}(t)) \\ &\approx 2\cos\omega_{LO} t - 2\phi_{LO}(t)\sin\omega_{LO} t \end{aligned} \tag{3.12}$$

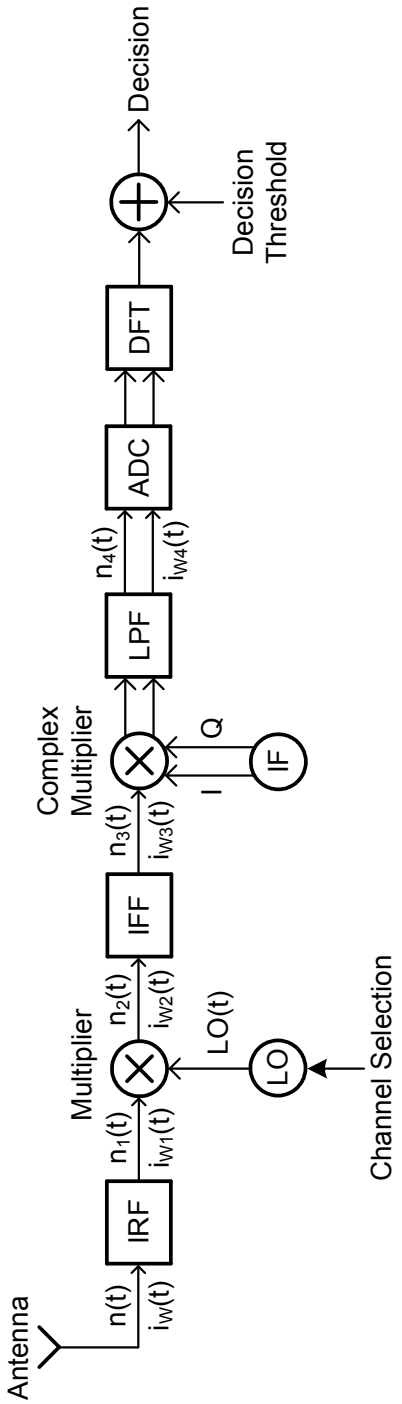

Figure 3.2: Heterodyne receiver architecture. All the gain blocks are excluded. The blocks IRF, IFF, LPF, and ADC denote the image-rejection filter, intermediate-frequency filter, lowpass filter, and analog-to-digital converter, respectively. The signals $n(t)$, $i(t)$, and $LO(t)$ represent the additive white Gaussian noise, adjacent channel interference, and local oscillator signal, respectively.

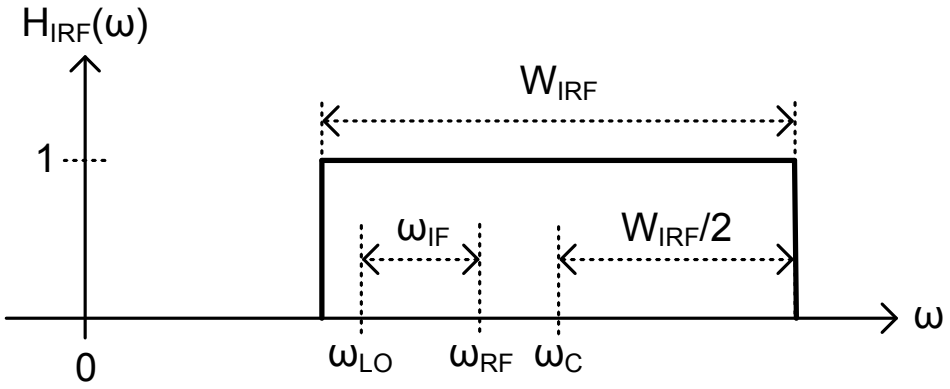

Figure 3.3: Frequency response of the front-end image-rejection filter (IRF). The frequencies ω_{RF}, ω_{IF}, and ω_C denote frequency of the received LO leakage, the intermediate frequency of the receiver, and center frequency of the IRF, respectively. The quantity W_{IRF} denotes the bandwidth of the IRF.

where ω_{LO} denotes the nominal frequency of the LO signal, and ω_{LO} is related to the frequency of the received LO leakage, ω_{RF}, by

$$\omega_{LO} = \omega_{RF} - \omega_{IF} \tag{3.13}$$

where ω_{IF} denotes the intermediate frequency of the receiver. Note that these analyses can also be applied to the direct-conversion receiver by setting $\omega_{IF} = 0$.

The frequency response of the front-end image rejection filter (IRF) is shown in Fig. 3.3. Note that ω_{RF} does not necessarily correspond to the center frequency of the IRF, ω_C. At the output of the IRF, the bandpass noise $n_1(t)$ due to an AWGN input, can be written by

$$n_1(t) = n_C(t)\cos(\omega_{RF}t + \theta_1) - n_S(t)\sin(\omega_{RF}t + \theta_1) \tag{3.14}$$

where $n_C(t)$, $n_S(t)$, and θ_1 denote the inphase component, quadrature component, and arbitrary random phase of $n_1(t)$, respectively [34]. Since the AWGN is a zero-mean white Gaussian random process, $n_C(t)$ and $n_S(t)$ are also zero-mean Gaussian random processes, but their PSDs are given by

$$S_{n_C}(\omega) = S_{n_S}(\omega) = \frac{\eta_0}{2}\left[P_{W_{IRF}}(\omega + \omega_X) + P_{W_{IRF}}(\omega - \omega_X)\right] \tag{3.15}$$

where η_0 and W_{IRF} denotes the single-sided PSD of the AWGN and the bandwidth of the IRF, respectively [34]. The frequency ω_X indicates the frequency difference between ω_{RF} and ω_C. The pulse function P_a is defined by

$$P_a = \begin{cases} 1, & -a/2 \leq x \leq a/2 \\ 0, & \text{otherwise.} \end{cases} \tag{3.16}$$

Due to the asymmetric PSD of $n_1(t)$ around ω_{RF}, $n_C(t)$ and $n_S(t)$ are correlated, and so their cross-PSD is given by [34]

$$S_{n_C n_S}(\omega) = j\frac{\eta_0}{2}\left[P_{W_{IRF}}(\omega - \omega_X) - P_{W_{IRF}}(\omega + \omega_X)\right]. \tag{3.17}$$

Figure 3.4 illustrates the PSD and cross-PSD of $n_C(t)$ and $n_S(t)$.

The bandpass noise $n_1(t)$ is downconverted by a multiplier. Suppose that ω_{LO} is sufficiently large so that the double frequency terms after the multiplier are sufficiently suppressed by the IFF. From (3.12) and (3.14), the downconverted noise at IF, denoted by $n_2(t)$, is given by

$$\begin{aligned} n_2(t) = {} & n_C(t)\cos(\omega_{IF}t + \theta_1) - n_S(t)\sin(\omega_{IF}t + \theta_1) \\ & + \phi_{LO}(t)\left[n_C(t)\sin(\omega_{IF}t + \theta_1) + n_S(t)\cos(\omega_{IF}t + \theta_1)\right]. \end{aligned} \tag{3.18}$$

Then, the complex envelope of $n_2(t)$, denoted by $n_{2E}(t)$, is given by

$$n_{2E}(t) = n_A(t) - jn_B(t) + \phi_{LO}(t)\left[n_B(t) + jn_A(t)\right] \tag{3.19}$$

where

$$n_A(t) = n_C(t)\cos\theta_1 - n_S(t)\sin\theta_1 \tag{3.20}$$

$$n_B(t) = n_C(t)\sin\theta_1 + n_S(t)\cos\theta_1. \tag{3.21}$$

Note that $n_A(t)$ and $n_B(t)$ are also zero-mean Gaussian random processes, and their PSD and cross-PSD are identical to (3.15) and (3.17), respectively. We define the LO phase noise related term in $n_{2E}(t)$ as

$$n_{2\phi}(t) = \phi_{LO}(t)\left[n_B(t) + jn_A(t)\right]. \tag{3.22}$$

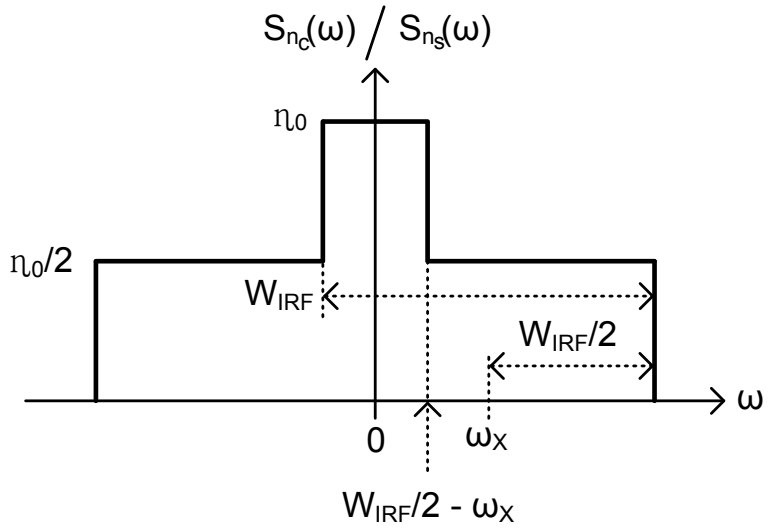

(a)

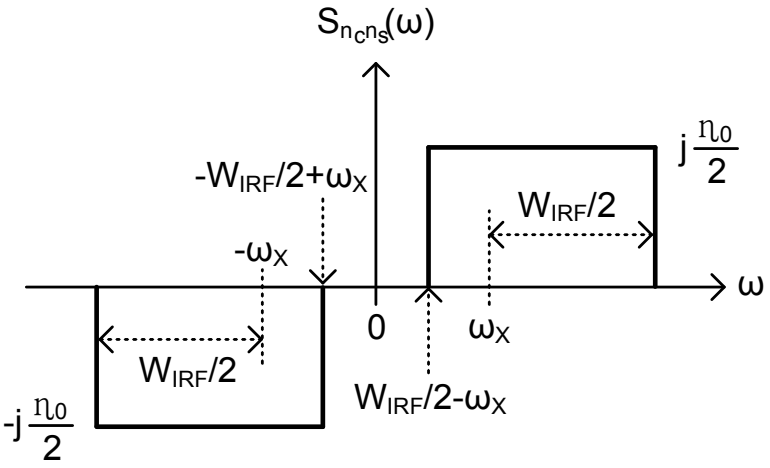

(b)

Figure 3.4: (a) PSD of the inphase and quadrature components of $n_1(t)$. (b) Cross-PSD of inphase and quadrature components of $n_1(t)$

Then, the PSD of $n_{2\phi}(t)$ is given by

$$S_{n_{2\phi}}(\omega) = \frac{1}{\pi} S_{\phi_{LO}}(\omega) * \left[S_{n_A}(\omega) + j S_{n_A n_B}(\omega) \right], \tag{3.23}$$

since $\phi_{LO}(t)$ is independent of $n_A(t)$ and $n_B(t)$ [34, 113].

The spectrum broadening of the phase noise interaction through a multiplier is now analyzed by comparing the equivalent bandwidths of the complex envelopes for the input and output signals of the multiplier. For a complex random process $x(t)$, the equivalent bandwidth W_x can be defined as

$$W_x = \frac{1}{G_x} \int_{-\infty}^{\infty} S_x(\omega) d\omega \tag{3.24}$$

where $S_x(\omega)$ is the PSD of $x(t)$ and $G_x = \max\left[S_x(\omega)\right]$ [34]. At the multiplier input, the complex envelope of $n_1(t)$, denoted by $n_{1E}(t)$, is given by

$$n_{1E}(t) = n_C(t) - j n_S(t). \tag{3.25}$$

Then, from Fig. 3.4, the equivalent bandwidths of $n_{1E}(t)$ is W_{IRF} (i.e., $W_{n_{1E}} = W_{IRF}$).

At the multiplier output, the PSD of $n_{2\phi}(t)$ can be derived by substituting $S_{\phi_{LO}}(\omega)$ in (3.23) by (3.11), and given by

$$S_{n_{2\phi}}(\omega) = \frac{\eta_0 \eta_{VCO}}{4\pi W_{PLL}} \Bigg\{ \tan^{-1}\left(\frac{\omega + W_{IRF}/2 + \omega_X}{W_{PLL}} \right) - \tan^{-1}\left(\frac{\omega - W_{IRF}/2 + \omega_X}{W_{PLL}} \right) - \frac{1}{2} \sin\left[2 \tan^{-1}\left(\frac{\omega + W_{IRF}/2 + \omega_X}{W_{PLL}} \right) \right] + \frac{1}{2} \sin\left[2 \tan^{-1}\left(\frac{\omega - W_{IRF}/2 + \omega_X}{W_{PLL}} \right) \right] \Bigg\} \tag{3.26}$$

Therefore, from the definition of the equivalent bandwidth in (3.24), the equivalent bandwidth of $n_{2\phi}(t)$, denoted by $W_{n_{2\phi}}$, is given by

$$W_{n_{2\phi}} = \frac{\pi W_{IRF}}{\text{Denom.}(W_{IRF}, W_{PLL})} \tag{3.27}$$

where the denominator function, Denom.(W_{IRF}, W_{PLL}), is given by

$$\begin{aligned} \text{Denom.}(W_{IRF}, W_{PLL}) = {} & \tan^{-1}\left(1 + \frac{W_{IRF}}{2W_{PLL}} \right) - \tan^{-1}\left(1 - \frac{W_{IRF}}{2W_{PLL}} \right) \\ & - \frac{1}{2} \sin\left[2 \tan^{-1}\left(1 + \frac{W_{IRF}}{2W_{PLL}} \right) \right] + \frac{1}{2} \sin\left[2 \tan^{-1}\left(1 - \frac{W_{IRF}}{2W_{PLL}} \right) \right] \end{aligned} \tag{3.28}$$

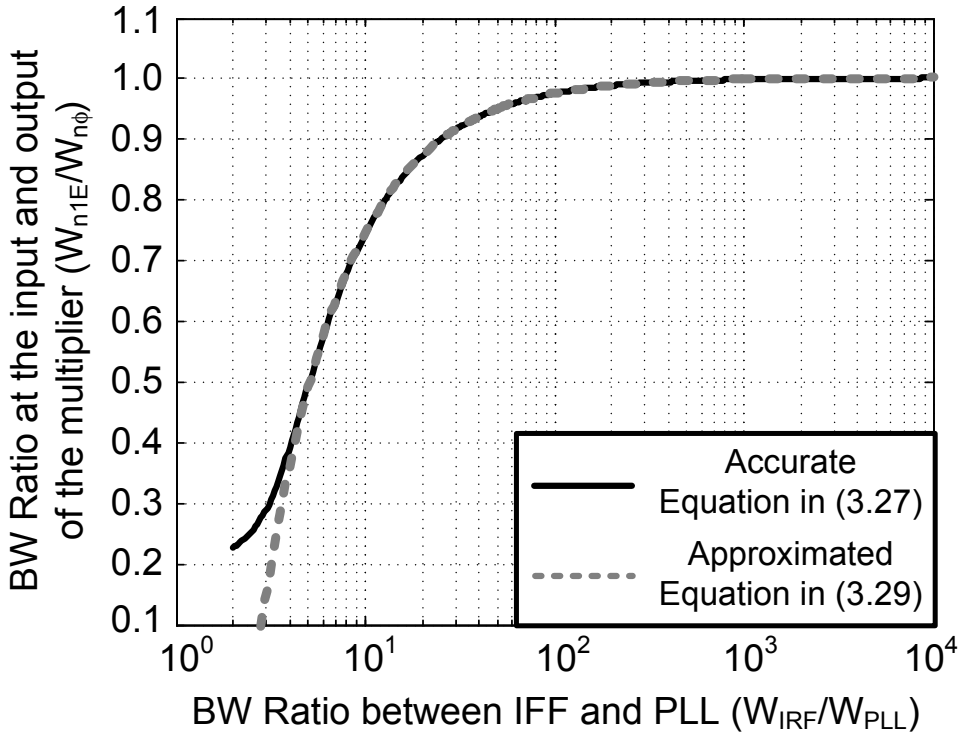

Figure 3.5: Equivalent bandwidth ratio between the complex envelopes of the multiplier input and the phase noise related signal at the multiplier output.

In general, the bandwidth of the front-end image rejection filter is large enough to cover the whole system band (i.e., $W_{IRF} \gg W_{PLL}$). Then, (3.27) reduces to

$$W_{n_{2\phi}} \approx \frac{\pi W_{IRF}^2}{\pi W_{IRF} - 8W_{PLL}} \tag{3.29}$$

using the approximation of $\tan^{-1}(x) \approx \pi/2 - 1/x$ for the large positive number of x [114]. The ratio of the equivalent bandwidths between $n_{1E}(t)$ and $n_{2\phi}(t)$ as a function of the ratio between W_{IRF} and W_{PLL} is shown in Fig. 3.5. Due to the convolution effect of the LO phase noise interaction, the equivalent bandwidth of $n_{2\phi}(t)$ is broadened, so that the energy of the multiplier input signal spills over in other signal bands at the multiplier output. The spectrum broadening due to the phase noise interaction through the multiplier can be significant when a strong adjacent channel signal is present at the multiplier input.

3.3 Local Oscillator Phase Noise Interaction with Adjacent Channel WiMAX Signal

3.3.1 In-band Interference Due to Adjacent Channel WiMAX Signal

The spectrum broadening effect can convert an adjacent channel signal into in-band interference. Suppose that the UWB detector is searching a particular channel of the WiMAX system, while an adjacent channel is concurrently occupied. Then, the received adjacent channel WiMAX signal can be represented by

$$i_W(t) = i_C(t)\cos([\omega_{RF} + W_W]t + \theta_W) - i_S(t)\sin([\omega_{RF} + W_W]t + \theta_W) \tag{3.30}$$

where θ_W and W_W denote an arbitrary random phase and the channel bandwidth of the WiMAX system. As an OFDM signal, the inphase and quadrature phase components of $i_C(t)$ and $i_S(t)$, respectively, can be modeled as independent, identically distributed, wide-sense stationary (WSS) Gaussian processes [49, 138]. Since the OFDM signal consists of a large number of subcarriers whose spectral width is narrow, the PSD of $i_W(t)$ can be approximated as having a rectangular shape [49, 138, 139]. Therefore, the PSD of both $i_C(t)$ and $i_S(t)$ are approximated as

$$S_{i_C}(\omega) = S_{i_S}(\omega) = \eta_W P_{W_W}(\omega) \tag{3.31}$$

where η_W denotes the single-sided PSD of $i_W(t)$. In general, the front-end IRF cannot sufficiently attenuate this adjacent channel signal, and so it will interact with the LO phase noise through the multiplier, and the resulting phase noise related signal whose bandwidth is broadened leaks to the channel the UWB detector is listening to.

Suppose that the IFF with the impulse response $h_{IFF}(t)$ is a narrowband channel selection filter. Then, the IFF output signal due to $i_W(t)$, denoted by $i_{W3}(t)$, is given by

$$i_{W3}(t) = i_{W\phi}(t) * h_{IFF}(t) \tag{3.32}$$

where

$$\begin{aligned} i_{W\phi}(t) = {} & \phi_{LO}(t) i_C(t)\sin([\omega_{IF} + W_W]t + \theta_W) \\ & + \phi_{LO}(t) i_S(t)\cos([\omega_{IF} + W_W]t + \theta_W). \end{aligned} \tag{3.33}$$

The double frequency terms and downconverted adjacent channel signals after the multiplier are assumed to be filtered out by the narrowband IFF. From (3.33), the complex envelope of $i_{W\phi}(t)$, denoted by $i_{W\phi E}(t)$, is given by

$$i_{W\phi E}(t) = \phi_{LO}(t) i_A(t) + j\phi(t) i_B(t) \tag{3.34}$$

where

$$i_A(t) = \; i_C(t)\sin\theta_W + i_S(t)\cos\theta_W \tag{3.35}$$

$$i_B(t) = \; i_C(t)\cos\theta_W - i_S(t)\sin\theta_W. \tag{3.36}$$

Note that $i_A(t)$ and $i_B(t)$ are independent zero-mean Gaussian processes and have the same statistics as $i_C(t)$ or $i_S(t)$. With the complex envelope $i_{W\phi E}(t)$, $i_{W3}(t)$ in (3.32) can be rewritten by

$$i_{W3}(t) = \Re[\exp(-j\omega_{IF}t)\{[i_{W\phi E}(t)\exp(-jW_W t)] * h_{LPE}(t)\}] \tag{3.37}$$

where $h_{LPE}(t)$ denotes the impulse response of the lowpass equivalent of $h_{IFF}(t)$. The lowpass equivalent transfer function is given by

$$H_{LPE}(\omega) = \begin{cases} H_{IFF}(\omega - \omega_{IF}), & |\omega| \le \omega_{IF} \\ 0, & \text{otherwise} \end{cases} \tag{3.38}$$

where $H_{IFF}(\omega)$ denotes the Fourier transform pair of $h_{IFF}(t)$.

As shown in Fig. 3.2, $i_{W3}(t)$ is multiplied by inphase and quadrature signals of the IF LO signal. Since the narrowband channel selection IFF attenuates all the out-of-channel signals and the phase noise of a typically IF LO signal satisfies $|\phi_{LO}(t)| \ll 1$, the phase noises of the IF LO signals can be neglected. Then, the complex baseband in-band interference, $i_{W4}(t)$, is given by

$$i_{W4}(t) = [i_{W\phi E}(t)\exp(-j\omega_W t)] * h_{LPE}(t). \tag{3.39}$$

This in-band interference results from the interaction between the LO phase noise and the adjacent channel WiMAX signal, and its spectrum overlaps the desired channel spectrum band by increasing the signal-to-noise-and-interference ratio (SNIR).

In order to quantify the in-band interference $i_{W4}(t)$, it is convenient to compare the power of $i_{W4}(t)$ with that of the baseband noise which results from the AWGN input and a noiseless LO signal. For instance, if the ratio of the power of $i_{W4}(t)$ to that of the baseband noise is unity, the SNIR degrades by 3 dB due to the presence of the LO phase noise. The baseband noise $n_4(t)$ can be derived from (3.19). By ignoring the phase noise $\phi_{LO}(t)$, the baseband complex noise $n_4(t)$ is given by

$$n_4(t) = n_I(t) - jn_Q(t) \tag{3.40}$$

where $n_I(t)$ and $n_Q(t)$ are independent zero-mean Gaussian random processes. With the ideal brick-wall frequency response of the IFF with bandwidth W_{IFF}, the power of $n_4(t)$, denoted by $\sigma^2_{n_4}$, is given by

$$\sigma^2_{n_4} = \sigma^2_{n_I} + \sigma^2_{n_Q} = \frac{\eta_0 W_{IFF}}{\pi}. \tag{3.41}$$

The power of in-band interference $i_{W4}(t)$ can be derived from (3.39). Substituting $i_{W\phi E}(t)$ in (3.39) by (3.34), the PSD of $i_{W4}(t)$ is given by

$$S_{W4}(\omega) = \frac{1}{\pi}\left[S_{\phi_{LO}}(\omega) * S_{i_{WA}}(\omega) * \delta(\omega + W_W)\right] |H_{LPE}(\omega)|^2 \tag{3.42}$$

since $\phi_{LO}(t)$, $i_{WA}(t)$, and $i_{WB}(t)$ are all independent. Substituting $S_{\phi_{LO}}(\omega)$ by (3.11), $S_{W4}(\omega)$ is given by

$$\begin{aligned} S_{W4}(\omega) = \frac{\eta_W \eta_{VCO}}{4\pi W_{PLL}} \Bigg\{ & \tan^{-1}\left(\frac{\omega + 3W_W/2}{W_{PLL}}\right) - \tan^{-1}\left(\frac{\omega + W_W/2}{W_{PLL}}\right) \\ & - \frac{1}{2}\sin\left[2\tan^{-1}\left(\frac{\omega + 3W_W/2}{W_{PLL}}\right)\right] \\ & + \frac{1}{2}\sin\left[2\tan^{-1}\left(\frac{\omega + W_W/2}{W_{PLL}}\right)\right] \Bigg\} |H_{LPE}(\omega)|^2 . \end{aligned} \tag{3.43}$$

Then, with the ideal brick-wall frequency response of the IFF with the bandwidth W_{IFF},

the power of the in-band interference $i_{W4}(t)$, denoted by σ_{W4}^2, is given by

$$\begin{aligned}\sigma_{W4}^2 = \frac{P_W \eta_{VCO}}{8\pi W_{PLL} W_W} \Bigg\{ & (3W_W + W_{IFF}) \tan^{-1}\left(\frac{3W_W + W_{IFF}}{2W_{PLL}}\right) \\ & - (3W_W - W_{IFF}) \tan^{-1}\left(\frac{3W_W - W_{IFF}}{2W_{PLL}}\right) \\ & - (W_W + W_{IFF}) \tan^{-1}\left(\frac{W_W + W_{IFF}}{2W_{PLL}}\right) \\ & + (W_W - W_{IFF}) \tan^{-1}\left(\frac{W_W - W_{IFF}}{2W_{PLL}}\right) \\ & + 2W_{PLL} \ln\left(\frac{[(3W_W - W_{IFF})^2 + 4W_{PLL}^2][(W_W + W_{IFF})^2 + 4W_{PLL}^2]}{[(3W_W + W_{IFF})^2 + 4W_{PLL}^2][(W_W - W_{IFF})^2 + 4W_{PLL}^2]}\right) \Bigg\}\end{aligned} \tag{3.44}$$

where P_W denotes the power of the received adjacent channel signal $i_W(t)$ in (3.30) (i.e., $P_W = \eta_W W_W / 2\pi$). As the power of either phase noise or adjacent channel signal increases, the power of in-band interference becomes comparable to that of the baseband noise.

The PSD of the LO phase noise is often described by the relative power ratio around the fundamental oscillation frequency f_{LO}. This relative power ratio, denoted by $\mathfrak{L}(f)$, is generally defined as [17, 120, 133]

$$\mathfrak{L}(f) = \frac{S_{LO}(f_{LO} + f)}{P_{LO}} = S_{\phi_{LO}}(f) \tag{3.45}$$

where $S_{LO}(f)$ and P_{LO} denote the single-sided PSD and power of the LO, respectively. For a frequency offset f that is greater than the PLL bandwidth, $\mathfrak{L}(f)$ can be, from (3.11), approximated as

$$\mathfrak{L}(f) \approx \frac{1}{f^2}\left(\frac{\eta_{VCO}}{8\pi^2}\right). \tag{3.46}$$

Using the relative phase noise PSD $\mathfrak{L}(f)$, the power ratio of in-band interference

$i_{W4}(t)$ in (3.39) to the baseband noise $n_4(t)$ in (3.40) are given by

$$\begin{aligned}\rho_W &= \frac{\sigma_{W4}^2}{\sigma_{n4}^2} \\ &= \frac{\pi^2 P_W f^2 \mathfrak{L}(f)}{\eta_0 W_{IFF} W_{PLL} W_W} \Bigg\{ (3W_W + W_{IFF}) \tan^{-1}\left(\frac{3W_W + W_{IFF}}{2W_{PLL}}\right) \\ &\quad - (3W_W - W_{IFF}) \tan^{-1}\left(\frac{3W_W - W_{IFF}}{2W_{PLL}}\right) \\ &\quad - (W_W + W_{IFF}) \tan^{-1}\left(\frac{W_W + W_{IFF}}{2W_{PLL}}\right) \\ &\quad + (W_W - W_{IFF}) \tan^{-1}\left(\frac{W_W - W_{IFF}}{2W_{PLL}}\right) \\ &\quad + 2W_{PLL} \ln\left(\frac{[(3W_W - W_{IFF})^2 + 4W_{PLL}^2][(W_W + W_{IFF})^2 + 4W_{PLL}^2]}{[(3W_W + W_{IFF})^2 + 4W_{PLL}^2][(W_W - W_{IFF})^2 + 4W_{PLL}^2]}\right) \Bigg\}\end{aligned} \tag{3.47}$$

Figure 3.6 illustrates the variation of ρ_W as a function of the LO phase noise. As expected, the LO phase noise should be sufficiently suppressed, in order not to generate serious in-band interference. This in-band interference is now applied to the coexistence problem between the UWB and WiMAX systems.

3.3.2 Detection Performance Variation Due to LO Phase Noise Interaction with Adjacent Channel WiMAX Signal

The presence of the adjacent channel signal will modify the detection performance when a UWB device scans a nearby WiMAX MT [140, 141]. Since $i_{W4}(t)$, as given in (3.39), results from the multiplication of two Gaussian processes, its statistics are not Gaussian. Therefore, due to the difficulty in analyzing the detection performance when actual WiMAX waveform is used as the adjacent channel signal, we resorted to simulations to generate numerical results. However, as a check on the accuracy of the simulation, we both analyzed and simulated the detection performance with a single frequency jammer instead of the adjacent channel WiMAX signal. The simulation results of the detection performance with the adjacent channel WiMAX signal will be compared with those with the signal frequency jammer. The analysis of the in-band interference

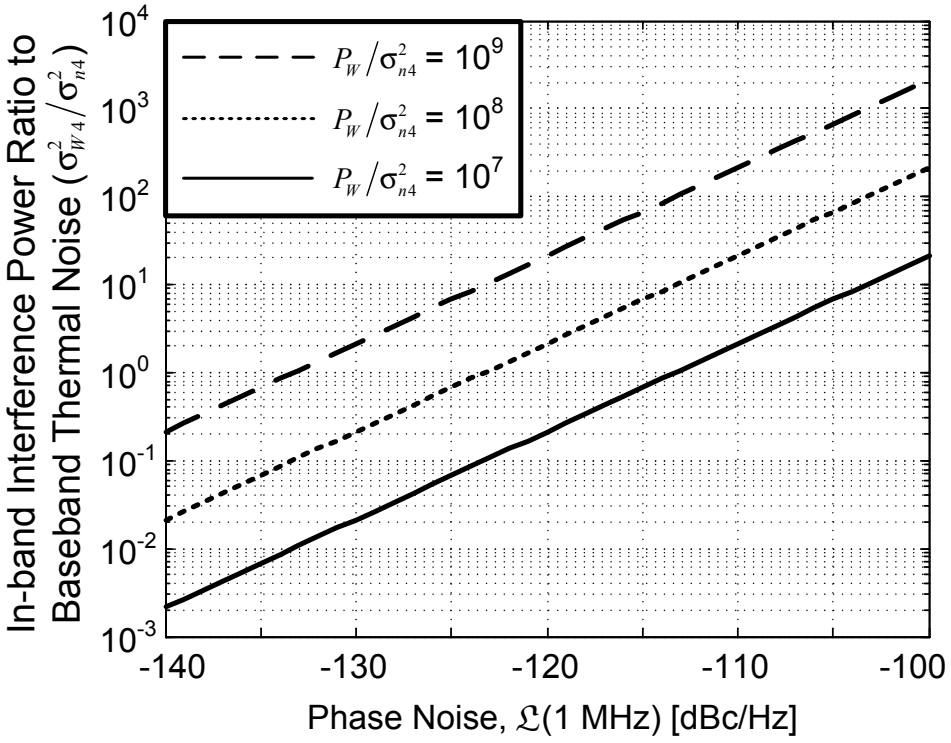

Figure 3.6: Power ratio of the in-band interference due to the interaction between the LO phase noise and the adjacent channel WiMAX signal to the baseband noise due to the AWGN without LO phase noise. The quantities P_W and σ_{n4}^2 denote the powers of the adjacent channel WiMAX signal and baseband noise, respectively: f_{PLL} = 100 kHz, f_{IFF} = 100 kHz, and f_W = 5 MHz.

due to the single frequency jammer is now presented.

In-band Interference Due to Single Frequency Jammer

A single frequency tone jammer can be represented by

$$i_J(t) = A_J \cos([\omega_{RF} + W_J]t + \theta_J) \tag{3.48}$$

where A_J and θ_J denote the amplitude and an arbitrary phase of the received single frequency jammer. The frequency difference between $i_J(t)$ and the desired LO leakage is denoted by W_J. Similarly, the complex baseband in-band interference, denoted by $i_{J4}(t)$, due to the single frequency jammer $i_J(t)$ is given by

$$i_{J4}(t) = [i_{J\phi E}(t) \exp(-jW_J t)] * h_{LPE}(t) \tag{3.49}$$

where the complex envelope $i_{J\phi E}(t)$ is given by

$$i_{J\phi E}(t) = A_J \sin\theta_J \phi_{LO}(t) + jA_J \cos\theta_J \phi_{LO}(t). \tag{3.50}$$

Then, the PSD of $i_{J4}(t)$ is given by

$$S_{J4}(\omega) = \left[A_J^2 S_{\phi_{LO}}(\omega + W_J)\right] |H_{LPE}(\omega)|^2 . \tag{3.51}$$

The LO phase noise effectively determines the statistical properties of $i_{J4}(t)$, but its power also varies with the received single frequency jammer $i_J(t)$. Substituting $S_{\phi_{LO}}(\omega)$ in (3.50) by (3.11), $S_{J4}(\omega)$ is given by

$$S_{J4}(\omega) = \frac{A_J^2(\omega + W_J)^2}{\left[(\omega + W_J)^2 + W_{PLL}^2\right]^2} \left(\frac{\eta_{VCO}}{2}\right) |H_{LPE}(\omega)|^2 \tag{3.52}$$

and the power of the in-band interference $i_{J4}(t)$ is given by

$$\begin{aligned}\sigma_{J4}^2 =& \frac{P_J \eta_{VCO}}{4\pi W_{PLL}} \Bigg\{ \tan^{-1}\left(\frac{W_J + W_{IFF}/2}{W_{PLL}}\right) - \tan^{-1}\left(\frac{W_J - W_{IFF}/2}{W_{PLL}}\right) \\ & - \frac{1}{2}\sin\left[2\tan^{-1}\left(\frac{W_J + W_{IFF}/2}{W_{PLL}}\right)\right] + \frac{1}{2}\sin\left[2\tan^{-1}\left(\frac{W_J - W_{IFF}/2}{W_{PLL}}\right)\right] \Bigg\}\end{aligned} \tag{3.53}$$

where P_J denotes the power of the received single tone jammer (i.e., $P_J = A_J^2/2$). If W_J is much greater than both W_{IFF} and W_{PLL}, then (3.53) reduces to

$$\sigma_{J4}^2 \approx \frac{P_J \eta_{VCO} W_{IFF}}{2\pi W_J^2}. \tag{3.54}$$

As expected, the power of in-band interference due to a single frequency jammer is inversely proportional to ω_J^2 [142, 143]. Moreover, the in-band interference due to the phase noise interaction becomes almost independent of the PLL parameters.

Using the relative phase noise PSD $\mathfrak{L}(f)$, the power ratio of in-band interference $i_{J4}(t)$ in (3.49) to the baseband noise $n_4(t)$ in (3.40) are given by

$$\rho_J = \frac{\sigma_{J4}^2}{\sigma_{n4}^2} = \frac{4\pi^2 P_J f^2 \mathfrak{L}(f)}{\eta_0 W_J^2}. \tag{3.55}$$

The in-band interference $i_{J4}(t)$ is now applied to the coexistence problem between the UWB and WiMAX systems.

Detection Performance Variation Due to LO Phase Noise Interaction with Single Frequency Jammer

In the context of detecting an unsynchronized WiMAX MT, the received signal of a UWB detector with LO phase noise and a single frequency jammer can be described by one of the following two hypotheses:

$$H_0 : \ r(t) = n_W(t) + i_J(t) \tag{3.56a}$$

or

$$H_1 : \ r(t) = s_{RF}(t) + n_W(t) + i_J(t) \tag{3.56b}$$

where $s_{RF}(t)$ and $n_W(t)$ denote the received LO leakage from a nearby WiMAX MT and an AWGN, respectively. The UWB detector downconverts $r(t)$ to baseband, and performs a discrete Fourier transform (DFT), as shown in Fig. 3.2. The UWB device decides that $s_{RF}(t)$ is absent if the magnitude response of all the DFT frequency bins fall below a pre-determined decision threshold. If at least one of the DFT outputs exceeds the threshold, the receiver decides that $s_{RF}(t)$ is present.

Under hypothesis H_0, the downconverted baseband signal, denoted by $r_D(t)$, is approximately equal to sum of the baseband noise and the in-band interference, given by

$$r_D(t) \approx n_4(t) + i_{J4}(t). \tag{3.57}$$

Since the phase noise of a typical LO signal satisfies $|\phi_{LO}(t)| \ll 1$ (i.e., the standard deviation of $\phi_{LO}(t)$ is much less than one radian), the phase noise interaction with the AWGN can be negligible when compared with either $n_4(t)$ or $i_{J4}(t)$. Note that $n_4(t)$ and $i_{J4}(t)$ are independent. If the main noise source of the VCO is a zero-mean WSS white Gaussian process, then $j_{J4}(t)$ is also a zero-mean WSS Gaussian process because the in-band interference $i_{J4}(t)$ results from the LTI processes in (3.49). With the the M samples of $r_D(t)$ from the Nyquist-rate sampling, the probability of false alarm in (2.8) is modified to

$$P_{FA} = 1 - \left(1 - \exp\left(-\frac{D_{TH}^2}{M\sigma_{n4}^2[1+\rho_J]}\right)\right)^M. \tag{3.58}$$

Due to the in-band interference $i_{J4}(t)$, the M-point DFT responses experience increased variance, and so are more likely to exceed the pre-determined decision threshold D_{TH}. Figure 3.7 shows the P_{FA} degradation due to the in-band interference for the adjacent channel signals of $i_W(t)$ and $i_J(t)$ separately. The lowpass equivalent of the IFF is implemented by a 10th-order Chebyshev lowpass filter with 100 kHz bandwidth and 0.5 dB passband ripple in Fig. 3.7 [87].

Under hypothesis H_1, the received LO leakage $s_{RF}(t)$ is an unmodulated sinusoidal wave, given by

$$s_{RF}(t) = A_{RF}\cos(\omega_{RF}t + \theta_{RF}) \tag{3.59}$$

where A_{RF} and θ_{RF} denote the amplitude and arbitrary random phase of the received LO leakage. Then, the downconverted LO leakage, denoted by $s_D(t)$, is given by

$$s_D(t) = A_{RF}\exp\left(j[\omega_{RF} - \omega_{LO} - \omega_{IF}]t + \theta_D\right) \tag{3.60}$$

where the uniformly distributed random phase θ_D accounts for an arbitrary phase mismatch between the received LO leakage and the UWB detector's LO signals.

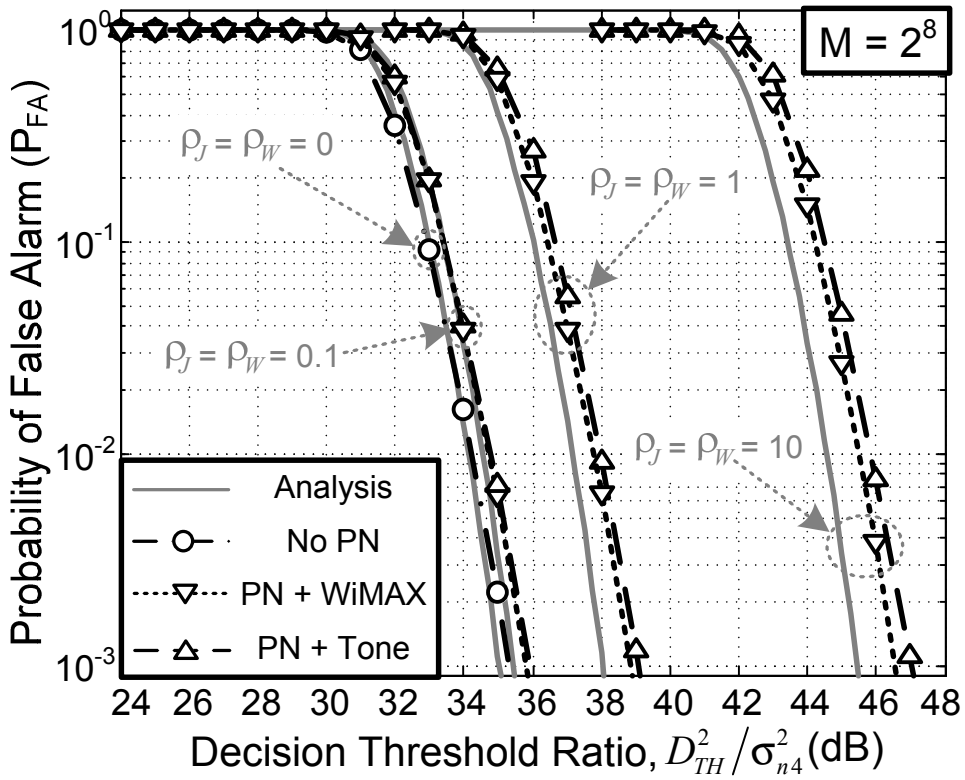

Figure 3.7: The P_{FA} degradation with the in-band interference for the adjacent channel signals of $i_W(t)$ and $i_J(t)$ separately. The quantities D_{TH}, σ^2_{n4}, M, and PN denote the pre-determined decision threshold, the baseband noise power, the number of samples, and LO phase noise, respectively.

Due to the phase noise interaction with the strong $i_J(t)$, the downconverted baseband signal $r_D(t)$ is approximately given by

$$r_D(t) \approx s_D(t) + n_4(t) + i_{J4}(t) \tag{3.61}$$

where the phase noise interaction with the AWGN is ignored because of $|\phi_{LO}(t)| \ll 1$, when compared with either $n_4(t)$ or $i_{J4}(t)$. Similarly, the phase noise interaction with $s_{RF}(t)$ is also negligible in the negative SNR range we are interested in, when compared with $s_D(t)$. Then, with the M samples of $r_D(t)$ from the Nyquist-rate sampling, the probability of false alarm in (2.11) is modified to

$$\begin{aligned} P_{MD} = &\left[1 - Q\left(\sqrt{\frac{2M\lambda}{1+\rho_J}}, \sqrt{\frac{2D_{TH}^2}{M\sigma_{n4}^2[1+\rho_J]}}\right)\right] \\ &\times \left[1 - \exp\left(-\frac{D_{TH}^2}{M\sigma_{n4}^2[1+\rho_J]}\right)\right]^{M-1}. \end{aligned} \tag{3.62}$$

Figure 3.8 shows the P_{MD} variation due to the in-band interference for the adjacent channel signals of $i_W(t)$ and $i_J(t)$ separately, using the same filter as used in Fig. 3.7. It is noted that the P_{MD} responses with and without the in-band interference exhibit a crossover. At sufficiently high input SNR, the DFT response in the absence of the in-band interference will, with high probability, exceed the pre-determined decision threshold. Thus, in presence of in-band interference at sufficiently high input SNR, the DFT response with the increased variation will less likely exceed the threshold, so that P_{MD} increases with in-band interference. On the other hand, at sufficiently low input SNR, the DFT response in the absence of in-band interference will often fall below the pre-determined decision threshold, and so the presence of in-band interference is actually beneficial for correct detection due to the increased variation in the DFT response. Therefore, P_{MD} decreases with in-band interference at sufficiently low input SNR.

In Fig. 3.7 and Fig. 3.8, the simulation results of P_{FA} and P_{MD} with in-band interference show good agreement with the analytical results of (3.58) and (3.62) when the power of the in-band interferences is much weaker than that of the baseband noise $n_4(t)$. As the power of the in-band interference increases, the deviation of the simulation results from the analytical results increases. There are mainly three reasons for this deviation:

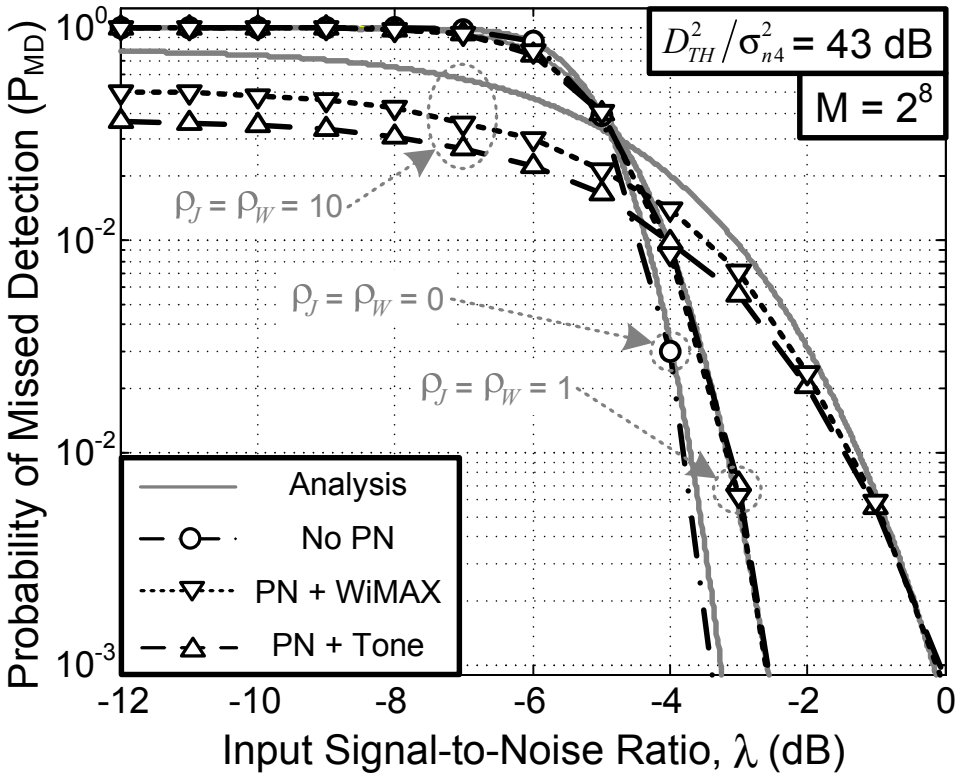

Figure 3.8: The P_{MD} variation with the in-band interference for the adjacent channel signals of $i_W(t)$ and $i_J(t)$ separately. The quantities D_{TH}, σ_{n4}^2, M, and PN denote the pre-determined decision threshold, the baseband noise power, the number of samples, and LO phase noise, respectively.

- Use of the 10th-order Chebyshev lowpass filter instead of the ideal rectangular filter used in the P_{FA} and P_{MD} analyses
- Aliasing problem when sampling LO phase noise which inherently has an infinite bandwidth
- Flat PSD approximation for the in-band interference

The in-band interference always degrades the P_{FA} response, as shown in (3.58). In order to compensate for this P_{FA} degradation, the decision threshold in (3.58) should be adjusted as follows:

$$D_{TH} = \sqrt{-M\sigma_{n4}^2[1+\rho_J]\ln\left[1-\left(1-P_{FA(des)}\right)^{\frac{1}{M}}\right]} \tag{3.63}$$

where $P_{FA(des)}$ denotes the desired P_{FA}. The modified decision threshold in (3.63) assures that P_{FA} is always less than the desired P_{FA}, regardless of the presence of in-band interference. However, this remedy increases P_{MD}. Substituting D_{TH} in (3.62) by (3.63), the P_{MD} response with the modified decision threshold is given by

$$\begin{aligned} P_{MD} = &\left[1 - Q\left(\sqrt{\frac{2M\lambda}{1+\rho_J}}, \sqrt{-2\ln\left[1-\left(1-P_{FA(des)}\right)^{\frac{1}{M}}\right]}\right)\right] \\ &\times \left[1-P_{FA(des)}\right]^{\frac{M-1}{M}} \end{aligned} \tag{3.64}$$

As a result, the number of samples M should be increased, in order to compensate for the degradation in P_{MD} due to the modified decision threshold. The required M is shown in Fig. 3.9 to simultaneously satisfy both the desired P_{FA} and the desired P_{MD} with different values of ρ_J.

3.4 Conclusion

The spectrum broadening due to the phase noise interaction through a multiplier has been analyzed. Due to the spectrum broadening, the presence of the LO phase noise causes the energy of a strong adjacent channel signal to spill over and become in-band interference in adjacent channels.

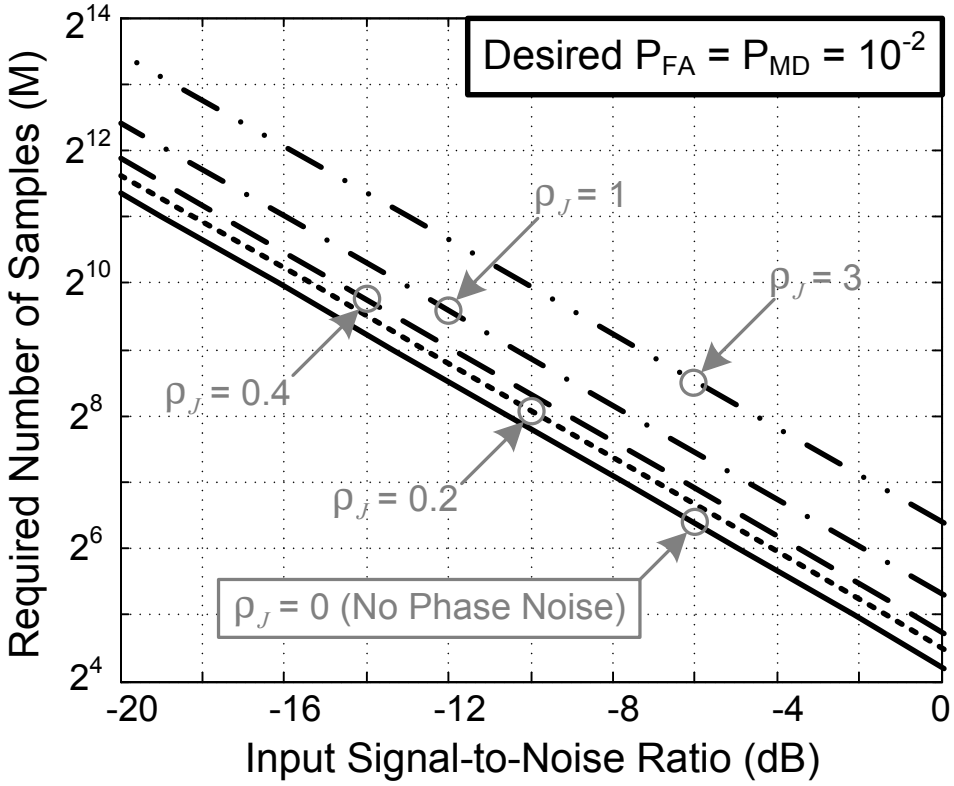

Figure 3.9: Required number of samples with the in-band interference due to the frequency tone jammer.

The results for in-band interference can be useful when evaluating the phase noise requirement of a receiver. For example, in order to ensure that a -30 dBm power level from an adjacent channel WiMAX signal does not result in more than 1 dB SNIR degradation, the UWB detector requires an LO signal whose relative phase noise PSD, $\mathfrak{L}(f)$, is less than -134 dBc/Hz at 1 MHz frequency offset, assuming 5 dB receiver noise figure, 100 kHz PLL bandwidth, 200 kHz IFF bandwidth, and 5 MHz WiMAX channel.

The in-band interference degrades the detector performance. Since the bandwidth of the front-end RF filter should be large enough to cover the whole system band, the LO phase noise interaction with an adjacent channel signal through a multiplier is inevitable. Therefore, the local oscillator has to be designed so that the phase noise has been sufficiently suppressed.

This chapter has been published and submitted for review in part for the following publications:

1. Sanghoon Park, Lawrence E. Larson, and Laurence B. Milstein, "Spectrum broadening of phase noise interaction with applications to cognitive radio coexistence," submitted to *IEEE Communications Letters*, 2009.

2. Sanghoon Park, Lawrence E. Larson, and Laurence B. Milstein, "Phase noise effects on signal detection for UWB/WiMAX coexistence," in *Proc. International Conference on Military Communication*, 2008, pp. 1-7.

Chapter 4

Interference Suppression Tunable RF Filter for IEEE 802.22 Cognitive Radio Applications

4.1 Introduction

Cognitive radio (CR) was proposed to manage the frequency allocation problems due to spectrum crowding [14, 15, 19], and the IEEE 802.22 working group has been developing a world-wide CR-based standard for WRANs in frequency bands currently allocated to the TV broadcast service [60]. Recently, the FCC released its order allowing personal portable devices to operate on unoccupied TV channels between 21 and 51 — except 37 — for IEEE 802.22 applications [31]. These frequency bands may be extended to 41 $\sim$ 910 MHz to meet international regulations [13]. In addition, the standard bandwidth of international TV channels varies from 6 to 8 MHz [13].

Since a CR device applicable to IEEE 802.22 applications must coexist with commercial TV systems, the presence of a strong adjacent TV signal is one of the challenging characteristics of the IEEE 802.22 CR system. A signal transmitted by a nearby TV station can be so strong that a level of -8 dBm is suggested in terms of the receiver blocking level [66]. However, the minimum detectable level of a desired CR signal can be as weak as -102 dBm [66]. Thus, the required dynamic range, more than 90 dB, of

the receiver puts a heavy burden on the receiver design to process a weak desired signal simultaneously with a strong TV signal. Therefore, an interference suppression filtering technique is highly desired to suppress the strong TV signals. At the same time, this technique must have very low loss and distortion. Finally, the filter must be tunable over a wide frequency range, because the channel allocation of the TV signal will depend on the geographic location of the CR device, and is outside of the control of the CR network.

Surface acoustic wave (SAW), microelectromechanical systems (MEMS), or distributed element filters can provide high suppression for a strong TV signal [71, 72, 78, 83, 85, 144], but they have well-known size and cost issues. An active circuit technique to synthesize an interference suppression filter has the advantage of straightforward integration [145, 146], but its performance is usually limited in RF applications. The N-path filter is a well-known approach that use switches to realize frequency translation [147, 148]. We propose a new RF filtering interference suppression approach — based on the N-path technique — with a very wide dynamic range, which overcomes some of the previous limitations of the N-path approach.

This chapter is organized as follows: Section 4.2 explains the effects of a front-end RF filter on a TV signal suppression. A frequency tunable impedance is presented in Section 4.3, and applied to the tunable RF bandstop as well as bandpass filters that has a wide dynamic range and suppresses the image response in Section 4.4. Since a modulator in the proposed tunable filter is derived by the square wave switching signal, the phase noise requirement for the switching signal is analyzed in Section 4.5. Conclusions are presented in Section 4.6.

4.2 Tunable RF Filter for TV Signal Suppression

A typical CR receiver is shown in Fig. 4.1 (a). The problem of an adjacent TV jammer is especially acute due to the LO phase noise, which interacts with the incoming TV signal through a mixer. This *reciprocal mixing* phenomenon results in an in-band interference that corrupts the desirable signal [149, 150], as shown in Fig. 4.1 (a). A CR device for IEEE 802.22 applications should be able to suppress this in-band interference

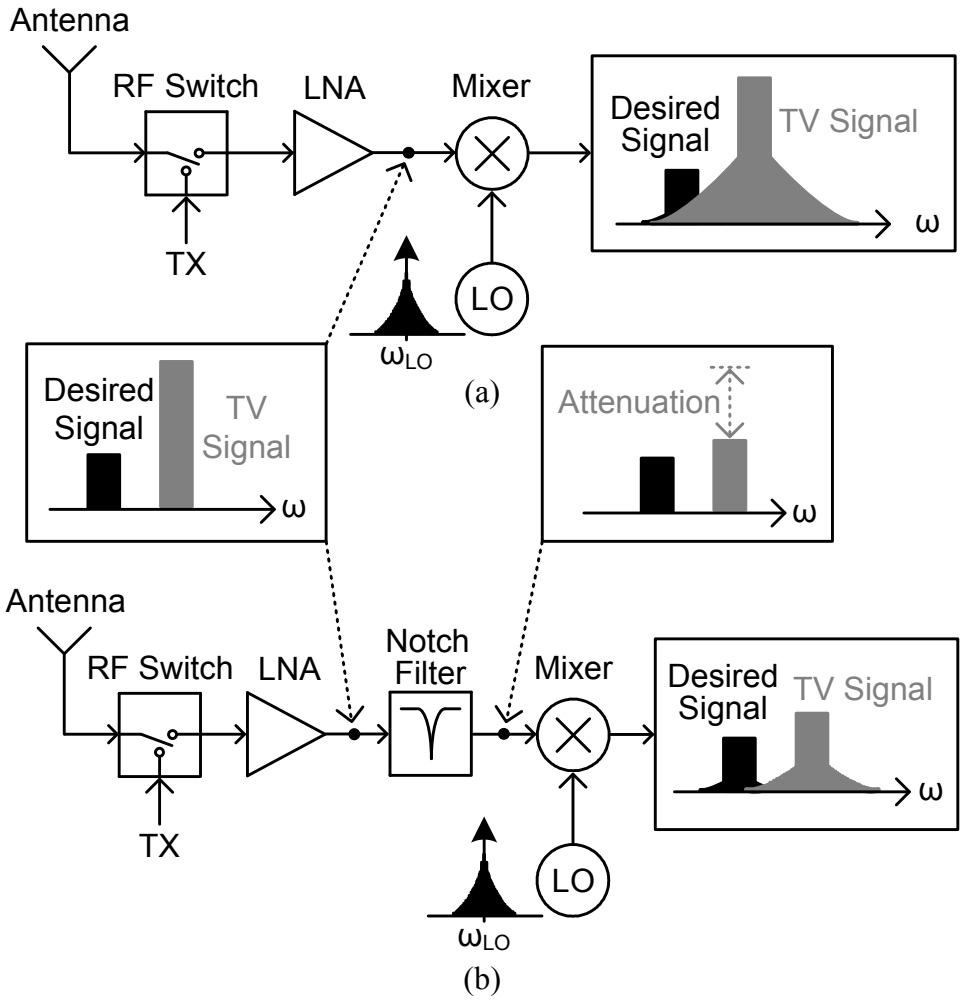

Figure 4.1: (a) IEEE 802.22 cognitive radio receiver without a notch filter, (b) IEEE 802.22 cognitive radio receiver with interference suppression notch filter.

more than 11.2 dB below the desired signal [66].

The PSD of a typical digital TV signal is almost constant within the channel bandwidth, as shown in Fig. 4.2, [7, 151]. The power of the pilot signal in the digital TV spectrum is usually small, compared to the integrated power within the channel bandwidth [151].

On the non-interfering basis of the CR device operation, a strong TV signal can be located as close as one alternate channel [64, 152]. Then, for flat PSD of a digital TV signal in an alternative channel, the power ratio, denoted by ρ_{TV}, between the in-band

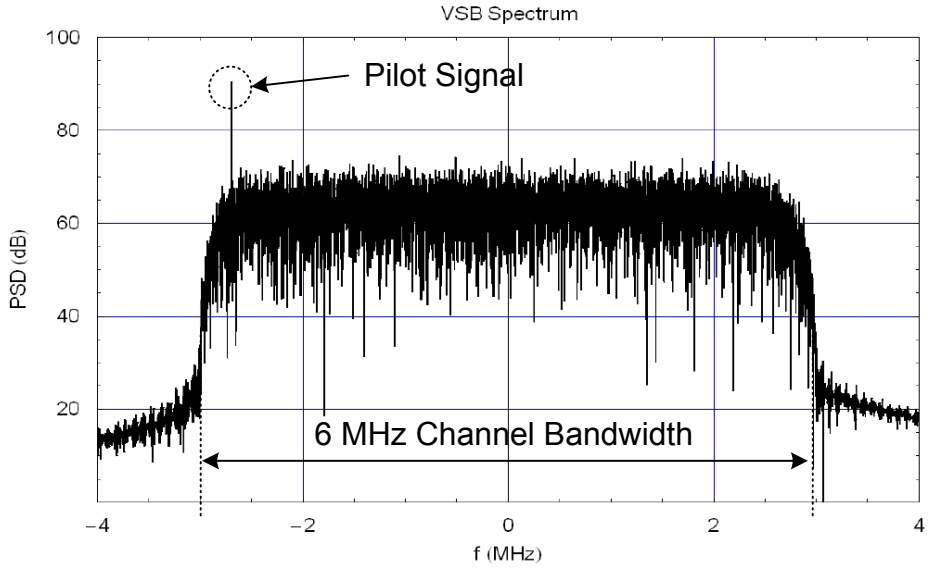

Figure 4.2: Measured Power spectral density of digital TV signal [7].

interference due to the adjacent channel TV signal and the baseband noise due to an AWGN is related to the relative phase noise PSD $\mathfrak{L}(f)$ from (3.47), and given by

$$\begin{aligned}\rho_{TV} &= \rho_W|_{P_W=P_{TV},W_W=2W_{TV}, \text{ and } W_{IFF}=W_W} \\ &= \frac{\pi^2 P_{TV} f^2 \mathfrak{L}(f)}{2\eta_0 W_{TV}^2 W_{PLL}} \left\{ 7W_{TV} \tan^{-1}\left(\frac{7W_{TV}}{2W_{PLL}}\right) - 5W_{TV} \tan^{-1}\left(\frac{5W_{TV}}{2W_{PLL}}\right) \right. \\ &\quad - 3W_{TV} \tan^{-1}\left(\frac{3W_{TV}}{2W_{PLL}}\right) + W_{TV} \tan^{-1}\left(\frac{W_{TV}}{2W_{PLL}}\right) \\ &\quad \left. + 2W_{PLL} \ln\left(\frac{[25W_{TV}^2 + 4W_{PLL}^2][9W_{TV}^2 + 4W_{PLL}^2]}{[49W_{TV}^2 + 4W_{PLL}^2][W_{TV}^2 + 4W_{PLL}^2]}\right) \right\} \end{aligned} \tag{4.1}$$

where f and η_0 denote the frequency offset of LO phase noise from the LO carrier frequency and the single-sided PSD of an AWGN. The quantities P_{TV} and W_{TV} are the power and bandwidth of a received TV signal. Since, in general, the TV channel bandwidth is much greater than the PLL bandwidth (i.e., $W_{TV} \gg W_{PLL}$), (4.1) is reduced to

$$\rho_{TV} \approx \frac{3\pi^2 P_{TV} f^2 \mathfrak{L}(f)}{2\eta_0 W_{TV}^2}. \tag{4.2}$$

Note that the reference SNR at the edge of coverage is 4.3 dB for a quadrature phase-shift keying (QPSK) modulated signal in AWGN environment [66]. Then, the LO phase

noise should be better than $\mathfrak{L}$(100 kHz) = -133 dBc/Hz, in order to suppress the in-band interference more than 11.2 dB below the weakest desired signal with the strongest adjacent channel TV signal [66]. However, this spectral purity is too demanding for a low-cost oscillator to achieve.

In order to alleviate the LO phase noise requirement, it is necessary to place a tunable notch filter prior to the mixer, as shown in Fig. 4.1 (b). With the help of the preceding notch filter, the LO phase noise requirement will be relaxed by approximately the attenuation level of the notch filter. For example, if the notch filter attenuates an alternative channel TV signal by 15 dB, the LO phase noise requirements are relaxed to $\mathfrak{L}$(100 kHz) = -118 dBc/Hz, which is challenging but achievable in monolithic form.

4.3 Tunable Impedance Employing a Balanced Modulator with Image Suppression

For wide and fine RF tuning abilities, a tunable impedance using an ideal balanced modulator-based circuit is shown in Fig. 4.3. Suppose that the modulator is derived by the complementary ideal square wave signals. Then, for an arbitrary load impedance Z_L, the input impedance Z_{in} is given by

$$Z_{in}(\omega) = \frac{4}{\pi^2} \sum_{n=1,3,5...}^{\infty} \frac{1}{n^2} \Big[Z_L(n\omega_{SW} + \omega) + Z_L^*(n\omega_{SW} - \omega) \Big]. \tag{4.3}$$

where ω_{SW} denotes the switching signal frequency [153]. The input impedance of this structure for a capacitive load was analyzed in [154]. However, $Z_{in}(\omega)$ in (4.3) is only valid for an infinite source impedance.

The tunable impedance $Z_{in}(\omega)$ with a real source impedance R_S, which would typically be encountered in most RF applications, is shown in Fig. 4.4 (a). For this analysis, the balanced modulator is driven by a single tone current $I_{in}(t)$ with amplitude A and frequency ω. The output voltage $V_{out}(t)$ for the first half cycle of the switching signal is fully inverted for the second half cycle of the switching signal, as shown in

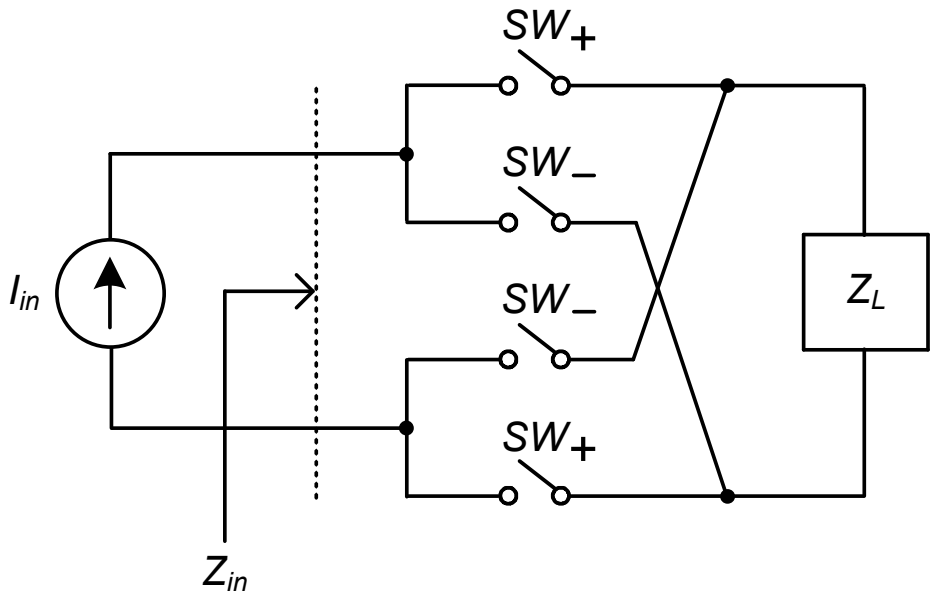

Figure 4.3: Ideal balanced modulator with frequency-dependent load Z_L. The switching signals SW_+ and SW_- denote the complementary ideal square wave signal.

Fig. 4.4 (b) and (c). Analytically,

$$I_{in}(t) = A\cos\omega t, \tag{4.4}$$

$$f_{SW}(t) = \frac{4}{\pi}\sum_{n=1,3,5...}^{\infty}\frac{1}{n}\sin n\omega_{SW}t, \tag{4.5}$$

$$\begin{aligned} V_{out}(t) &= (R_S\|Z_L)I_{in}(t)f_{SW}(t) \\ &= \frac{2A}{\pi}\sum_{n=1,3,5...}^{\infty}\frac{1}{n}\Bigg\{\left|\frac{R_SZ_L(n\omega_{SW}+\omega)}{R_S+Z_L(n\omega_{SW}+\omega)}\right|\sin((n\omega_{SW}+\omega)t+\theta_1) \\ &\quad + \left|\frac{R_SZ_L(n\omega_{SW}-\omega)}{R_S+Z_L(n\omega_{SW}-\omega)}\right|\sin((n\omega_{SW}-\omega)t+\theta_2)\Bigg\} \end{aligned} \tag{4.6}$$

where θ_1 and θ_2 are arguments at each frequencies, defined by

$$\theta_1 = \measuredangle\left[R_SZ_L(n\omega_{SW}+\omega)\right] - \measuredangle\left[R_S+Z_L(n\omega_{SW}+\omega)\right] \tag{4.7}$$

$$\theta_2 = \measuredangle\left[R_SZ_L(n\omega_{SW}-\omega)\right] - \measuredangle\left[R_S+Z_L(n\omega_{SW}-\omega)\right]. \tag{4.8}$$

Since the balanced passive mixer allows bidirectional signal flows, the input voltage $V_{in}(t)$ in Fig. 4.4 (a) is derived by multiplying $V_{out}(t)$ in (4.6) with $f_{SW}(t)$,

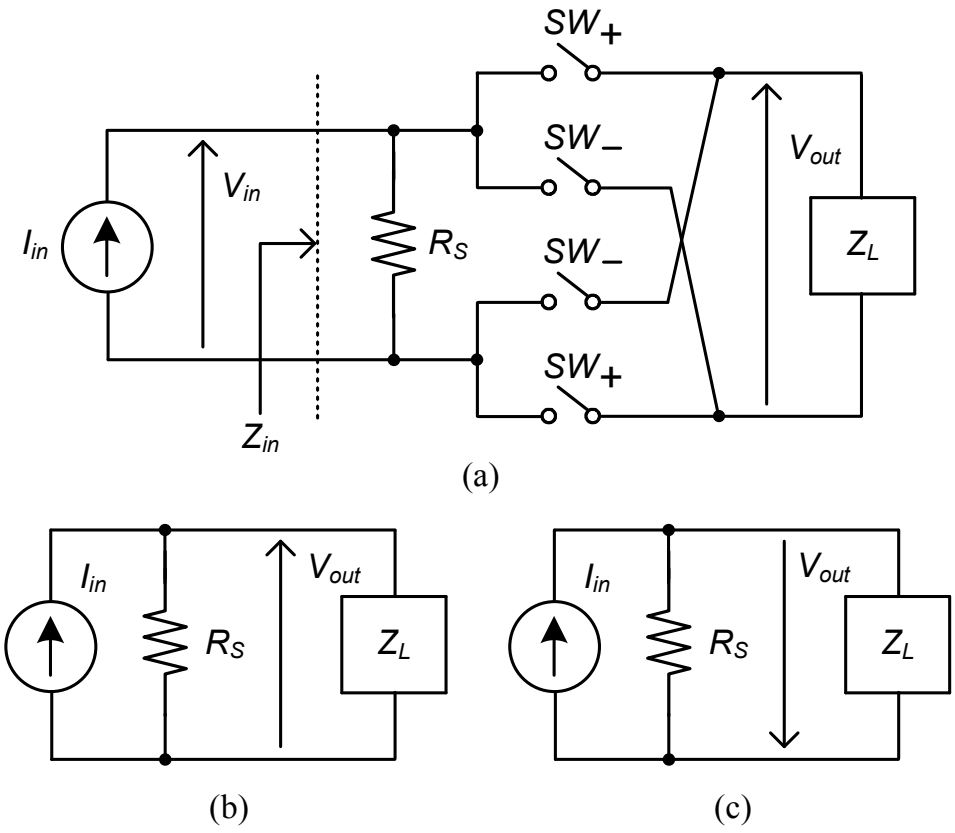

Figure 4.4: (a) Ideal balanced modulator with frequency-dependent load Z_L and real source impedance R_S, (b) Circuit diagram when SW_+ is active, (c) Circuit diagram when SW_- is active.

given by

$$
\begin{aligned}
V_{in}(t) &= V_{out}(t) f_{SW}(t) \\
&= \frac{4A}{\pi^2} \sum_{n=1,3,5\ldots}^{\infty} \sum_{m=1,3,5\ldots}^{\infty} \frac{1}{nm} \times \\
&\quad \Bigg\{ \left| \frac{R_S Z_L(n\omega_{SW}+\omega)}{R_S + Z_L(n\omega_{SW}+\omega)} \right| \cos(((n-m)\omega_{SW}+\omega)t + \theta_1) \\
&\quad - \left| \frac{R_S Z_L(n\omega_{SW}+\omega)}{R_S + Z_L(n\omega_{SW}+\omega)} \right| \cos(((n+m)\omega_{SW}+\omega)t + \theta_1) \\
&\quad + \left| \frac{R_S Z_L(n\omega_{SW}-\omega)}{R_S + Z_L(n\omega_{SW}-\omega)} \right| \cos(((n-m)\omega_{SW}-\omega)t + \theta_2) \\
&\quad - \left| \frac{R_S Z_L(n\omega_{SW}-\omega)}{R_S + Z_L(n\omega_{SW}-\omega)} \right| \cos(((n+m)\omega_{SW}-\omega)t + \theta_2) \Bigg\}. \qquad (4.9)
\end{aligned}
$$

With a method similar to the conversion matrix in [153, 155], the frequency response of the node impedance, $Z_{in}(\omega)$, is defined by the ratio of the coefficients of the same frequency tones between $V_{in}(t)$ and $I_{in}(t)$, and given by

$$
Z_{in}(\omega) = \frac{4}{\pi^2} \sum_{n=1,3,5\ldots}^{\infty} \frac{1}{n^2} \Big[\left(\frac{R_S Z_L(n\omega_{SW}+\omega)}{R_S + Z_L(n\omega_{SW}+\omega)} \right) + \left(\frac{R_S Z_L(n\omega_{SW}-\omega)}{R_S + Z_L(n\omega_{SW}-\omega)} \right)^* \Big]. \qquad (4.10)
$$

This demonstrates the relationship between the baseband impedance Z_L and the high-frequency input impedance (centered at ω_{SW}), created by the frequency translation of the modulator. However, the tunable impedance of Fig. 4.4 has a serious practical limitation due to the image response of the mixer. For example, if a jammer at ω_J is present at the input *along with* the desired signal at ω_S, then the image component of the jammer will be translated to ω_S if $2\omega_{SW} - \omega_J = \omega_S$. This condition is shown in Fig. 4.5. In this case, if the jammer is significantly larger than the desired signal, it will degrade the SNR of the desired signal.

This image signal problem can be mitigated by the use of an image reject (or complex) passive mixer, which will inherently reject the image signal, as shown in Fig. 4.6. An added complication is that the image reject mixer has to maintain near-perfect isolation between the *I* and *Q* paths, which is difficult to achieve with a passive

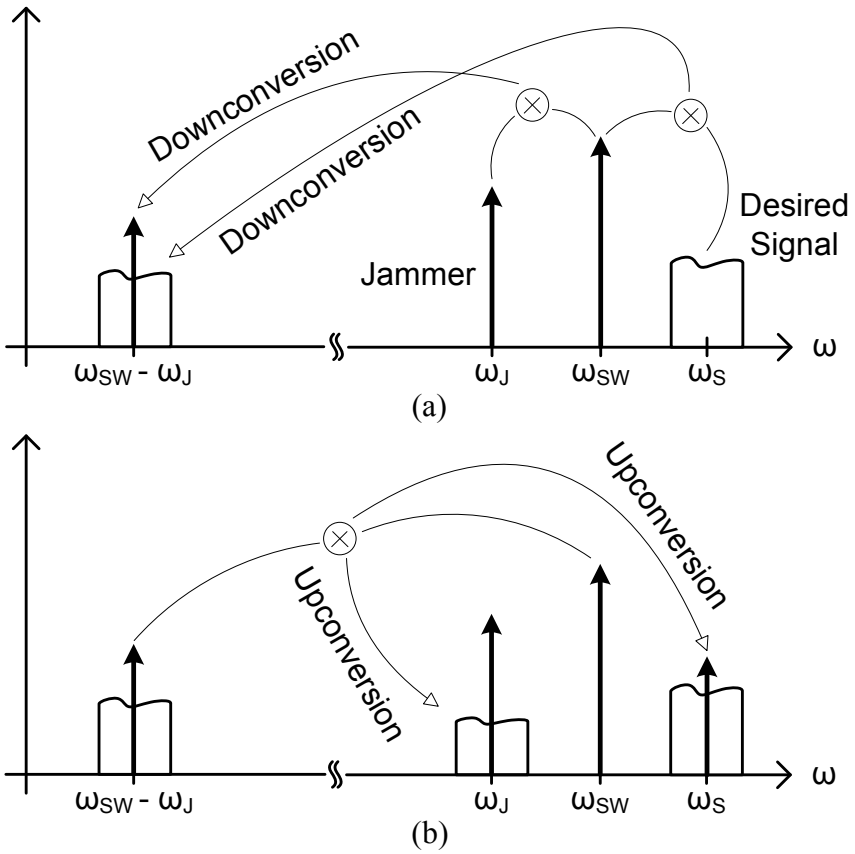

Figure 4.5: (a) Downconversion of the desired signal and jammer to baseband, (b) Upconversion of the downconverted desired signal and jammer. Note that the image response of the mixer causes the jammer to appear at the same frequency as the desired signal

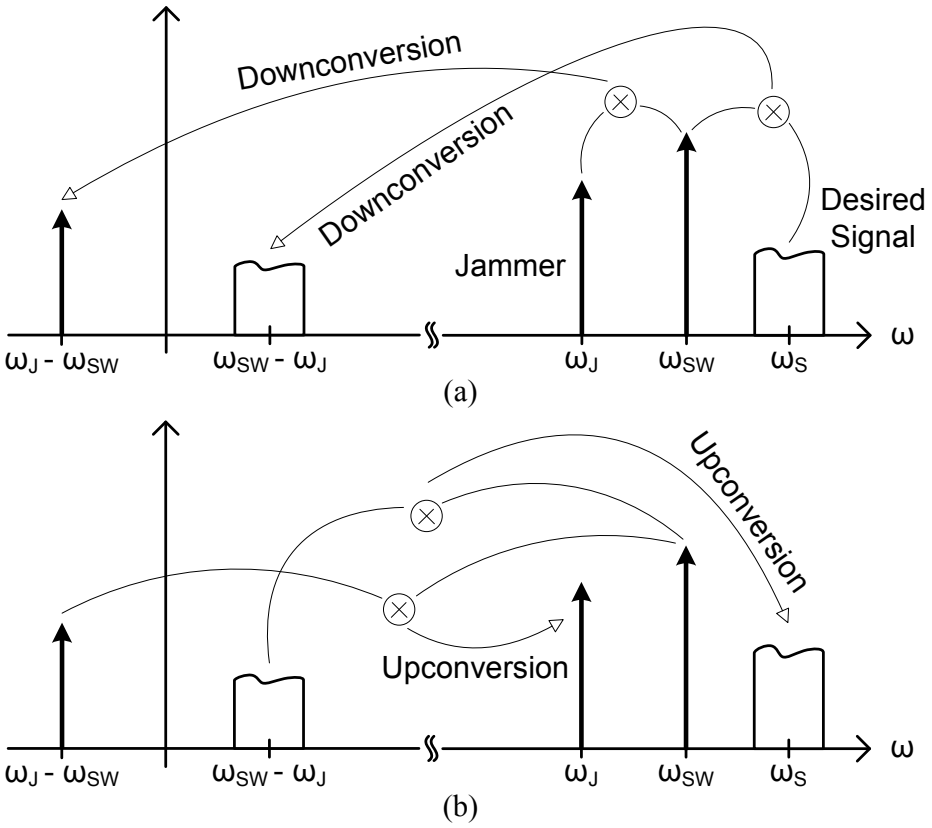

Figure 4.6: (a) Complex downconversion of the desired signal and jammer to baseband, (b) Complex upconversion of the downconverted desired signal and jammer.

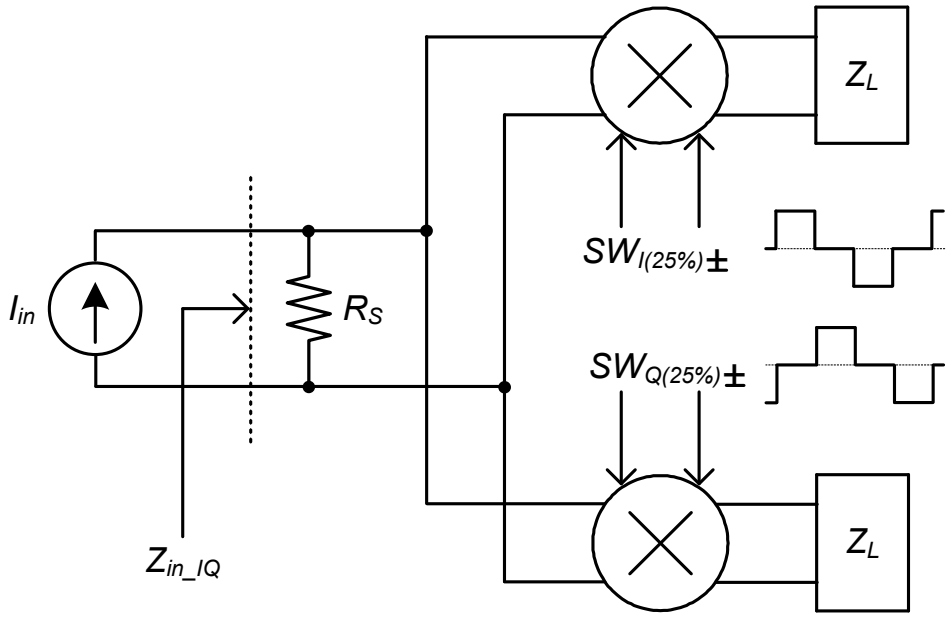

Figure 4.7: Tunable impedance Z_{in-IQ} with image cancellation. The duty cycle of the complementary switching signals have 25% duty cycle.

mixer when employing a 50% duty cycle LO waveform. Therefore, a 25% duty cycle LO waveform is employed to maintain isolation between the *I* and *Q* paths [156]. Figure 4.7 shows the resulting tunable impedance incorporating image cancellation. The input impedance of Fig. 4.7, denoted by Z_{in-IQ}, is given by

$$Z_{in-IQ}(\omega) = \frac{4}{\pi^2} \sum_{n=1,3...}^{\infty} \frac{1}{n^2} \Big[\left(\frac{R_{eq} Z_L(n\omega_{SW} + \omega)}{R_{eq} + Z_L(n\omega_{SW} + \omega)} \right) + \left(\frac{R_{eq} Z_L(n\omega_{SW} - \omega)}{R_{eq} + Z_L(n\omega_{SW} - \omega)} \right)^* \Big], \tag{4.11}$$

where R_{eq} denotes the equivalent source impedance at the input of each *I* and *Q* path (i.e., $R_{eq} = 2R_S$).

For practical consideration, the on-resistance of the transistor switch, $R_{SW(ON)}$, should be incorporated in Fig. 4.7 by connecting $R_{SW(ON)}$ and Z_L in series. Then, the resulting impedance $Z_{in-IQ}(\omega)$ is modified to

$$Z_{in-IQ}(\omega) = \frac{4}{\pi^2} \sum_{n=1,3...}^{\infty} \frac{1}{n^2} \Big[\left(\frac{2R_S[Z_L(n\omega_{SW}+\omega)+R_{SW(ON)}]}{2R_S+[Z_L(n\omega_{SW}+\omega)+R_{SW(ON)}]} \right) + \left(\frac{2R_S[Z_L(n\omega_{SW}-\omega)+R_{SW(ON)}]}{2R_S+[Z_L(n\omega_{SW}-\omega)+R_{SW(ON)}]} \right)^* \Big]. \quad (4.12)$$

The circuit in Fig. 4.7 has the desirable property that it translates a *baseband* impedance to a *tunable* RF, so that the baseband filter response can be replicated at RF, and it suppresses the inevitable image response with a complex passive mixer. It is extremely linear due to the switching action of the transistor, and it is possible low noise due to the low losses of the CMOS switch. In this respect, it is an ideal candidate for a monolithic, tunable, interference suppression application.

4.4 Tunable RF Filters Using Tunable Impedance

Based on the tunable impedance presented in Section 4.3, tunable notch filter as well as bandpass filter are implemented for wide and fine tunnings.

4.4.1 Tunable RF Notch Filter

A tunable RF notch filter is achievable with a parallel LC tank load which has zero impedance at DC. The input impedance of this tunable RF notch filter can be derived from (4.12), and given by

$$Z_{notch}(\omega) = \frac{4}{\pi^2} \sum_{n=1,3,5...}^{\infty} \frac{1}{n^2} \times \Big[\left(\frac{2R_S R_{SW(ON)}[1-(n\omega_{SW}+\omega)^2 L_L C_L] + j2R_S(n\omega_{SW}+\omega)L_L}{(2R_S+R_{SW(ON)})[1-(n\omega_{SW}+\omega)^2 L_L C_L] + j(n\omega_{SW}+\omega)L_L} \right) + \left(\frac{2R_S R_{SW(ON)}[1-(n\omega_{SW}-\omega)^2 L_L C_L] + j2R_S(n\omega_{SW}-\omega)L_L}{(2R_S+R_{SW(ON)})[1-(n\omega_{SW}-\omega)^2 L_L C_L] + j(n\omega_{SW}-\omega)L_L} \right)^* \Big] \quad (4.13)$$

where L_L and C_L denote a inductor and a capacitor in the parallel LC tank load. This tunable notch filter can be merged into the receiver path to suppress the adjacent channel TV signal, as shown in Fig. 4.8.

Table 4.1: Performance and design parameters of tunable RF notch filter

Design Parameter		Filter Performance	
NMOS	300 μm / 0.1 μm	Attenuation[1]	17 dB
L_L	2 μH	Insertion Loss[2]	1.6 dB
C_L	10 pF	Quality Factor	32
R_S	50 Ω	Noise Figure[3]	1.7 dB
Vdd	1 V	$\text{IIP}_{3(notch)}$[4]	16 dBm
		$\text{IIP}_{3(signal)}$[5]	22 dBm

[1]Absolute value of maximum impedance ratio. [2]Absolute value of minimum impedance ratio. [3]Measured at an alternative channel from switching frequency. [4]Measured at the channel of switching frequency. [5]Measured at an alternative channel from switching frequency.

To verify this approach, the filter of Fig. 4.8 is simulated with a 50 Ω source impedance in Fig. 4.9. The simulated filter response shows excellent agreement with the calculated response using (4.13) for the switching frequencies of 515, 605, and 695 MHz corresponding to U.S. TV channels 21, 36, and 51. The dashed line at the bottom of Fig. 4.9 illustrates the variation of the peak attenuation as the switching frequency varies. The switches in the balanced passive mixers are implemented with NMOS transistors in a 90 nm CMOS technology, with an estimated 2.3 Ω switch on-resistance. The design parameters and filter performance of the tunable RF notch filter are summarized in Table 4.1. The large value of the inductor in Fig. 4.8 may require an off-chip component. In Fig. 4.10, the effect of image cancellation is verified by comparing the spectrum of filter output voltage across R_S in Fig. 4.4 without image cancellation technique with that in Fig. 4.8 with image cancellation technique.

4.4.2 Tunable RF Bandpass Filter

A tunable RF bandpass filter can be implemented using a capacitive load which has high impedance at DC, as shown in Fig. 4.11. The input impedance $Z_{BPF}(\omega)$ in

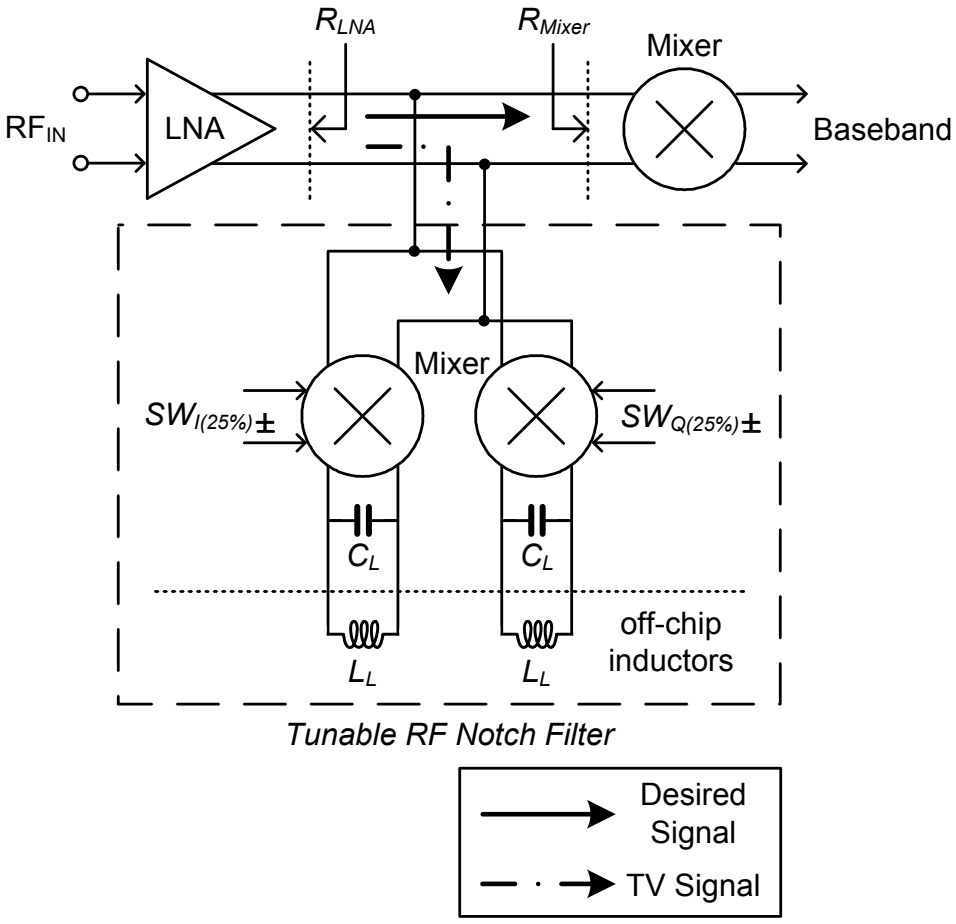

Figure 4.8: Realization of a tunable RF notch filter with wide and fine frequency tuning abilities. The components L_L and C_L consists of a parallel LC tank load. The large value of L_L is recommended to be implemented using an off-chip component.

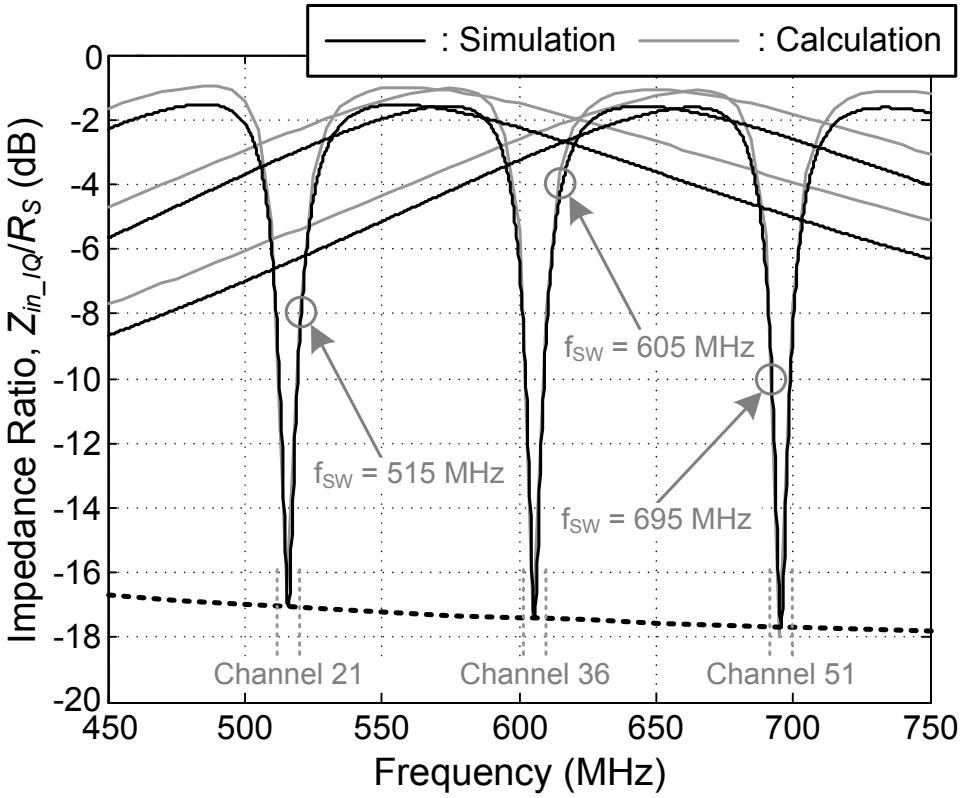

Figure 4.9: Comparison of simulated and calculated impedance ratios for the switching frequencies of 515, 605, and 695 MHz. The dashed line at the bottom illustrates the variation of the peak attenuation as the switching frequency varies.

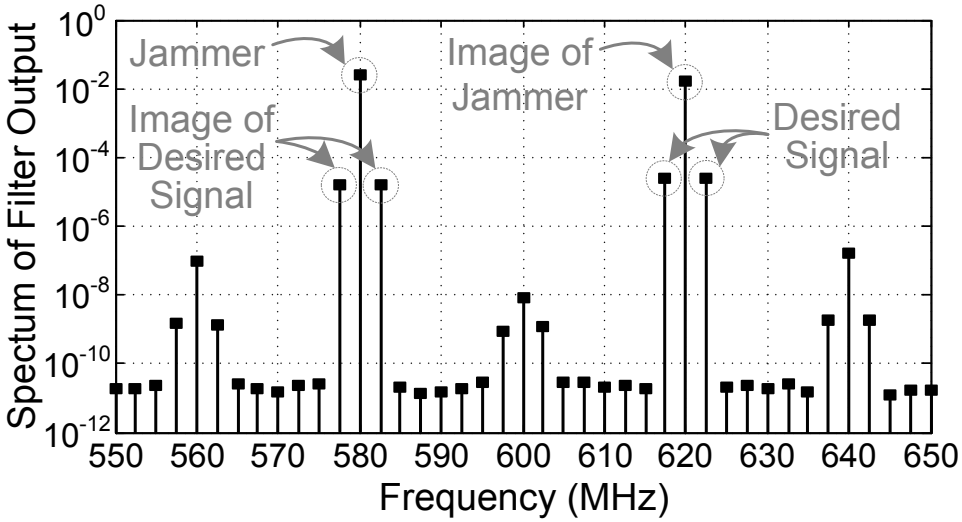

(a)

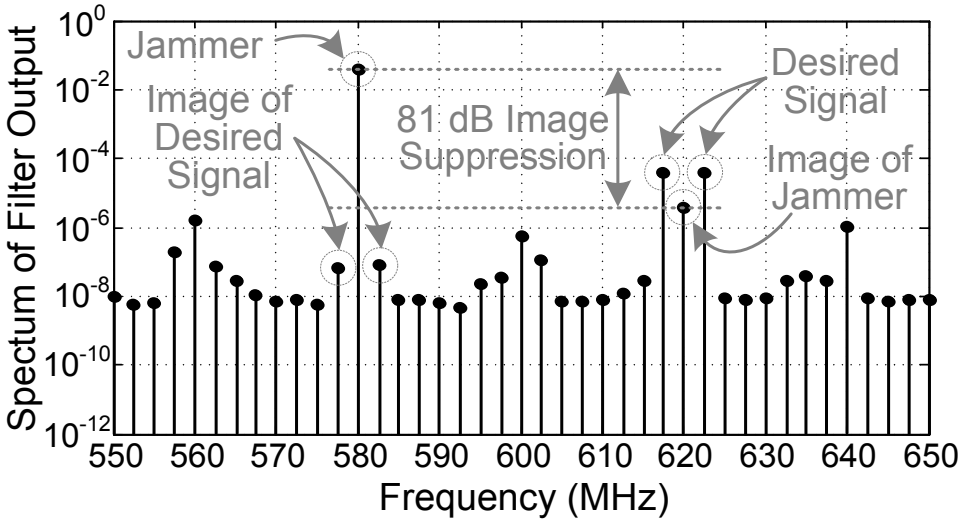

(b)

Figure 4.10: (a) Spectrum of filter output without image cancellation, (b) Spectrum of filter output with image cancellation. Note that the frequencies of the jammer and switching signal are 580 and 600 MHz, respectively. The desired signal is a two-tone signal at 617.5 and 625.5 MHz.

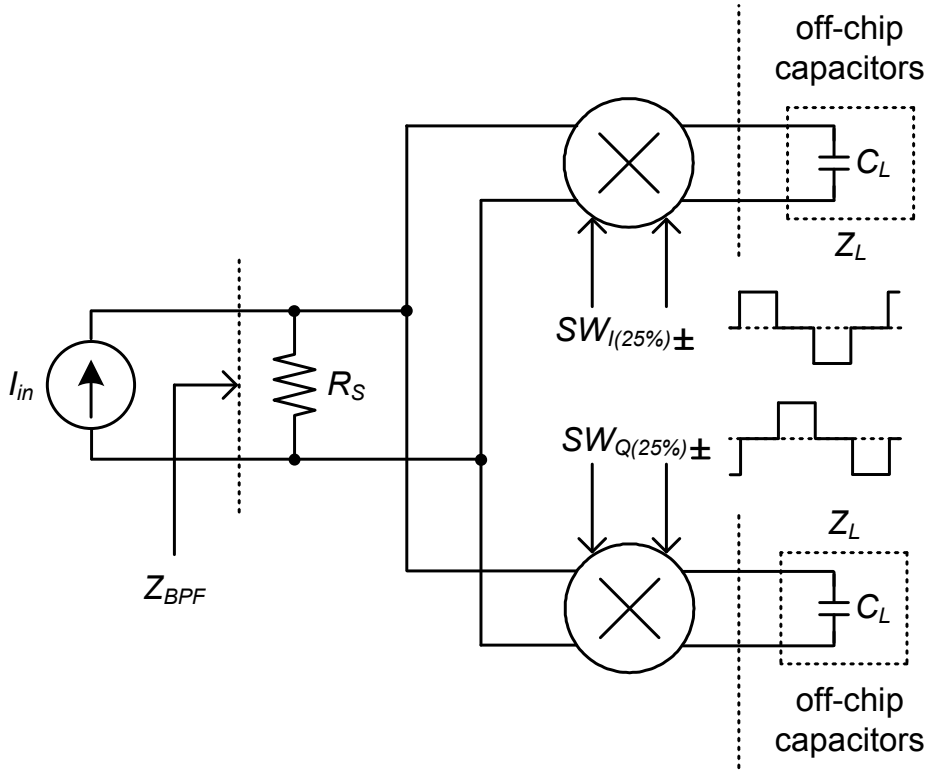

Figure 4.11: Tunable RF bandpass filter with the capacitive loads.

Fig. 4.11 is given by

$$Z_{BPF}(\omega) = \frac{4}{\pi^2} \sum_{n=1,3\ldots}^{\infty} \frac{1}{n^2} \Big[\left(\frac{2R_S + j2R_S R_{SW(ON)}(n\omega_{SW} + \omega)C_L}{1 + j(2R_S + R_{SW(ON)})(n\omega_{SW} + \omega)C_L} \right) + \left(\frac{2R_S + j2R_S R_{SW(ON)}(n\omega_{SW} - \omega)C_L}{1 + j(2R_S + R_{SW(ON)})(n\omega_{SW} - \omega)C_L} \right)^* \Big]. \quad (4.14)$$

where C_L denotes a capacitive load. This tunable RF bandpass filter is simulated with a 50 Ω source impedance, and shows excellent agreement with the calculated response using (4.14) for the switching frequencies of 515, 605, and 695 MHz corresponding to U.S. TV channels 21, 36, and 51 in Fig. 4.12. The dashed line at the top of Fig. 4.12 illustrates the variation of the insertion-loss as the switching frequency varies. The design parameters and filter performance of the tunable bandpass filter are summarized in Table 4.2. The large value of the load capacitors in Fig. 4.11 may require off-chip

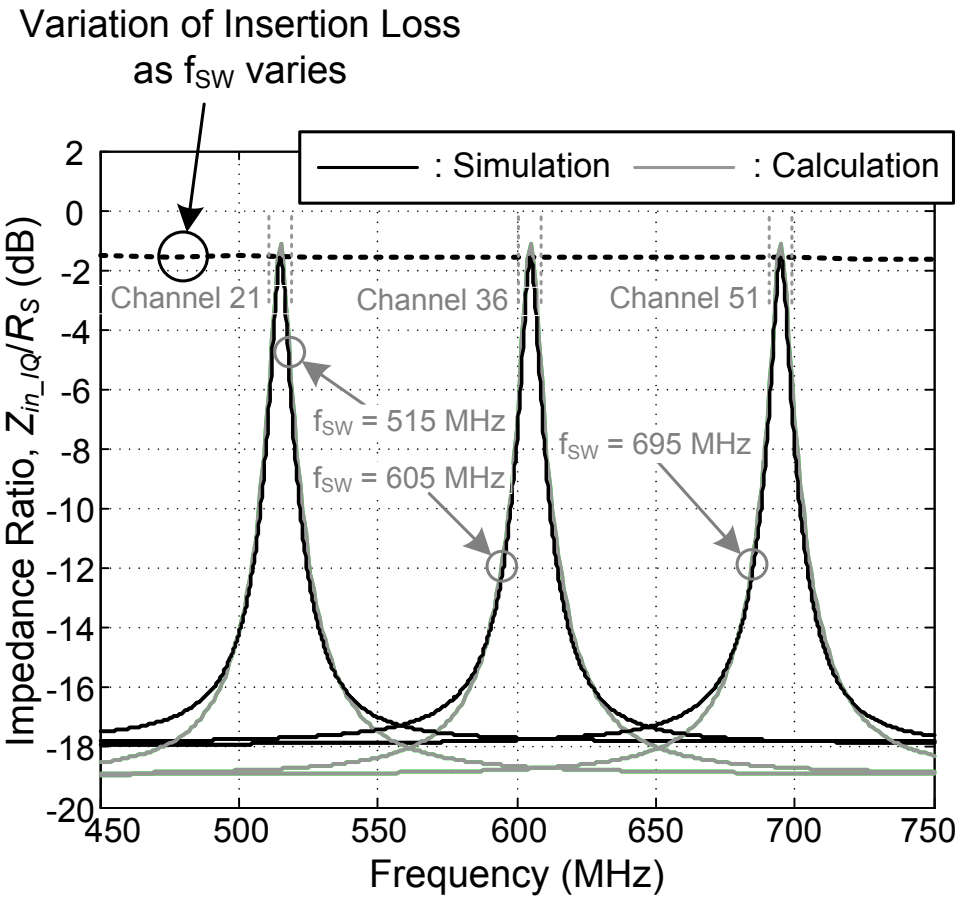

Figure 4.12: Comparison of simulated and calculated impedance ratios for the switching frequencies of 515, 605, and 695 MHz. The dashed line at the top illustrates the variation of the peak attenuation as the switching frequency varies.

Table 4.2: Performance and design parameters of tunable RF bandpass filter

Design Parameter		Filter Performance	
NMOS	300 μm / 0.1 μm	Attenuation[1]	18 dB
C_L	0.53 nF	Insertion Loss[2]	1.8 dB
R_S	50 Ω	3dB Bandwidth	5.5 MHz
Vdd	1 V	Noise Figure[3]	1.7 dB
		$\text{IIP}_{3(bandpass)}$[4]	23 dBm
		$\text{IIP}_{3(bandstop)}$[5]	18 dBm

[1]Absolute value of maximum impedance ratio. [2]Absolute value of minimum impedance ratio. [3]Measured at the bandpass channel. [4]Measured at the bandpass channel. [5]Measured at the bandstop channel.

components.

4.5 Phase Noise Requirement for Switching Signal

Tunable RF filters in Section 4.4 are useful to suppress the adjacent channel TV signal. However, the incoming strong TV signal can also interacts with the phase noise of the switching signal, creating potential in-band interference. The phase noise interaction of the switching signal with a TV signal should be analyzed.

A simplified single-ended tunable impedance using a multiplier is shown in Fig. 4.13 for the analysis of a switching signal phase noise. A noisy switching signal $f_{SW}(t)$ in Fig. 4.13 is given by

$$f_{SW}(t) = 4\sin(\omega_{SW}t + \phi_{SW}(t)) \tag{4.15}$$

where ω_{SW} and $\phi_{SW}(t)$ denote the nominal frequency and the phase noise of a switching signal, respectively. The amplitude of four in $f_{SW}(t)$ is assumed for simplicity.

For this analysis, $I_{in}(t)$ is an ideal single tone current with amplitude A_{in} and frequency ω_{in}. The output current $I_{out}(t)$ in Fig. 4.13 is computed by multiplying $I_{in}(t)$

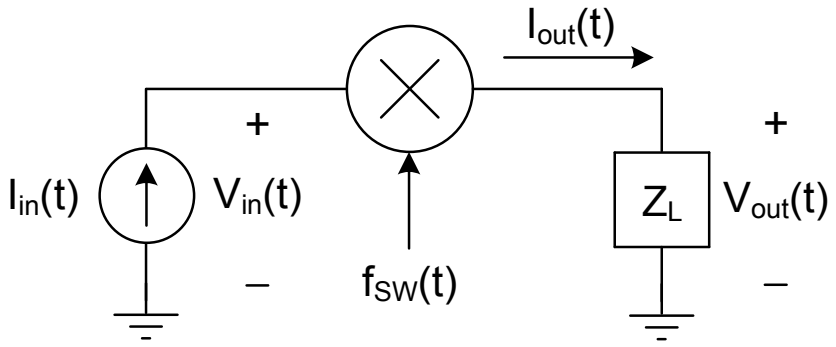

Figure 4.13: Simplified single-ended tunable impedance.

with $f_{SW}(t)$. Then,

$$I_{in}(t) = A_{in}\cos\omega_{in}(t), \tag{4.16}$$

$$\begin{aligned} I_{out}(t) &= I_{in}(t)f_{SW}(t) \\ &= 2A_{in}\left(\sin([\omega_{SW}-\omega_{in}]t+\phi_{SW}(t))+\sin([\omega_{SW}+\omega_{in}]t+\phi_{SW}(t))\right). \end{aligned} \tag{4.17}$$

The output voltage $V_{out}(t)$ is the product of $I_{out}(t)$ and the load impedance Z_L, and given by

$$\begin{aligned} V_{out}(t) = {} & 2A_{in}Z_L(\omega_{SW}-\omega_{in})\sin([\omega_{SW}-\omega_{in}]t+\phi_{SW}(t)+\theta_1) \\ & + 2A_{in}Z_L(\omega_{SW}+\omega_{in})\sin([\omega_{SW}+\omega_{in}]t+\phi_{SW}(t)+\theta_2) \end{aligned} \tag{4.18}$$

where $\theta_1 = \measuredangle[Z_L(\omega_{SW}-\omega_{in})]$ and $\theta_2 = \measuredangle[Z_L(\omega_{SW}+\omega_{in})]$ are arguments at each frequencies. The balanced passive mixer in Fig. 4.13 also works as a voltage commutator with $V_{out}(t)$. Then, $V_{in}(t)$ is given by

$$\begin{aligned} V_{in}(t) &= V_{out}(t)f_{SW}(t) \\ &= A_{in}Z_L(\omega_{SW}-\omega_{in})\cos(\omega_{in}t-\phi_{SW}(t)+\phi_{SW}(t+t_1)-\theta_1) \\ &\quad - A_{in}Z_L(\omega_{SW}-\omega_{in})\cos([2\omega_{SW}-\omega_{in}]t+\phi_{SW}(t)+\phi_{SW}(t+t_1)+\theta_1) \\ &\quad + A_{in}Z_L(\omega_{SW}+\omega_{in})\cos(\omega_{in}t+\phi_{SW}(t)-\phi_{SW}(t+t_2)+\theta_2) \\ &\quad - A_{in}Z_L(\omega_{SW}+\omega_{in})\cos([2\omega_{SW}+\omega_{in}]t+\phi_{SW}(t)+\phi_{SW}(t+t_2)+\theta_2) \end{aligned} \tag{4.19}$$

where t_1 and t_2 denote the time delay for each frequency tone when $I_{out}(t)$ is converted

to $V_{out}(t)$, and are given by

$$t_1 = (\phi_{SW}(t) + \theta_1)/(\omega_{SW} - \omega_{in}) \tag{4.20}$$

$$t_2 = (\phi_{SW}(t) + \theta_2)/(\omega_{SW} + \omega_{in}). \tag{4.21}$$

Note that time delays t_1 and t_2 are also phase noise related random processes, which determine the correlations between $\phi_{SW}(t)$ and $\phi_{SW}(t + t_1)$ and between $\phi_{SW}(t)$ and $\phi_{SW}(t + t_2)$, respectively.

Suppose that the phase noise of the switching signal, $\phi_{SW}(t)$, generally satisfies $|\phi_{SW}(t)| \ll 1$ (i.e., the standard deviation of $\phi_{SW}(t)$ is much less than one radian). Then, $V_{in}(t)$ can be approximated as

$$V_{in}(t) \approx V_{WO\ \phi_{SW}}(t) + V_{With\ \phi_{SW}}(t) \tag{4.22}$$

where $V_{WO\ \phi_{SW}}(t)$ and $V_{With\ \phi_{SW}}(t)$ denote the phase noise independent and related signals in $V_{in}(t)$, and are given by

$$\begin{aligned} V_{WO\ \phi_{SW}}(t) = {} & A_{in} Z_L(\omega_{SW} - \omega_{in}) \cos(\omega_{in} t - \theta_1) \\ & - A_{in} Z_L(\omega_{SW} - \omega_{in}) \cos([2\omega_{SW} - \omega_{in}]t + \theta_1) \\ & + A_{in} Z_L(\omega_{SW} + \omega_{in}) \cos(\omega_{in} t + \theta_2) \\ & - A_{in} Z_L(\omega_{SW} + \omega_{in}) \cos([2\omega_{SW} + \omega_{in}]t + \theta_2) \end{aligned} \tag{4.23}$$

and

$$\begin{aligned} V_{With\ \phi_{SW}}(t) = {} & (\phi_{SW}(t) - \phi_{SW}(t + t_1)) A_{in} Z_L(\omega_{SW} - \omega_{in}) \cos(\omega_{in} t - \theta_1) \\ & + (\phi_{SW}(t) + \phi_{SW}(t + t_1)) A_{in} Z_L(\omega_{SW} - \omega_{in}) \cos([2\omega_{SW} - \omega_{in}]t + \theta_1) \\ & - (\phi_{SW}(t) - \phi_{SW}(t + t_2)) A_{in} Z_L(\omega_{SW} + \omega_{in}) \cos(\omega_{in} t + \theta_2) \\ & + (\phi_{SW}(t) + \phi_{SW}(t + t_2)) A_{in} Z_L(\omega_{SW} + \omega_{in}) \cos([2\omega_{SW} + \omega_{in}]t + \theta_2), \end{aligned} \tag{4.24}$$

respectively. The phase noise independent $V_{WO\ \phi_{SW}}(t)$ is effective to build the desirable input impedance of the tunable filter. However, the phase noise related $V_{With\ \phi_{SW}}(t)$ results from the interaction between $\phi_{SW}(t)$ and a TV signal, and so its spectral skirt overlaps the desired signal band, creating potential in-band interference.

The phase noise related $V_{With\ \phi_{SW}}(t)$ can further categorized as follows:

$$V_{With\ \phi_{SW}}(t) = V_{\omega_{in}}(t) + V_{Images}(t) \tag{4.25}$$

where $V_{\omega_{in}}(t)$ and $V_{Images}(t)$ are given by

$$\begin{aligned} V_{\omega_{in}}(t) = &(\phi_{SW}(t) - \phi_{SW}(t+t_1))A_{in}Z_L(\omega_{SW} - \omega_{in})\cos(\omega_{in}t - \theta_1) \\ &- (\phi_{SW}(t) - \phi_{SW}(t+t_2))A_{in}Z_L(\omega_{SW} + \omega_{in})\cos(\omega_{in}t + \theta_2) \end{aligned} \tag{4.26}$$

and

$$\begin{aligned} V_{Images}(t) = &(\phi_{SW}(t) + \phi_{SW}(t+t_1))A_{in}Z_L(\omega_{SW} - \omega_{in})\cos([2\omega_{SW} - \omega_{in}]t + \theta_1) \\ &+ (\phi_{SW}(t) + \phi_{SW}(t+t_2))A_{in}Z_L(\omega_{SW} + \omega_{in})\cos([2\omega_{SW} + \omega_{in}]t + \theta_2), \end{aligned} \tag{4.27}$$

respectively. If the inphase and quadrature signals of the switching signal is generated by a single frequency tone, then the phase noises of the inphase and quadrature signals are strongly correlated, and so $V_{Images}(t)$ is cancelled or sufficiently suppressed by the use of an image rejection structure in Section 4.3. Therefore, $V_{\omega_{in}}(t)$ is responsible for the phase noise problems of the switching signal. Suppose that the phases θ_1 and θ_2 are uniformly distributed random variables. Then, the variance of $V_{\omega_{in}}(t)$ is given by

$$\begin{aligned} \sigma^2_{V_{\omega_{in}}} &= E[V^2_{\omega_{in}}(t)] - E^2[V_{\omega_{in}}(t)] \\ &= (\sigma^2_{\phi_{SW}} - R_{\phi_{SW}}(t_1))A^2_{in}Z^2_L(\omega_{SW} - \omega_{in}) \\ &\quad + (\sigma^2_{\phi_{SW}} - R_{\phi_{SW}}(t_2))A^2_{in}Z^2_L(\omega_{SW} + \omega_{in}). \end{aligned} \tag{4.28}$$

where $R_{\phi_{SW}}(t_1)$ and $R_{\phi_{SW}}(t_2)$ denote the correlation function between $\phi_{SW}(t)$ and $\phi_{SW}(t_1)$ and between $\phi_{SW}(t)$ and $\phi_{SW}(t_2)$, respectively. There are two distinguished attenuation factors in the switching signal phase noise interaction with a TV signal from the typical *reciprocal mixing* phenomenon in Chapter 3. First, the correlations between $\phi_{SW}(t)$ and $\phi_{SW}(t_1)$ and between $\phi_{SW}(t)$ and $\phi_{SW}(t_2)$ effectively suppress the phase noise problems of the switching signal. For instance, if they are perfectly correlated, then both $R_{\phi_{SW}}(t_1)$ and $R_{\phi_{SW}}(t_2)$ are equal to $\sigma^2_{\phi_{SW}}$. Then, the phase noise of the switching signal does not induce any interference problem at all. Second, the phase noise interaction of the switching signal is suppressed by the load impedance. This suppression is more than 15 dB, as shown in Section 4.4. The suppression mechanism of

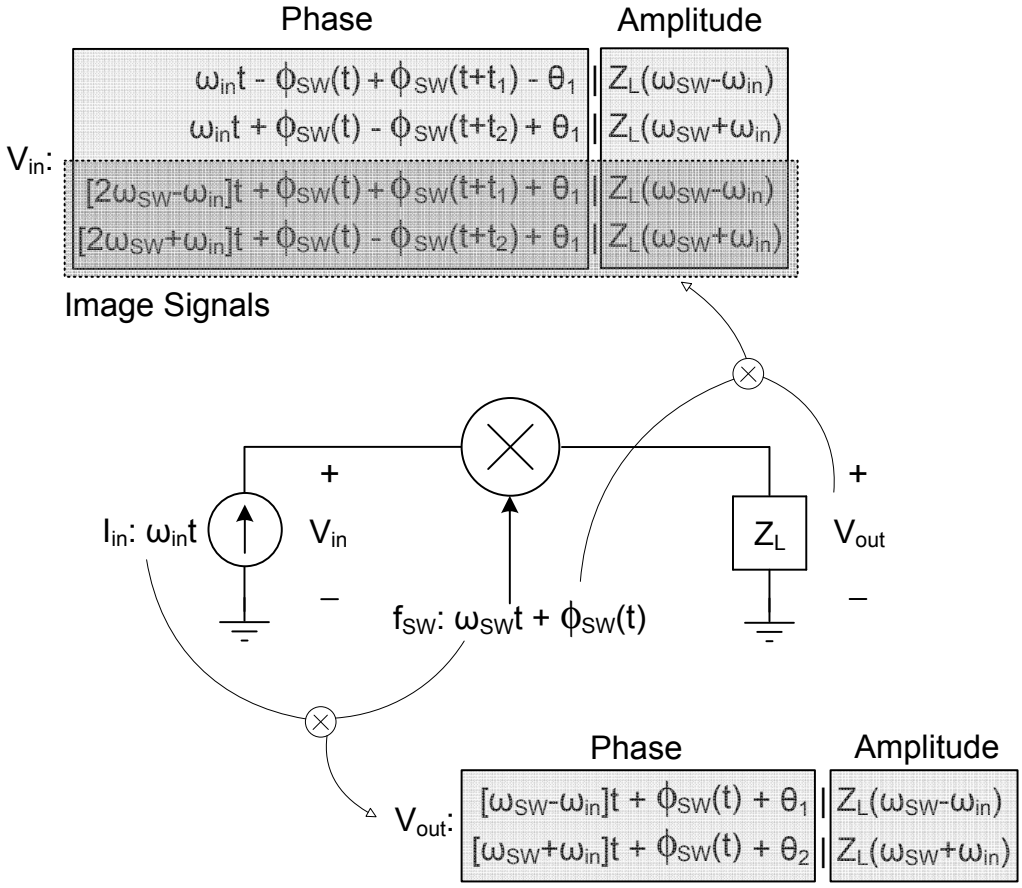

Figure 4.14: Phase and amplitude domain analyses for the switching signal phase noise.

the phase noise effects of a switching signal is depicted in Fig. 4.14. As a result, the phase noise of the switching signal does not create serious interference problem. The phase noise requirement of the switching signal is much relaxed by about $15 \sim 25$ dB when compared with that of the LO signal in downconversion path.

4.6 Conclusion

A wide dynamic range low-power CMOS-based RF tunable filter with image cancellation is presented for the IEEE 802.22 cognitive radio applications, in order to suppress a strong TV signal. The tunable RF notch filter with 17 dB attenuation and 1.6 dB insertion loss is achieved using the parallel LC tank load. A tunable RF bandpass is

implemented with a capacitive termination. It achieved 18 dB maximum attenuation and 1.8 dB insertion loss. These tunable RF ftilers will have a wide range of potential applications where a single interfering signal must be suppressed, without compromising the SNR of a desired signal.

This chapter has been published in part for the following publications:

1. Sanghoon Park, Wingching V. Leung, and Lawrence E. Larson, "An improved wide-dynamic range tunable RF interference suppression notch filter," to appear in *Proc. IEEE International Symposium on Circuits and Systems*, May 2010.

Chapter 5

Conclusion

Cognitive radio is a type of radio standard, which can adaptively detect and access unoccupied frequency bands to manage the frequency allocation problem due to the spectrum crowding by multiple wireless devices. By allowing multiple devices to operate in the same frequency bands, cognitive radio is effective in increasing the spectral efficiency. However, there is an inevitable interference problem between the primary licensed users and the unlicensed cognitive radio devices.

This dissertation focuses on the cognitive radio operation, and can be divided into two broad topics. The first part of this dissertation discusses the detection technique using the radiated LO leakage from a nearby mobile terminal. This detection method can be useful for short–range wireless communications, and so is applied to the coexistence problems between the UWB and WiMAX systems. The UWB system can be characterized by its short range of 10 m, low effective isotropic radiation power (EIRP) of -41.25 dBm/MHz, and wide signal bandwidth of 7.5 GHz. The most likely frequencies for mobile WiMAX system are the licensed spectrum bands at 2.3, 2.5, 3.3, and 3.5 GHz. Therefore, the mobile WiMAX system in the 3 GHz frequency band is quite susceptible to potential interference from UWB devices.

Once a WiMAX channel is set up, there are two synchronized wireless connections — uplink and downlink — between a WiMAX AP and a MT. Both connections are useful for a UWB device to detect the presence of a WiMAX MT. However, there will be a potential interference problem with an unsynchronized WiMAX MT which does not have a stable wireless connection with a WiMAX AP. The transmitted UWB

signal can be harmful to an unsynchronized WiMAX MT in the sense of preventing it from receiving a signal from a WiMAX AP. The essence of the proposed technique is to sense the incoming LO leakage of an unsynchronized WiMAX MT that is within the UWB interference range, thus enabling the UWB device to avoid the spectrum of the unsynchronized WiMAX MT.

The proposed detection technique uses the DFT magnitude response to determine the presence of an LO leakage signal. The probabilities of false alarm and missed detection are derived to quantify the DFT-based detection performance. There is a tradeoff between P_{FA} and P_{MD} when adjusting the number of samples and the decision threshold of the DFT. Compared with a radiometer, the DFT-based detector shows higher detection sensitivity and more robust detection performance to estimation error if the power spectral density of the ambient noise is unknown. Systematic limitations on the detection performance are also investigated.

The second part of this dissertation focuses on the analysis of LO phase noise interaction with an adjacent channel signal through a mixer. Since the received LO leakage is generally very weak, the sensitivity of the UWB detector is a great concern. Local oscillator phase noise can degrade the detection sensitivity if there is a significant adjacent channel signal. Spectrum broadening is the main reason that causes the energy of a strong adjacent channel signal to spill over and become in-band interference in adjacent channels. Accurate expressions for the resulting in-band interference are presented for an adjacent channel WiMAX signal. The effects of the in-band interference on the detection performance are evaluated with the probabilities of false alarm and missed detection. Since the bandwidth of the front-end RF filter should be large enough to cover the whole system band, the LO phase noise interaction with an adjacent channel signal through a multiplier is inevitable. Therefore, the local oscillator has to be designed so that the phase noise has been sufficiently suppressed.

Spectrum broadening of the LO phase noise interaction with a TV signal is applied to CR device operation in UHF bands. Recently, the FCC released an order allowing personal portable devices to operate in unoccupied TV channels between 21 and 51 — except 37 — for IEEE 802.22 cognitive radio applications. Since a CR device must coexist with commercial TV systems, the presence of a strong adjacent TV signal

is a challenging problem. Therefore, an interference suppression filtering technique is highly desired to suppress the strong TV signals. This filter must be tunable over a wide frequency range, because the channel allocation of the TV signal will depend on the geographic location of the CR device, and is outside of the control of the CR network. A wide dynamic range low-power CMOS-based RF tunable filter with image cancellation is presented using a balanced passive complex mixer and frequency dependent loads. The tunable RF notch filter with 17 dB attenuation and 1.6 dB insertion loss is achieved using parallel LC tank loads. A tunable RF bandpass is implemented with capacitive termination. It achieved 18 dB maximum attenuation and 1.8 dB insertion loss. These tunable RF tilers will have a wide range of potential applications where a single interfering signal must be suppressed, without compromising the SNR of the desired signal.

References

[1] R. V. Prasad, P. Pawelczak, J. A. Hoffmeyer, and H. S. Berger, "Cognitive functionality in next generation wireless networks: standardization efforts," *IEEE Commun. Mag.*, vol. 46, no. 4, pp. 72–78, April 2008.

[2] FCC, "First report and order, revision of part 15 of the commission's rules regarding ultra-wideband transmission systems," ET Docket, pp. 98-153, Feb. 14, 2002.

[3] A. Batra, J. Balakrishnan, G. R. Aiello, J. R. Foerster, and A. Dabak, "Design of a multiband OFDM system for realistic UWB channel environments," *IEEE Trans. Microw. Theory Tech.*, vol. 52, no. 9, pp. 2123–2138, Sept. 2004.

[4] LAN / MAN Standards Committee of the IEEE Computer Society and the IEEE Microwave Theory and Techniques Society, Local and Metropolitan Area Networks - Part 16: Air Interface for Fixed Broadband Wireless Access Systems, IEEE Std. 802.16-2004, 2004.

[5] LAN / MAN Standards Committee of the IEEE Computer Society and the IEEE Microwave Theory and Techniques Society, Local and Metropolitan Area Networks - Part 16: Air Interface for Fixed Broadband Wireless Access Systems - Amendment for Physical and Medium Access Control Layers for Combined Fixed and Mobile Operation in Licensed Bands, IEEE Std. 802.16e-2005, 2005.

[6] A. Sahai, N. Hoven, and R. Tandra, "Some fundamental limits on cognitive radio," in *Proc. Allerton Conference on Communication, Control, and Computing*, Oct. 2004.

[7] S. J. Shellhammer, S. Shankar N, R. Tandra, and J. Tomcik, "Performance of power detector sensors of DTV signals in IEEE 802.22 WRANs," in *Proceedings of the first international workshop on Technology and policy for accessing spectrum*, 2006.

[8] J. G. Andrews, A. Ghosh, and R. Muhamed, *Fundamentals of WiMAX, Understanding Broadband Wireless Networking*. Prentice Hall USA, 2007.

[9] WiMAX Forum, "Mobile WiMAX - part I: a technical overview and performance evaluation," Aug. 2006, [Online] available: http://www.wimaxforum.org/technology/downloads/Mobile_WiMAX_Part1_Overview_and_Performance.pdf.

[10] U. S. Department of Commerce, National Telecommunications and Information Administration, Office of Spectrum Management, "United states, frequency allocations, the radio spectrum," Oct. 2003, [Online] available: http://www.ntia.doc.gov/osmhome/allochrt.pdf.

[11] M. Lebherz, W. Wiesbeck, and W. Krank, "A versatile wave propagation model for the VHF/UHF range considering three-dimensional terrain," *IEEE Trans. Antennas Propag.*, vol. 40, no. 10, pp. 1121–1131, Oct. 1992.

[12] G. J. M. Janssen, P. A. Stigter, and R. Prasad, "Wideband indoor channel measurements and BER analysis of frequency selective multipath channels at 2.4, 4.75, and 11.5 GHz," *IEEE Trans. Commun.*, vol. 44, no. 10, pp. 1272–1288, Oct. 1996.

[13] C. Cordeiro, K. Challapali, D. Birru, and N. Sai Shankar, "IEEE 802.22: the first worldwide wireless standard based on cognitive radios," in *Proc. First IEEE International Symposium on New Frontiers in Dynamic Spectrum Access Networks DySPAN 2005*, 8–11 Nov. 2005, pp. 328–337.

[14] J. Mitola III, "Cognitive radio for flexible mobile multimedia communications," in *Proc. (MoMuC '99) 1999 IEEE International Workshop on Mobile Multimedia Communications*, 15–17 Nov. 1999, pp. 3–10.

[15] ——, "Cognitive radio: an integrated agent architecture for software radio architecture," Ph.D. dissertation, Ph. D Dissertation, Royal Institute of Technology (KTH), 2000.

[16] W. H. W. Tuttlebee, "Software-defined radio: facets of a developing technology," *IEEE Personal Communications*, vol. 6, no. 2, pp. 38–44, April 1999.

[17] A. A. Abidi, "Phase noise and jitter in CMOS ring oscillators," *IEEE J. Solid-State Circuits*, vol. 41, no. 8, pp. 1803–1816, Aug. 2006.

[18] A. C. Tribble, "The software defined radio: Fact and fiction," in *Proc. IEEE Radio and Wireless Symposium*, 22–24 Jan. 2008, pp. 5–8.

[19] S. Haykin, "Cognitive radio: brain-empowered wireless communications," *IEEE J. Sel. Areas Commun.*, vol. 23, no. 2, pp. 201–220, Feb 2005.

[20] R. W. Thomas, L. A. DaSilva, and A. B. MacKenzie, "Cognitive networks," in *Proc. First IEEE International Symposium on New Frontiers in Dynamic Spectrum Access Networks DySPAN 2005*, 8–11 Nov. 2005, pp. 352–360.

[21] N. Devroye, M. Vu, and V. Tarokh, "Cognitive radio networks," *IEEE Signal Process. Mag.*, vol. 25, no. 6, pp. 12–23, November 2008.

[22] L. Song, "Cognitive networks: standardizing the large scale wireless systems," in *Proc. 5th IEEE Consumer Communications and Networking Conference CCNC 2008*, 10–12 Jan. 2008, pp. 988–992.

[23] V. Anantharam, "The stability region of the finite-user slotted ALOHA protocol," *IEEE Trans. Inf. Theory*, vol. 37, no. 3, pp. 535–540, May 1991.

[24] FCC, "First report and order, authorization of spread spectrum systems under parts 15 and 90 of the FCC rules and regulations," Gen. Docket 81-413; FCC 85-245, June 18 1985.

[25] M. Hamalainen, V. Hovinen, R. Tesi, J. H. J. Iinatti, and M. Latva-aho, "On the UWB system coexistence with GSM900, UMTS/WCDMA, and GPS," *IEEE J. Sel. Areas Commun.*, vol. 20, no. 9, pp. 1712–1721, Dec. 2002.

[26] S. M. Mishra and R. W. Brodersen, "Cognitive technology for improving ultra-wideband (UWB) coexistence," in *Proc. IEEE International Conference on Ultra-Wideband ICUWB 2007*, 24–26 Sept. 2007, pp. 253–258.

[27] A. Durantini, R. Giuliano, F. Mazzenga, and D. Valente, "Analysis of UWB interference to WiMAX for detect and avoid procedures," in *Proc. IEEE 18th International Symposium on Personal, Indoor and Mobile Radio Communications PIMRC 2007*, 3–7 Sept. 2007, pp. 1–5.

[28] A. Rahim, S. Zeisberg, A. Idriss, and A. Finger, "The impact of UWB interference on WiMax client receiver: detect and avoid," in *Proc. 3rd International Conference on Information and Communication Technologies: From Theory to Applications ICTTA 2008*, 7–11 April 2008, pp. 1–6.

[29] M. Chiani and A. Giorgetti, "Coexistence between UWB and narrow-band wireless communication systems," *Proc. IEEE*, vol. 97, no. 2, pp. 231–254, Feb. 2009.

[30] S. Kandeepan, G. Baldini, and R. Piesiewicz, "Preliminary experimental results on the spectrum sensing performances for UWB-cognitive radios for detecting IEEE 802.11n systems," in *Proc. 6th International Symposium on Wireless Communication Systems ISWCS 2009*, 7–10 Sept. 2009, pp. 111–115.

[31] FCC, "In the matter of unlicensed operation in the TV broadcast bands: second report and order and memorandum opinion and order," Tech. Rep. 08-260, Nov. 14 2008.

[32] D. Niyato and E. Hossain, "Cognitive radio for next-generation wireless networks: an approach to opportunistic channel selection in ieee 802.11-based wireless mesh," *IEEE Wireless Commun. Mag.*, vol. 16, no. 1, pp. 46–54, February 2009.

[33] T. Yucek and H. Arslan, "A survey of spectrum sensing algorithms for cognitive radio applications," *IEEE Communications Surveys & Tutorials*, vol. 11, no. 1, pp. 116–130, First Quarter 2009.

[34] J. Proakis, *Digital Communications*, 4th ed. McGraw-Hill New York, 2000.

[35] R. E. Ziemer and W. H. Tranter, *Principles of Communications: Systems, Modulation, and Noise*, 5th ed. John Wiley & Sons Inc., 2002.

[36] G. L. Turin, "An introduction to matched filters," *IRE Transactions on Information Theory*, vol. 6, no. 3, pp. 311–329, June 1960.

[37] M. Padmanabhan and K. W. Martin, "Comparison of correlator configurations for FSK demodulation," in *Proc. IEEE International Symposium on Circuits and Systems*, 1–3 May 1990, pp. 1203–1206.

[38] S. M. Kay, *Fundamentals of Statistical Signal Processing, Volume II, Detection Theory*. Prentice-Hall, 1998.

[39] H. Urkowitz, "Energy detection of unknown deterministic signals," *Proc. IEEE*, vol. 55, no. 4, pp. 523–531, April 1967.

[40] A. Sonnenschein and P. M. Fishman, "Radiometric detection of spread-spectrum signals in noise of uncertain power," *Aerospace and Electronic Systems, IEEE Transactions on*, vol. 28, no. 3, pp. 654–660, July 1992.

[41] A. Fonte, D. Zito, B. Neri, and F. Alimenti, "Feasibility study and design of a low-cost system-on-a-chip microwave radiometer on silicon," in *Proc. International Waveform Diversity and Design Conference*, 4–8 June 2007, pp. 37–41.

[42] R. Tandra and A. Sahai, "SNR Walls for Signal Detection," *IEEE Journal of Selected Topics in Signal Processing*, vol. 2, no. 1, pp. 4–17, Feb. 2008.

[43] S. Geirhofer, L. Tong, and B. M. Sadler, "A measurement-based model for dynamic spectrum access in WLAN channels," in *Proc. Military Communications Conference MILCOM 2006*, 23–25 Oct. 2006, pp. 1–7.

[44] W. A. Gardner, *Statistical Spectral Analysis: a Nonprobabilistic Theory*. John Wiley & Sons Inc., 1988.

[45] ——, "Signal interception: a unifying theoretical framework for feature detection," *IEEE Trans. Commun.*, vol. 36, no. 8, pp. 897–906, Aug. 1988.

[46] ——, "Exploitation of spectral redundancy in cyclostationary signals," *IEEE Signal Process. Mag.*, vol. 8, no. 2, pp. 14–36, April 1991.

[47] IEEE 802.15 Working Group, http://www.ieee802.org/15/.

[48] IEEE 802.16 Working Group, http://www.ieee802.org/16/.

[49] H. Ochiai and H. Imai, "On the distribution of the peak-to-average power ratio in OFDM signals," *Communications, IEEE Transactions on*, vol. 49, no. 2, pp. 282–289, Feb. 2001.

[50] R. Van Nee and R. Prasad, *OFDM for Wireless Multimedia Communications*. Artech House, Inc. Norwood, MA, USA, 2000.

[51] S. H. Muller and J. B. Huber, "OFDM with reduced peak-to-average power ratio by optimum combination of partial transmit sequences," *Electronics Letters*, vol. 33, no. 5, pp. 368–369, 27 Feb. 1997.

[52] X. Huang, J. Lu, J. Zheng, and J. Gu, "Reduction of PAPR of OFDM signals with piecewise-scales transform," in *Proc. VTC 2002-Fall Vehicular Technology Conference 2002 IEEE 56th*, vol. 2, 24–28 Sept. 2002, pp. 1240–1243.

[53] X. Huang, J. Lu, J. Zheng, K. B. Letaief, and J. Gu, "Companding transform for reduction in peak-to-average power ratio of OFDM signals," *IEEE Trans. Wireless Commun.*, vol. 3, no. 6, pp. 2030–2039, Nov. 2004.

[54] Z. Zhang, Y. Wu, and J. Hou, "An improved scheme of reducing peak-to-average power ratio in OFDM systems," in *Proc. IEEE 6th Circuits and Systems Symposium on Emerging Technologies: Frontiers of Mobile and Wireless Communication*, vol. 2, 31 May–2 June 2004, pp. 469–471.

[55] P. Tu, X. Huang, and E. Dutkiewicz, "Peak-to-average power ratio performance of interleaved spread spectrum OFDM signals," in *Proc. International Symposium on Communications and Information Technologies ISCIT '07*, 17–19 Oct. 2007, pp. 82–86.

[56] FCC, "Notice of proposed rule making," ET Docket, no. 04-113, May 25 2004.

[57] ——, "Spectrum policy task force report," ET Docket, no. 02-155, Nov. 02 2002.

[58] D. Cabric, S. M. Mishra, and R. W. Brodersen, "Implementation issues in spectrum sensing for cognitive radios," in *Conference Record of the Thirty-Eighth Asilomar Conference on Signals, Systems and Computers*, vol. 1, 7–10 Nov. 2004, pp. 772–776.

[59] A. L. Michael J. Marcus, Paul Kolodzy, "Reclaiming the vast wasteland: why unlicensed use of the white space in the TV bands will not cause interference to DTV viewers," *New America Foundation: Wireless Future Program, Issue Brief no. 17*, Oct. 2005.

[60] IEEE 802.22 Working Group, http://www.ieee802.org/22/.

[61] J. Walfisch and H. L. Bertoni, "A theoretical model of UHF propagation in urban environments," *IEEE Trans. Antennas Propag.*, vol. 36, no. 12, pp. 1788–1796, Dec. 1988.

[62] H. L. Bertoni, W. Honcharenko, L. R. Macel, and H. H. Xia, "UHF propagation prediction for wireless personal communications," *Proc. IEEE*, vol. 82, no. 9, pp. 1333–1359, Sept. 1994.

[63] C. Cordeiro, M. Ghosh, D. Cavalcanti, and K. Challapali, "Spectrum sensing for dynamic spectrum access of TV Bands," in *Proc. 2nd International Conference on Cognitive Radio Oriented Wireless Networks and Communications CrownCom 2007*, 1–3 Aug. 2007, pp. 225–233.

[64] S. H. Hwang, J. S. Um, M. S. Song, C. J. Kim, H. R. Park, and Y. H. Kim, "Design and verification of IEEE 802.22 WRAN physical layer," in *Proc. 3rd International Conference on Cognitive Radio Oriented Wireless Networks and Communications CrownCom 2008*, 15–17 May 2008, pp. 1–6.

[65] FCC, "Revision of oarts 2 and 15 of the commissions rules to permit unlicensed national information infrastructure (U-NII) devices in the 5GHz band," ET Docket, no. 03-122, Nov. 18, 2003.

[66] E. Au, G. Chouinard, and Z. Lei, "IEEE P802.22 wireless RANs receiver performance evaluation criteria," IEEE 802.22-08/0326r2, http://www.ieee802.org/22/, Dec. 2008.

[67] S. Datta, *Surface Acoustic Wave Devices*. Prentice Hall, 1986.

[68] C. Campbell, *Surface Acoustic Wave Devices and Their Signal Processing Applications*. Academic Press, 1989.

[69] H. Meier, T. Baier, and G. Riha, "Miniaturization and advanced functionalities of SAW devices," *IEEE Trans. Microw. Theory Tech.*, vol. 49, no. 4, pp. 743–748, April 2001.

[70] S. Yoshimoto, Y. Yamamoto, Y. Takahashi, and E. Otsuka, "Multi-band RF SAW filter for mobile phone using surface mount plastic package," in *Proc. IEEE Ultrasonics Symposium*, vol. 1, 8–11 Oct. 2002, pp. 113–118.

[71] N. Shigekawa, K. Nishimura, T. Suemitsu, H. Yokoyama, and K. Hohkawa, "SAW filters composed of interdigital schottky and ohmic contacts on AlGaN/GaN heterostructures," *IEEE Electron Device Lett.*, vol. 28, no. 2, pp. 90–92, Feb. 2007.

[72] F. Shiba, M. Yamazaki, O. Iijima, and H. Yatsuda, "GPS SAW filter using a wafer level technique," in *Proc. IEEE Ultrasonics Symposium*, 28–31 Oct. 2007, pp. 937–940.

[73] G. M. Rebeiz, *RF MEMS: theory, design, and technology*. John Wiley and Sons, 2003.

[74] L. Dussopt and G. M. Rebeiz, "Intermodulation distortion and power handling in RF MEMS switches, varactors, and tunable filters," *IEEE Trans. Microw. Theory Tech.*, vol. 51, no. 4, pp. 1247–1256, April 2003.

[75] K. W. Nadim Maluf, *Introduction to Microelectromechanical Systems Engineering*, 2nd ed. Artech House, 2004.

[76] A. Takacs, D. Neculoiu, D. Vasilache, A. Muller, P. Pons, L. Bary, and R. Plana, "Design of tunable MEMS filters for millimeter wave systems," in *Proc. IEEE Mediterranean Electrotechnical Conference MELECON 2006*, 16–19 May 2006, pp. 301–304.

[77] D. fang Wei, Y. liang Li, and J. de Zhao, "Design of MEMS filter for WiMAX systems," in *Proc. 8th International Conference on Electronic Packaging Technology ICEPT 2007*, 14–17 Aug. 2007, pp. 1–3.

[78] I. Reines, A. Brown, M. El-Tanani, A. Grichener, and G. Rebeiz, "1.6–2.4 GHz RF MEMS tunable 3-pole suspended combline filter," in *Proc. IEEE MTT-S International Microwave Symposium Digest*, 15–20 June 2008, pp. 133–136.

[79] F. Islam, M. A. M. Ali, B. Y. Majlis, and N. Amin, "RF MEMS tunable filter: design, simulation and fabrication process," in *Proc. International Conference on Electrical and Computer Engineering ICECE 2008*, 20–22 Dec. 2008, pp. 247–250.

[80] X. Zou, K. Chen, H. Zhang, and J. Zhang, "Design and simulation of 4-bit 10-14GHz RF MEMS tunable filter," in *Proc. 4th IEEE International Conference on Nano/Micro Engineered and Molecular Systems NEMS 2009*, 5–8 Jan. 2009, pp. 21–24.

[81] W. Kaufman and S. Garrett, "Tapered distributed filters," *IRE Transactions on Circuit Theory*, vol. 9, no. 4, pp. 329–336, Dec 1962.

[82] M. C. Horton and R. J. Wenzel, "General theory and design of optimum quarter-wave TEM filters," *IEEE Trans. Microw. Theory Tech.*, vol. 13, no. 3, pp. 316–327, May 1965.

[83] I. Hunter, *Theory and Design of Microwave Filters*. The Institution of Electrical Engineering, London, United Kingdom, 2001.

[84] T. Prodromakis and C. Papavassiliou, "Distributed filter design on silicon cmos," in *Proc. IEEE International Symposium on Circuits and Systems ISCAS 2006*, 2006, pp. 4pp.–3312.

[85] J. Brinkhoff and F. Lin, "Integrated filters for 60 GHz systems on CMOS," in *Proc. IEEE International Workshop on Radio-Frequency Integration Technology RFIT 007*, 9–11 Dec. 2007, pp. 154–157.

[86] P. Jarry and J. Beneat, *Advanced Design Techniques and Realizations of Microwave and RF Filters*. John Wiley & Sons Inc., 2008.

[87] R. Schaumann and M. Van Valkenburg, *Design of Analog filters*. Oxford University Press, 2001.

[88] Y. Sun, *Design of High Frequency Integrated Analogue Filters*. The Institution of Electrical Engineers, 2002.

[89] W. V. Kuang and J. S. Wight, "A novel biquad filter circuit for continuous-time sigma-delta modulators," in *Proc. VTC-2006 Fall Vehicular Technology Conference 2006 IEEE 64th*, 25–28 Sept. 2006, pp. 1–4.

[90] A. Yamazaki, A. Ravindran, O. C. Akgun, and M. Ismail, "An active-RC reconfigurable lowpass-polyphase Tow-Thomas biquad filter," in *Proc. 47th Midwest Symposium on Circuits and Systems MWSCAS '04*, vol. 1, 25–28 July 2004, pp. I–57–60.

[91] V. Dhanasekaran, M. Gambhir, J. Silva-Martinez, and E. Sanchez-Sinencio, "A 1.1 GHz fifth order active-LC butterworth type equalizing filter," *IEEE J. Solid-State Circuits*, vol. 42, no. 11, pp. 2411–2420, Nov. 2007.

[92] M. O. Shaker, S. A. Mahmoud, and A. M. Soliman, "High-order Gm-C filters with current transfer function based on multiple loop feedback," in *Proc. IEEE International Conference on Signal Processing and Communications ICSPC 2007*, 24–27 Nov. 2007, pp. 85–88.

[93] J.-H. Weng and C.-Y. Yang, "An active Gm-C filter using a linear transconductance," in *Proc. IEEE Conference on Electron Devices and Solid-State Circuits EDSSC 2007*, 20–22 Dec. 2007, pp. 909–912.

[94] D. Jurisic, N. Mijat, and G. S. Moschytz, "Tuning elliptic filters with a 'tuning biquad'," in *Proc. IEEE International Symposium on Circuits and Systems ISCAS 2009*, 24–27 May 2009, pp. 45–48.

[95] R. W. Brodersen, P. R. Gray, and D. A. Hodges, "MOS switched-capacitor filters," *Proc. IEEE*, vol. 67, no. 1, pp. 61–75, Jan. 1979.

[96] T. Viswanathan, S. Faruque, K. Singhal, and J. Vlach, "Switched-capacitor transconductance and related building blocks," *IEEE Trans. Circuits Syst.*, vol. 27, no. 6, pp. 502–508, Jun 1980.

[97] D. A. Johns and K. Martin, *Analog integrated circuit design*. John Wiley & Sons Inc., 1997.

[98] [Online] available: http://www.tvlicensing.biz/detection/index.htm.

[99] B. Wild and K. Ramchandran, "Detecting primary receivers for cognitive radio applications," in *Proc. First IEEE International Symposium on New Frontiers in Dynamic Spectrum Access Networks DySPAN 2005*, 8–11 Nov. 2005, pp. 124–130.

[100] R. Wolff, "An assessment of the potential terrestrial interference due to direct broadcast satellite television receivers," *IEEE J. Sel. Areas Commun.*, vol. 3, no. 1, pp. 148–154, Jan. 1985.

[101] N. C. Hamilton, "Aspects of direct conversion receiver design," in *Proc. Fifth International Conference on HF Radio Systems and Techniques*, 22-25 Jul. 1991, pp. 299–303.

[102] S. A. Hamzah, M. F. Baharudin, N. M. Shah, Z. Z. Abidin, and A. Ubin, "Indoor channel prediction and measurement for wireless local area network (WLAN) system," in *Proc. International Conference on Communication Technology ICCT '06*, 27–30 Nov. 2006, pp. 1–5.

[103] D.-R. Huang, S.-W. Kao, and Y.-H. Pang, "A WiMAX receiver with variable bandwidth of 2.5 - 20 MHz and 93 dB dynamic gain range in 0.13-μm CMOS process," in *Proc. IEEE Radio Frequency Integrated Circuits (RFIC) Symposium*, 3–5 June 2007, pp. 369–372.

[104] A. Taparia, S. A. Nakvi, and B. Banerjee, "A low-IF WiMAX RF transceiver in 0.18μm CMOS technology," in *Proc. IEEE Dallas Circuits and Systems Workshop: System-on-Chip - Design, Applications, Integration, and Software*, 19–20 Oct. 2008, pp. 1–4.

[105] J. G. Atallah, S. Rodriguez, L.-R. Zheng, and M. Ismail, "A direct conversion WiMAX RF receiver front-end in CMOS technology," in *Proc. International Symposium on Signals, Circuits and Systems ISSCS 2007*, vol. 1, 13–14 July 2007, pp. 1–4.

[106] Adiseno, G. Wiranto, and T. M. S. Soegandi, "A low-cost CMOS reconfigurable receiver for WiMAX applications," in *Proc. IEEE International Conference on Semiconductor Electronics ICSE '06*, Oct. 29 2006–Dec. 1 2006, pp. 346–351.

[107] M. Locher, J. Kuenen, A. Daanen, H. Visser, B. H. Essink, P. P. Vervoort, R. Kopmeiners, W. Alkema, W. Redman-White, R. Balmford, and R. El Waffaoui, "A versatile, low power, high performance BiCMOS MIMO/diversity direct conversion transceiver IC for WiBro/WiMAX (802.16e)," *IEEE J. Solid-State Circuits*, vol. 43, no. 8, pp. 1731–1740, Aug. 2008.

[108] B. J. Farahani and M. Ismail, "WiMAX/WLAN radio receiver architecture for convergence in WMANS," in *Proc. 48th Midwest Symposium on Circuits and Systems*, 7–10 Aug. 2005, pp. 1621–1624.

[109] Y. Yu, L. Bu, S. Shen, B. Jalali-Farahani, G. Ghiaasi, P. Zhang, and M. Ismail, "A 1.8 V fully integrated dual-band VCO for zero-IF WiMAX/WLAN receiver in 0.18μm CMOS," in *Proc. 48th Midwest Symposium on Circuits and Systems*, 7–10 Aug. 2005, pp. 1259–1262.

[110] Y. Zhou, C. P. Yoong, L. S. Weng, Y. J. Khoi, M. Chia Yan Wah, K. Ang Chai Moy, and D. Wee Tue Fatt, "A 5 GHz dual-mode WiMAX/WLAN direct-conversion receiver," in *Proc. IEEE International Symposium on Circuits and Systems ISCAS 2006*, 2006, p. 4pp.

[111] F. Montaudon, R. Mina, S. Le Tual, L. Joet, D. Saias, R. Hossain, F. Sibille, C. Corre, V. Carrat, E. Chataigner, J. Lajoinie, S. Dedieu, F. Paillardet, and E. Perea, "A scalable 2.4-to-2.7GHz Wi-Fi/WiMAX discrete-time receiver in 65nm CMOS," in *Proc. Digest of Technical Papers. IEEE International Solid-State Circuits Conference ISSCC 2008*, 3–7 Feb. 2008, pp. 362–619.

[112] C. E. Shannon, "Communication in the presence of noise," *Proceedings of the IRE*, vol. 37, no. 1, pp. 10–21, Jan. 1949.

[113] A. Papoulis and S. Pillai, *Probability, Random Variables, and Stochastic Processes*, 4th ed. McGraw-Hill New York, 2002.

[114] M. R. Spiegel and J. Liu, *Mathematical Handbook of Formulas and Tables Schaum's Outline Series*, 2nd ed. McGraw-Hill, 1998.

[115] J. Lin, "A low-phase-noise 0.004-ppm/step DCXO with guaranteed monotonicity in the 90-nm CMOS process," *IEEE J. Solid-State Circuits*, vol. 40, no. 12, pp. 2726–2734, Dec. 2005.

[116] S. Farahvash, C. Quek, and M. Mak, "A temperature-compensated digitally-controlled crystal pierce oscillator for wireless applications," in *Proc. Digest of Technical Papers. IEEE International Solid-State Circuits Conference ISSCC 2008*, 3–7 Feb. 2008, pp. 352–619.

[117] M. I. Skolnik, *Introduction to Radar Systems*, 3rd ed. McGraw-Hill, 2001.

[118] A. V. Oppenheim and R. W. Schafer, *Discrete-Time Signal Processing*, 2nd ed. Prentice-Hall, Inc. Upper Saddle River, NJ, USA, 1999.

[119] B. Razavi, *RF Microelectronics*. Prentice Hall, 1998.

[120] T. H. Lee, *The Design of CMOS Radio-Frequency Integrated Circuits*, 2nd ed. Cambridge University Press, 2004.

[121] B. Razavi, "A study of phase noise in CMOS oscillators," *IEEE J. Solid-State Circuits*, vol. 31, no. 3, pp. 331–343, Mar. 1996.

[122] G. F. Earl, "Consideration of reciprocal mixing in HF OTH radar design," in *Proc. Seventh International Conference on (Conf HF Radio Systems and Techniques Publ. No. 441)*, 7–10 July 1997, pp. 256–259.

[123] J.-H. Bae, J.-C. Kim, B.-W. Jeon, J.-W. Jung, J.-S. Park, B.-J. Jang, H.-R. Oh, Y.-J. Moon, and Y.-R. Seong, "Analysis of phase noise requirements on local oscillator for RFID system considering range correlation," in *Proc. European Microwave Conference*, 9–12 Oct. 2007, pp. 1664–1667.

[124] F. Gardner, "Charge-pump phase-locked loops," *IEEE Trans. Commun.*, vol. COM-28, no. 11, pp. 1849–1858, Nov. 1980.

[125] B. Razavi, *Design of Analog CMOS Integrated Circuits*. McGraw-Hill Boston, MA, 2001.

[126] K. Hosaka, S. Harase, S. Izumiya, and T. Adachi, "A cascode crystal oscillator suitable for integrated circuits," in *Frequency Control Symposium and PDA Exhibition, 2002. IEEE International*, May 2002, pp. 610–614.

[127] T. A. D. Riely, M. A. Copeland, and T. Kwasniewski, "Delta-sigma modulation in fractional-N frequency synthesis," *IEEE J. Solid-State Circuits*, vol. 28, no. 5, pp. 553–559, May 1993.

[128] S. E. Meninger and M. H. Perrott, "A fractional-N frequency synthesizer architecture utilizing a mismatch compensated PFD/DAC structure for reduced quantization-induced phase noise," *Circuits and Systems II: Analog and Digital Signal Processing, IEEE Transactions on [see also Circuits and Systems II: Express Briefs, IEEE Transactions on]*, vol. 50, no. 11, pp. 839–849, Nov. 2003.

[129] E. Temporiti, G. Albasini, I. Bietti, R. Castello, and M. Colombo, "A 700-kHz bandwidth $\Sigma\Delta$ fractional synthesizer with spurs compensation and linearization techniques for WCDMA applications," *IEEE J. Solid-State Circuits*, vol. 39, no. 9, pp. 1446–1454, Sept. 2004.

[130] A. Swaminathan, K. J. Wang, and I. Galton, "A wide-bandwidth 2.4 GHz ISM band fractional-N PLL with adaptive phase noise cancellation," *IEEE J. Solid-State Circuits*, vol. 42, no. 12, pp. 2639–2650, Dec. 2007.

[131] A. Demir, A. Mehrotra, and J. Roychowdhury, "Phase noise in oscillators: a unifying theory and numerical methods for characterization," *IEEE Trans. Circuits Syst. I*, vol. 47, no. 5, pp. 655–674, May 2000.

[132] A. Demir, "Phase noise and timing jitter in oscillators with colored-noise sources," *IEEE Trans. Circuits Syst. I*, vol. 49, no. 12, pp. 1782–1791, Dec. 2002.

[133] ——, "Computing timing jitter from phase noise spectra for oscillators and phase-locked loops with white and $1/f$ noise," *IEEE Trans. Circuits Syst. I*, vol. 53, no. 9, pp. 1869–1884, Sept. 2006.

[134] M. Lax, "Classical noise. V. noise in self-sustained oscillators," *Physical Review*, vol. CAS-160, no. 2, pp. 290–307, Aug. 1967.

[135] R. L. Stratonovich, *Topics in the Theory of Random Noise*. New York: Gordon & Breach Science Pub, 1967, vol. II.

[136] D. Ham and A. Hajimiri, "Virtual damping and Einstein relation in oscillators," *IEEE J. Solid-State Circuits*, vol. 38, no. 3, pp. 407–418, Mar. 2003.

[137] A. Mehrotra, "Noise analysis of phase-locked loops," in *Proc. ICCAD-2000 Computer Aided Design IEEE/ACM International Conference on*, 5–9 Nov. 2000, pp. 277–282.

[138] S. Wei, D. L. Goeckel, and P. E. Kelly, "A modern extreme value theory approach to calculating the distribution of the peak-to-average power ratio in OFDM systems," in *Proc. IEEE International Conference on Communications ICC 2002*, vol. 3, 28 April–2 May 2002, pp. 1686–1690.

[139] A. G. Mason, G. Drury, and N. Lodge, "Digital television to the home - when will it come?" in *Broadcasting Convention, 1990. IBC 1990., International*, 1990, pp. 51–57.

[140] S. Park, L. E. Larson, and L. B. Milstein, "Hidden mobile terminal device discovery in a UWB environment," in *Proc. IEEE 2006 International Conference on Ultra-Wideband*, Sept. 2006, pp. 417–421.

[141] ——, "Mobile Terminal Detection for UWB/WiMAX Coexistence," submitted to *IEEE Transactions on Vehicular Technology*.

[142] L. S. Cutler and C. L. Searle, "Some aspects of the theory and measurement of frequency fluctuations in frequency standards," *Proc. IEEE*, vol. 54, no. 2, pp. 136–154, Feb. 1966.

[143] D. B. Leeson, "A simple model of feedback oscillator noise spectrum," *Proc. IEEE*, vol. 54, no. 2, pp. 329–330, Feb. 1966.

[144] W. D. Yan and R. R. Mansour, "Tunable dielectric resonator bandpass filter with embedded MEMS tuning elements," *IEEE Trans. Microw. Theory Tech.*, vol. 55, no. 1, pp. 154–160, Jan. 2007.

[145] A. Yoshizawa and Y. Tsividis, "A channel-select filter with agile blocker detection and adaptive power dissipation," *IEEE J. Solid-State Circuits*, vol. 42, no. 5, pp. 1090–1099, May 2007.

[146] Y. Palaskas and Y. Tsividis, "Power-area-DR-frequency-selectivity tradeoffs in weakly nonlinear active filters," in *Proc. International Symposium on Circuits and Systems ISCAS '03*, vol. 1, 25–28 May 2003, pp. I–453–I–456.

[147] L. E. Franks and I. W. Sandberg, "An alternative approach to the realization of network transfer functions: The N-path filter," *Bell System Tech. J*, vol. 39, pp. 1321–1350, Sept. 1960.

[148] H. Wupper, "A modified N-path filter suited for practical realization," *IEEE Trans. Circuits Syst.*, vol. 21, no. 3, pp. 449–456, May 1974.

[149] S. Park, L. E. Larson, and L. B. Milstein, "Phase noise effects on signal detection for UWB/WiMAX coexistence," in *Proc. IEEE Military Communications Conference MILCOM 2008*, 16–19 Nov. 2008, pp. 1–7.

[150] ——, "An RF receiver detection technique for UWB/WiMAX coexistence with applications to cognitive Radio," submitted to *IEEE Transactions on Circuits and Systems II*.

[151] S. G. Rayment, P. Eccelsine, G. Chouniard, M. Christensen, M. Austin, and M. Sandmann, "Regulatory tutorial material," sg-whitespace-09/0048r3, https://mentor.ieee.org/802-sg-whitespace/documents/, Mar. 10 2009.

[152] C. Einof, "IEEE P802.22 wireless RANs proposed resolution to comment 283," IEEE 802.22-09/0022r1, http://www.ieee802.org/22/, Jan. 2009.

[153] H. Khatri, "Interference mitigation techniques for SAW-less CDMA receivers," Ph.D. dissertation, University of California - San Diego (UCSD), La Jolla, USA, 2009.

[154] B. W. Cook, A. Berny, A. Molnar, S. Lanzisera, and K. S. J. Pister, "Low-power 2.4-GHz transceiver with passive RX front-end and 400-mV supply," *IEEE J. Solid-State Circuits*, vol. 41, no. 12, pp. 2757–2766, Dec. 2006.

[155] S. Maas, "Theory and analysis of GaAs MESFET mixers," *IEEE Transactions on Microwave Theory and Techniques*, vol. 32, pp. 1403–1406, 1984.

[156] H. Khatri, L. Liu, T. Chang, P. S. Gudem, and L. E. Larson, "A SAW-less CDMA receiver front-end with single-ended LNA and single-balanced mixer with 25% duty-cycle LO in 65nm CMOS," in *Proc. IEEE Radio Frequency Integrated Circuits Symposium RFIC 2009*, 7–9 June 2009, pp. 13–16.